



**Cinvestav**

**CENTRO DE INVESTIGACIÓN Y DE ESTUDIOS AVANZADOS DEL  
INSTITUTO POLITÉCNICO NACIONAL**

UNIDAD SALTILLO

“Development of Heteroatoms-doped Ordered Mesoporous Carbon Hollow Spheres:  
Evaluation as electrocatalysts for the Oxygen Reduction Reaction”

A dissertation submitted in partial fulfillment of the requirements for the degree of:

Doctor en Ciencias

In:

Sustentabilidad de los Recursos Naturales y Energía

By:

M. C. Juan Carlos Carrillo Rodríguez

Thesis advisors:

Dra. Ivonne Liliana Alonso Lemus  
Dr. Francisco Javier Rodríguez Varela



**Cinvestav**

**CENTRO DE INVESTIGACIÓN Y DE ESTUDIOS AVANZADOS DEL  
INSTITUTO POLITÉCNICO NACIONAL**

UNIDAD SALTILLO

“Desarrollo de Esferas Huecas de Carbón Mesoporoso Ordenado dopadas con heteroátomos:  
Evaluación como electrocatalizadores para la Reacción de Reducción de Oxígeno”

Tesis que presenta:

M. C. Juan Carlos Carrillo Rodríguez

Para obtener el grado de

Doctor en Ciencias en Sustentabilidad de los Recursos Naturales y Energía

Directores de tesis:

Dra. Ivonne Liliana Alonso Lemus  
Dr. Francisco Javier Rodríguez Varela

# Content

Abstract .....	iv
Resumen .....	v
Introduction .....	1
<b>CHAPTER I.</b> .....	6
Background .....	6
1.1. Fuel Cells .....	6
1.1.1. Anion Exchange Membrane Fuel Cells (AEMFCs) .....	7
1.2. Electrocatalytic activity of metal-free electrocatalysts for the ORR .....	9
1.2.1. Heteroatoms-doped OMCHS for the ORR .....	14
1.3. Design and fabrication approaches for the synthesis of OMCHS .....	15
1.4. Theoretical study of R-F polymers .....	18
1.4.1. Theoretical models of the R-F reactions .....	19
<b>CHAPTER II.</b> .....	29
Hypothesis .....	29
Objectives .....	29
<b>CHAPTER III.</b> .....	30
Materials and methods .....	30
3.1 Reagents and gases .....	30
3.2 Synthesis of N-doped, S-doped, and N/S co-doped OMCHS .....	30
3.4. Theoretical study of the resorcinol-formaldehyde (R-F) reaction .....	35
3.4.1. Synthesis of R-F polymers .....	35
3.4.2. Theoretical calculation .....	35
<b>CHAPTER IV.</b> .....	37
Insight into the performance and stability of N-doped Ordered Mesoporous Carbon Hollow Spheres for the ORR: Influence of the nitrogen species on their catalytic activity after ADT .....	37
4.1. Physicochemical characterization of N-doped OMCHS .....	37
4.2. The catalytic activity of the N-doped OMCHS for the ORR .....	42
4.3. Surface chemical composition of the N-doped OMCHS before ADT .....	46
4.4. Catalytic activity for the ORR and surface chemical composition of the N-doped OMCHS after ADT .....	49
4.5. Conclusions .....	56

<b>CHAPTER V.....</b>	<b>60</b>
Influence of the sulfur and nitrogen species on catalytic activity to the ORR of N-S-co-doped OMCHS after ADT: a study of the performance and stability.....	60
5.1. Physicochemical characterization of N-S-doped OMCHS .....	60
5.2. Catalytic activity of the N/S co-doped OMCHS for the ORR.....	64
5.3. Surface chemical composition of S-doped and N/S-doped OMCHS before ADT.....	67
5.4. Catalytic activity for the ORR and surface chemical composition of S doped and N/S co-doped OMCHS after ADT.....	72
5.5. Conclusions.....	79
<b>CHAPTER VI.....</b>	<b>83</b>
Three-dimensional modeling the Resorcinol-Formaldehyde (R-F) polymer: a DFT and XRD study.....	83
6.1. Determination of lattice parameters, enthalpy of formation ( $\Delta H_f$ ) and bulk modulus.....	83
6.2. Comparative analysis of experimental and theoretical XRD patterns of R-F polymers..	91
6.3. Conclusions.....	95

## Abstract

In this work, it is shown that novel heteroatoms-doped (nitrogen -N- and sulfur -S-) Ordered Mesoporous Carbon Spheres (OMCHS) promote the Oxygen Reduction Reaction (ORR) in alkaline media.

In the first section of this work, N-doped OMCHS are synthesized using two different sources: i) 2-pyridinecarboxaldehyde; (N1-OMCHS), and ii) pyrrole (N2-OMCHS). The electrochemical characterization for the ORR shows the highest catalytic activity of N2-OMCHS in terms of onset potential ( $E_{\text{onset}} = 0.88$  V), half-wave potential ( $E_{1/2} = 0.82$  V), percentage of hydroperoxyl ion produced ( $\% \text{HO}_2^- = 3.8\%$ ), and electron transfer number ( $n = 3.92$ ). Evaluation of their stability by accelerated degradation test (ADT) indicates that the performance of N1-OMCHS shows a better stability compared to N2-OMCHS. The high stability towards the ORR is ascribed to the chemical modification of N species on the surface of the N-doped OMCHS.

The second section involves doping OMCHS with S and co-doping with S and N using: i) 2-thiophenemethanol (S-OMCHS); ii) 2-pyridinecarboxaldehyde/2-thiophenemethanol (N1-S-OMCHS); and iii) pyrrole/2thiophenemethanol (N2-S-OMCHS). S-OMCHS shows a higher performance for the ORR ( $E_{\text{onset}} = 0.88$  V,  $E_{1/2} = 0.81$  V,  $\text{HO}_2^-$  yield= 2.8%, and  $n= 3.95$ ) than N1-S-OMCHS and N2-S-OMCHS. Moreover, it is observed that the performance of S-OMCHS and N1-S-OMCHS improved after ADT. However, the three electrocatalysts show a high stability. Analysis of the chemical surface composition of the S-OMCHS, N1-S-OMCHS and N2-S-OMCHS demonstrates that interaction between nitrogen and sulfur species improve their catalytic activity towards the ORR.

In the third stage, a novel model of resorcinol-formaldehyde (R-F) polymer is designed from the saturation of  $\alpha$  and  $\beta$  resorcinol phases with formaldehyde molecules. The X-ray diffraction (XRD) patterns of the experimental RF polymers show a change from crystalline to amorphous structures, which is in good agreement with the theoretically obtained patterns. The similarities between the experimental and theoretical patterns provide the certainty that the proposed models are correctly proposed, allowing for the theoretical evaluation of the ORR at OMCHS in the future.

## Resumen

En el presente trabajo se muestran novedosas Esferas Huecas de Carbono Mesoporoso Ordenado (OMCHS, por sus siglas en inglés) dopadas con heteroátomos (nitrógeno -N- y azufre -S-) promueven la Reacción de Reducción de Oxígeno (RRO) en medio alcalino.

En la primera etapa de este trabajo, OMCHS dopadas con N se sintetizan usando dos fuentes de nitrógeno: i) 2-piridincarboxaldehído (N1-OMCHS), y ii) pirrol (N2-OMCHS). La caracterización electroquímica para la RRO muestra que N2-OMCHS tiene una actividad catalítica más alta en términos de potencial de inicio ( $E_{\text{onset}} = 0.88 \text{ V}$ ), potencial de media onda ( $E_{1/2} = 0.82 \text{ V}$ ), porcentaje de ion hidróperóxido producido ( $\% \text{HO}_2^- = 3.8\%$ ), y número de electrones transferidos ( $n = 3.92$ ). La evaluación de su estabilidad mediante una prueba de degradación acelerada (ADT) indica que el desempeño de N1-OMCHS y N2-OMCHS mejora, comparando con su comportamiento antes de la prueba. En este sentido, N1-OMCHS tiene una mejor estabilidad en relación con N2-OMCHS. La alta estabilidad hacia la RRO se atribuye a la modificación química de especies de N en la superficie de las OMCHS dopadas con nitrógeno.

La segunda etapa consiste en dopar OMCHS con S y co-dopar con S y N usando: i) 2-tiofenometanol (S-OMCHS); ii) 2-piridincarboxaldehído/2-tiofenometanol (N1-S-OMCHS) y iii) pirrol/2-tiofenometanol (N2-S-OMCHS). S-OMCHS muestra el mejor desempeño para la RRO ( $E_{\text{onset}} = 0.88 \text{ V}$ ,  $E_{1/2} = 0.81 \text{ V}$ ,  $\% \text{HO}_2^- = 2.8\%$ , y  $n = 3.95$ ) en comparación con N1-S-OMCHS y N2-S-OMCHS. Además, se observa que el desempeño de S-OMCHS y N1-S-OMCHS mejora después de ADT. Sin embargo, los tres electrocatalizadores tienen una estabilidad. El análisis de la composición química de superficie de S-OMCHS, N1-S-OMCHS y N2-S-OMCHS muestran que interacciones entre los átomos de nitrógeno y azufre mejoran su actividad catalítica para la RRO.

En la tercera etapa, se diseña un modelo novedoso del polímero resorcinol-formaldehído (R-F) a partir de la saturación de las fases  $\alpha$  y  $\beta$  del resorcinol con moléculas de formaldehído. Los patrones de difracción de rayos X (XRD, por sus siglas en inglés) experimentales de los polímeros de RF muestran un cambio de estructura cristalina a amorfa, que concuerda con los patrones obtenidos teóricamente. Las similitudes entre los patrones experimentales y teóricos brindan la certeza de que los modelos son correctamente propuestos, lo que permitiría evaluar teóricamente en un futuro la RRO en OMCHS.

## Introduction

---

The increasing demand for clean energy has generated worldwide research efforts to develop high-performing, inexpensive, and environmentally friendly electrochemical devices for energy generation [1].

Anion Exchange Membrane Fuel Cells (AEMFCs) are a technology that satisfies such goals. These systems can generate electricity from several fuels such as H<sub>2</sub> or alcohols with higher efficiency than traditional energy systems. Unfortunately, AEMFCs have two important drawbacks: i) the chemical composition of the anode and cathode electrodes, which in most cases requires the use of expensive and low earth-abundant noble metal electrocatalysts (e.g., Pt), which limits the fuel cell large-scale production, and ii) the slow kinetics of the Oxygen Reduction Reaction (ORR), which takes place at the cathode, limiting the performance of the fuel cell [2–4].

Usually, the cathode electrocatalysts are made of Pt supported on Vulcan (Pt/C), which is the most active material for the ORR. However, as mentioned above, efforts are being made to replace or limit the use of Pt/C, aiming to reduce the production costs of AEMFCs [5]. Therefore, the search for electrocatalysts with similar catalytic activity than Pt/C, without its limitations, is one of the most challenging topics in fuel cell research.

One of the most promising alternatives to replace Pt/C is the development of Metal-free cathode electrocatalysts. They are typically carbon-based materials (e.g., graphene, carbon nanotubes, carbon nanoparticles, carbon spheres, and nanoporous carbons, etc.) doped with heteroatoms (e.g., B, S, N, P, etc.), which sometimes approaches the catalytic activity of Pt/C for the ORR [6–8].

Some of the advantages of metal-free electrocatalysts are: i) tailorable surface chemistry, ii) lower cost than Pt/C, iii) suitable structural characteristics, iv) high electronic conductivity, and v) high surface area [9–11]. Moreover, their catalytic activity for the ORR can be improved by substitutionally doping them with heteroatoms. Nevertheless, their performance still need to be improved on order to replace Pt/C and propose the production of Pt-free AEMFCs on a large scale basis [11].

Metal-free electrocatalysts are currently the subject of debate because the reaction mechanism of the ORR at their surface has not yet been fully clarified. In the case of N-doped carbon metal-free electrocatalysts, it has been suggested that nitrogen atoms induce oxygen chemisorption in adjacent carbon atoms which facilitates the cleavage of O-O bonds in O<sub>2</sub> molecules [12]. Analogous to nitrogen, sulfur atoms induce strain and stress to the sp<sup>2</sup> carbon lattice, modifying the charge distribution of the neighboring carbon atoms, which facilitates oxygen chemisorption promoting the ORR [4, 10].

There are few reports on the development of N, S-co-doped carbon metal-free electrocatalysts that show superior electrocatalytic activity compared to carbons doped with a single heteroatom. The enhanced catalytic activity of co-doped electrocatalysts has been ascribed to, a combined effect of both heteroatoms which facilitates the adsorption and bond cleavage of oxygen molecules [13].

In this context, high surface area Ordered Mesoporous Carbon Hollow Spheres (OMCHS) have gained considerable attention since these structures can be easily doped with heteroatoms. Their morphology is such that the shell is mesoporous in nature, with large internal cavities. These chemical, structural, and textural properties make them suitable as highly active electrocatalysts for the ORR [14, 15].

Meanwhile, OMCHS synthesized from resorcinol and formaldehyde have recently stood out because they are used in application such as energy storage, electromagnetic interference devices, antibacterial, and ablative process, among other, due to their electrical and textural properties, and they can adopt a three-dimensional architecture [16–21].

In this regard, chemical computational methods can be useful tools to propose models that help clarify the behavior of metal-free electrocatalysts [22, 23]. Therefore, it is necessary to generate models of resorcinol-formaldehyde based materials that allow to explain or predict their behavior, focusing particularly on their use as electrocatalysts for the ORR.

This thesis focuses on the development of heteroatoms-doped OMCHS, which are evaluated as cathode electrocatalysts for the ORR. In the first part, the catalytic activity N-doped OMCHS




for the ORR, along with their electrochemical stability after an accelerated degradation test (ADT), is evaluated in alkaline media. Changes in their surface chemistry after ADT have also been analyzed, aiming to propose a correlation with their electrochemical behavior.

In the second part, the catalytic activity for the ORR and electrochemical stability after ADT of S-doped and N-S co-doped OMCHS have been evaluated also in alkaline media. Like the previous electrocatalysts, modification of their surface chemical composition after ADT have been analyzed as well. The application of N and S as co-dopants is of particular interest, to evaluate if this approach is an effective strategy to enhance the catalytic activity of OMCHS for the ORR.

In last chapter, a novel theoretical model of resorcinol-formaldehyde reactions is developed. The goal is to propose a model having a behavior like resorcinol-formaldehyde materials synthesized in our Laboratory. The model can serve as the basis for the theoretical study of the surface of the heteroatoms-doped OMCHS, with a broader objective of performing subsequent DFT studies.

## References

- [1] Y. Deng, Y. Xie, K. Zou, X. Ji. Review on recent advances in nitrogen-doped carbons: preparations and applications in supercapacitors. *J. Mater. Chem. A* 4 (2016) 1144–1173.
- [2] R. Silva, D. Voiry, M. Chhowalla, T. Asefa. Efficient metal-free electrocatalysts for oxygen reduction: Polyaniline-derived N- and O-doped mesoporous carbons. *J. Am. Chem. Soc.* 135 (2013) 7823–7826.
- [3] M. Shao. Palladium-based electrocatalysts for hydrogen oxidation and oxygen reduction reactions. *J. Power Sources.* 196 (2011) 2433–2444.
- [4] X. Ge, Sumboja, D. Wu, T. An, B. Li, F.W.T. Goh, T.S.A. Hor, Y. Zong, Z. Liu. Oxygen Reduction in Alkaline Media: From Mechanisms to Recent Advances of Catalysts. *ACS Catal.* 5 (2015) 4643–4667
- [5] J.C. Carrillo-Rodríguez, I.L. Alonso-Lemus, A.A. Siller-Ceniceros, E. Martínez Guerra, P. Pizá-Ruiz, G. Vargas-Gutiérrez, F.J. Rodríguez-Varela. Easy synthesis of N-doped graphene by milling exfoliation with electrocatalytic activity towards the Oxygen Reduction Reaction (ORR). *Int. J. Hydrogen Energy* 42 (2017) 30383–30388.
- [6] A. Gupta, T. Sakthivel, S. Seal. Recent development in 2D materials beyond graphene. *Prog. Mater. Sci.* 3 (2015) 44–126.
- [7] D. Geng, N. Ding, T. Andy Hor, Z. Liu, X. Sun, Y. Zong, T. Hor, Z. Liu, X. Sun, Y. Zong. Potential of metal-free ‘graphene alloy’ as electrocatalysts for oxygen reduction reaction, *J. Mater. Chem. A.* 3 (2015) 1795–1810.
- [8] X. Zhou, L. Zheng, H. Nie, Z. Yang, G. Fang, Z. Yao, G. Li, X. Chen, S. Huang, G. Fang. Sulfur-doped graphene as an efficient metal-free cathode catalyst for oxygen reduction. *ACS Nano.* 6 (2012) 205–211.
- [9] H. P. Cong, P. Wang, M. Gong, S. H. Yu. Facile synthesis of mesoporous nitrogen-doped graphene: An efficient methanol-tolerant cathodic catalyst for oxygen reduction reaction. *Nano Energy.* 3 (2014) 55–63.
- [10] D.W. Wang, D. Su. Heterogeneous nanocarbon materials for oxygen reduction reaction. *Energy and Environ. Sci.* 7 (2014) 576–591.
- [11] L. Dai, Y. Xue, L. Qu, H.J. Choi, J.B. Baek. Metal-Free Catalysts for Oxygen Reduction Reaction. *Chem. Rev.* 115 (2015) 4823–4892.
- [12] J.C. Carrillo-Rodríguez, A.M. Garay-Tapia, B. Escobar-Morales, J. Escorcia-García, M.T. Ochoa-Lara, F.J. Rodríguez-Varela, I.L. Alonso-Lemus. Insight into the performance and stability of N-doped Ordered Mesoporous Carbon Hollow Spheres for the ORR: Influence of the nitrogen species on their catalytic activity after ADT. *Int. J. Hydrogen Energy* 46 (2021) 26087–26100.
- [13] L. Wang, W. Jia, X. Liu, J. Li, M.M. Titirici. Sulphur-doped ordered mesoporous carbon with enhanced electrocatalytic activity for the oxygen reduction reaction. *J. Energy Chem.* 25 (2016) 566–570.
- [14] T. Zhou, Y. Zhou, R. Ma, Z. Zhou, G. Liu, Q. Liu, Y. Zhu, J. Wang. Nitrogen-doped hollow mesoporous carbon spheres as a highly active and stable metal-free electrocatalyst for oxygen reduction. *Carbon* 114 (2017) 177–186.
- [15] C. Hsu, J. Jan, H. Lin, P. Kuo. Nitrogen-doped mesoporous carbon hollow spheres as a novel carbon support for oxygen reduction reaction. *New J. Chem.* 38 (2014) 5521–5526.
- [16] W. Kiciński, M. Norek, B.J. Jankiewicz. Heterogeneous carbon gels: N-doped carbon xerogels from resorcinol and n-containing heterocyclic aldehydes. *Langmuir* 30 (2014) 14276–14285.
- [17] K.Z. Gaca, J. Sefcik. Mechanism and kinetics of nanostructure evolution during early stages of resorcinol-formaldehyde polymerisation. *J. Colloid Interface Sci.* 406 (2013) 51–59.
- [18] A. Abolghasemi Mahani, S. Motahari, V. Nayyeri. Synthesis, characterization, and dielectric properties of one-step pyrolyzed / activated resorcinol-formaldehyde based carbon aerogels for electromagnetic interference shielding applications. *Mater. Chem. Phys.* 213 (2018) 492–501.
- [19] F. Li, L. Xie, G. Sun, Q. Kong, F. Su, Y. Cao, J. Wei, A. Ahmad, X. Guo, C.M. Chen. Resorcinol-formaldehyde based carbon aerogel: Preparation, structure, and applications in energy storage devices., *Microporous and Mesoporous Materials*, 279. Elsevier, 293–315, 01-May-2019
- [20] Yutika Badhe, Balasubramanian K, Rohit Gupta. Cost-effective, low density, carbon soot doped resorcinol formaldehyde composite for ablative applications. *RSC Adv.* 5 (2015) 23622–23634.
- [21] Yiman Zhong, Yonghong Ni, Shifeng Li, Meifang Wang. Chain-like Fe<sub>3</sub>O<sub>4</sub> resorcinol-formaldehyde resins–Ag composite microstructures: facile construction and applications in antibacterial and catalytic fields. *RSC Adv.* 6 (2016) 15831–15837.

- 
- [22] X. Bao, D. von Deak, E.J. Biddinger, U.S. Ozkan, C.M. Hadad. A computational exploration of the oxygen reduction reaction over a carbon catalyst containing a phosphinate functional group. *Chem. Commun.* 46 (2010) 8621–8623.
- [23] X. Chen, F. Li, X. Wang, S. Sun, D. Xia. Density Functional Theory Study of the Oxygen Reduction Reaction on a Cobalt–Polypyrrole Composite Catalyst. *J. Phys. Chem. C* 116 (2012) 12553–12558.

## CHAPTER I.

### Background

---

The increase in electricity demand has provoked changes in the cultural and social behaviour of the population in many countries because it is fundamental for modern, growing economies. Two-thirds of the energy produced by electricity generation systems (EGS) are used to meet transport, commercial and industrial activities, heating, and cooling demands, which represents 70% of total energy-related greenhouse gas (GHG) emission [1–3].

Consequently, GHG reduction has become a central topic in EGS, because it is where decarbonization can be achieved at an acceptable rate [4]. In addition, energy policies that promote the decarbonization, production, and storage of electricity from renewable and clean sources with low/zero GHG emissions are required [5]. Thus, worldwide research groups have focused their efforts on the development of more efficient and sustainable systems for the production and distribution of electric power [6]. One of the most promising technologies for sustainable energy production is that of fuel cells.

#### 1.1. Fuel Cells

Fuel cells are devices that directly convert fuel into electrical energy with low/zero GHG emissions through electrochemical reactions [7]. A general classification of fuel cells can be made based on their electrolyte: Solid Oxide Fuel Cell (SOFC), Phosphoric Acid Fuel Cell (PAFC), Molten Carbonate Fuel Cell (MCFC), Proton Exchange Membrane Fuel Cell (PEMFC), and Alkaline Fuel Cell (AFC)[8].

AFCs have several advantages over other technologies. For example, the Oxygen Reduction Reaction (ORR) kinetics is faster in alkaline media than in acid media, and noble metal electrocatalysts are not necessary to promote it at the cathode. However, earlier AFCs used an asbestos matrix impregnated with KOH as the electrolyte, forming solid deposits of potassium carbonates on the electrodes when CO<sub>2</sub>-containing gases are used as fuel, decreasing drastically the catalytic activity of the electrocatalysts [9]. Recently, alkaline polymer membranes have been developed which avoid the use of KOH and its disadvantages while maintaining the

benefits of AFCs, causing the rapid development of Anion Exchange Membrane Fuel Cell (AEMFC) [10].

### 1.1.1. Anion Exchange Membrane Fuel Cells (AEMFCs)

AEMFCs is constituted by three main components: i) anode, where the oxidation of H<sub>2</sub> (or other fuels) is carried out, ii) cathode, where the ORR takes place, and iii) anion exchange membrane (AEM, electrolyte), which plays a double role, transporting OH<sup>-</sup> from the cathode to the anode while acting as a separator of the electrodes avoiding the mixing of the reactants, as seen in Fig. 1.1 [11].

An additional element of AEMFCs is anode and cathode Gas Diffusion Layers (GDL) that provide support for the electrocatalysts layer and mechanical structure for the electrode. The GDL acts as a reactants/products transport channel, an electric current collector, and an electrons transporter to the current conductor [12, 13].

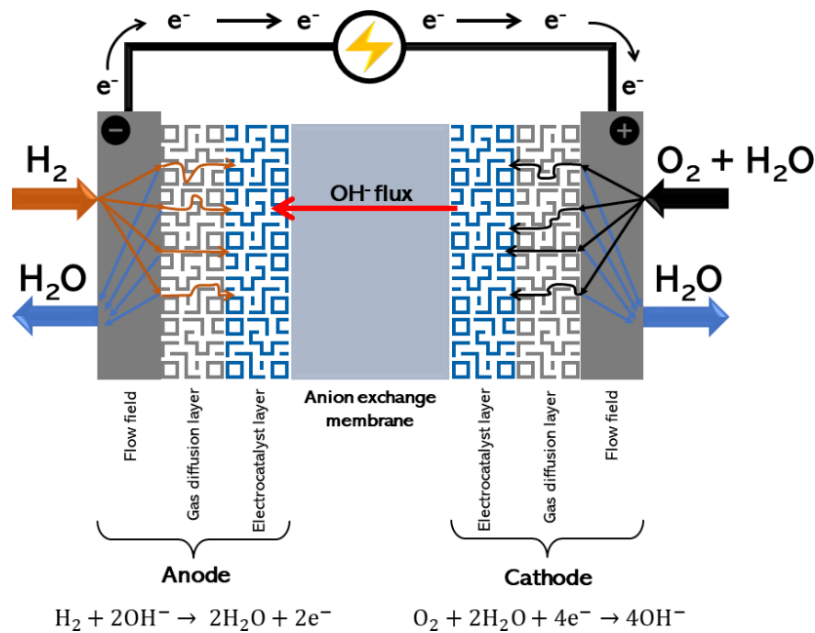
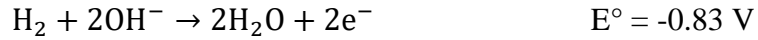
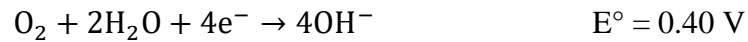


**Fig. 1.1.** Scheme representation of an AEMFC [14].

AEMFCs operation starts with OH<sup>-</sup> ions generated at the cathode, crossing the AEM to the anode electrocatalyst layer where the anode flow channel feeds with humidified H<sub>2</sub> to the anode GDL/electrocatalyst layer where the H<sub>2</sub> undergoes an oxidation reaction to produce H<sub>2</sub>O molecules and electrons. The anodic reaction is:



The electrons then go over through the anode GDL by an external circuit to the cathode GDL and electrocatalyst layer where humidified oxygen supplied by the cathode flow channel is transported through the cathode GDL where it is reduced in presence of water at the electrocatalysts layer to produce OH<sup>-</sup> ions. The cathodic reaction is:

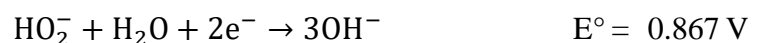
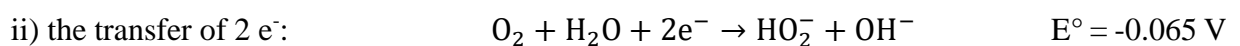
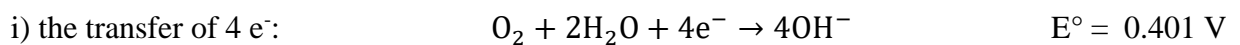


Then, the generated OH<sup>-</sup> ions are conducted through the AEM for the Hydrogen Oxidation Reaction (HOR), closing the operation cycle. Therefore, the overall reaction at AEMFCs is expressed as follow [15, 16]:



Hence, AEMFCs are attractive systems because, non-Pt electrocatalysts (e.g., inorganic oxides or metal-free electrocatalysts) can be used, at either the anode, the cathode, or both, weaker corrosion, and faster ORR kinetics [14, 17]. The ORR is critical for fuel cells because it dominates the overall performances [18, 19].

The ORR is kinetically sluggish than the HOR at the anode which requires an overpotential to overcome the kinetics barrier, so the energy efficiency is considerably reduced, thus limiting the commercialization of these electrochemical devices [19, 20]. For this reason, the development of electrocatalysts with high catalytic activity for the ORR is of high relevance. The ORR can occur in both acid and alkaline media via two mechanisms. In alkaline media, the electrochemical reactions are [21, 22]:



The 4e<sup>-</sup> pathway is preferable in fuel cell cathodes because the direct reduction of O<sub>2</sub> molecules to HO<sup>-</sup> occurs without the formation of chemical intermediates. Meanwhile, the 2e<sup>-</sup> pathway produces the hydroperoxyl ion (HO<sub>2</sub><sup>-</sup>) which is an undesired intermediate because it decreases the catalytic activity of cathode electrocatalysts and damages the membrane promoting the

crossover effect. Therefore, electrocatalysts can promote the ORR by one of these mechanisms or a combination of both, which depends on several of their properties and the pH of the electrolyte [23].

Pt/C is considered the best electrocatalyst for the ORR due to its high catalytic activity because it promotes the  $4 e^-$  pathway during the reaction. Its high performance is attributed to its high enough binding energy to adsorb oxygen molecules and weakly enough to desorb the reaction products (e.g.,  $\text{OH}^-$  species) [24].

However, Pt has a high cost because of its scarcity, low tolerance to CO and  $\text{CO}_2$  contained in low purity  $\text{H}_2$ , poor stability, and detrimental environmental effects. Moreover, it has shown a lower catalytic activity for the ORR in alkaline media compared to acid electrolytes [25–29]. There are different alternatives to reduce or replace Pt/C in fuel cell cathodes, such as the use of cheaper noble metals, Pt-transition metals alloys, Pt-metal oxides compounds, non-noble metal oxides, perovskites, spinel-like materials, and metal-free electrocatalysts [30–34].

## 1.2. Electrocatalytic activity of metal-free electrocatalysts for the ORR

Over the past years, metal-free electrocatalysts (carbon-based materials) have been developed, having the objective of being a feasible alternative to replace Pt/C. Pristine carbon-based materials are ORR inactive, meaning they are unable to adsorb  $\text{O}_2$  molecules or ORR intermediates. However, different strategies have been proposed to turn the metal-free electrocatalysts into ORR active: i) chemical doping (heteroatoms integration to  $\text{sp}^2$  matrix carbon), ii) physical intermolecular charge transfer (physical adsorption polyelectrolyte chain onto carbon), and iii) structural defects (formation of an armchair and zigzag edges or pentagon rings at matrix carbon)[35–38].

Metal-free electrocatalysts always have defects and/or structural disorders at the edge or over the surface. These defects in carbon nanomaterials can be divided into two groups: i) the intrinsic defects (carbon atoms rearrangement) and ii) the extrinsic defects (induced by heteroatoms and/or metal atoms dopants) [39–41].

The intrinsic defects in metal-free electrocatalysts include edge defects (armchair and zigzag), point defects (vacancies, holes, and voids), line defects (dislocation, grain boundaries), some

topological defects (pentagon, heptagon, Stone-Wales defects, and their combination), and surface defects. The effect of intrinsic defects in the carbon matrix for the ORR is that modify the electronic structure (charge and spin densities), which interrupt  $\pi$  conjugation facilitating the oxygen adsorption and dissociation over the surface or at the edge of the carbon matrix during the ORR [42–44].

On another hand, the catalytic activity for the ORR of carbon materials can be mainly enhanced by heteroatom doping because the size or electronegativity between heteroatom and the adjacent C atoms are usually different. The local charge and spin density of the carbon matrix has been altered, which can enable O<sub>2</sub> chemisorption, decreases the reaction energy barrier, and break the O–O bond thus, facilitate the ORR [42, 45, 46]. The defects on metal-free electrocatalysts (chemical doping or structural defects) can promote the mass transport of intermediate reactants on the triple-phase boundary regions to enhance the ORR kinetics [40, 47, 48].

When performing any of these strategies, this family of electrocatalysts exhibit high electrical conductivity (e.g., 3.3 S cm<sup>-2</sup> for N-doped carbon nanotubes [49]), good electrochemical potential cycling stability, and high surface area, (e.g., P/N co-doped hollow carbon sphere, 721 m<sup>2</sup> g<sup>-1</sup> [50], 3D porous N-doped carbon, 1074 m<sup>2</sup> g<sup>-1</sup> [51]). Furthermore, some N-doped metal-free electrocatalysts have shown high catalytic activity for the ORR (close to Pt/C) in alkaline solutions [21].

Nitrogen is the most widely used heteroatom for this purpose. It has been reported that some N-doped carbon electrocatalysts have similar catalytic activity for the ORR than Pt/C, which makes them materials with high potential for AEMFCs applications [52, 53]. They have unique electronic properties derived from the conjugation between the nitrogen lone-pair electrons and the  $\pi$  conjugation of the carbon structure [54].

Several reports indicate that the catalytic activity of doped carbon-based electrocatalysts towards the ORR is enhanced by the presence of N-pyridinic and N-quaternary species (Fig. 1.2), while N-pyrrolic species have no positive effect on the reaction [55, 56]. Some works show that N-pyridinic improves the onset potential, while N-quaternary increases the limiting current density of the ORR. However, each N specie's concentration and specific contribution in enhancing the catalytic activity for the ORR is not well-understood yet [57, 58].



Chen *et al.* synthesized N-doped carbon nanotubes with similar ORR performance compared to Pt/C in terms of onset potential ( $E_{\text{onset}} = 1.0$  V/RHE), half-wave potential ( $E_{1/2} = 0.87$  V/RHE), and electron transfer number ( $n = 3.63$ ) [59]. In the same manner, the study by Chen *et al.* shows that N-doped carbon nanocages exhibit good catalytic activity for the ORR ( $E_{\text{onset}} = 0.89$  V/RHE and  $n = 3.27$ ). The electrochemical stability of the nanocage is shown to be high, since the current density ( $j$ ) decreases by 10% in the diffusion-controlled region after testing for 100 h, compared to 40% of commercial Pt/C in alkaline media [60]. Despite having good electronic, structural, and textural properties, in some cases, the N-doped electrocatalyst performance is not yet comparable to that obtained by Pt/C for the ORR.

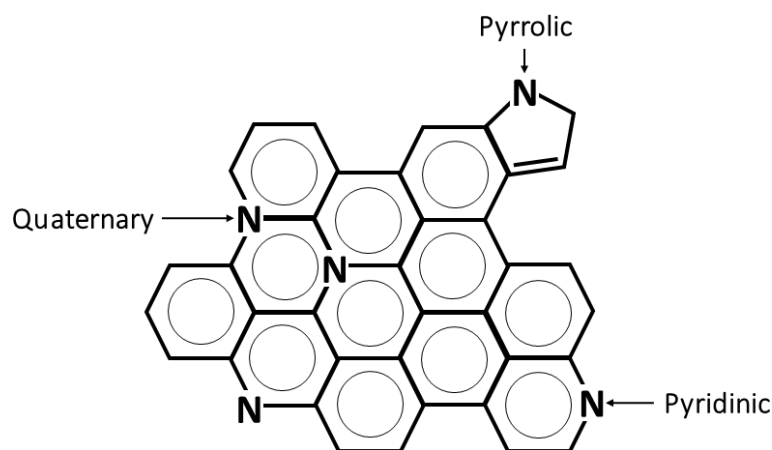


**Fig. 1.2.** Typical carbon structure containing quaternary, pyrrolic, and pyridinic nitrogen groups [21].

In this context, sulphur is a less studied doping heteroatom than N. It is heteroatom used as a dopant in metal-free electrocatalysts due to its exhibit high electrocatalytic activity for the ORR. Sulphur has an electronegativity close to that of carbon ( $d_C = 2.55$  and  $d_S = 2.58$ ), its incorporation into the  $sp^2$  carbon lattice may induce strain and stress, modifying the charge distribution and facilitating the oxygen chemisorption, a necessary step to promote the ORR [21, 61]. Then, replacing carbon with a sulphur atom generates three sulphur species that are active for ORR: i) thiophene S (located at the edge of carbon lattice), ii) graphitic S (inside the lattice structure), and iii) sulphur oxides (Fig. 1.3) [62–64].

For example, Yang *et al.* synthesized S-doped graphene with a similar  $E_{\text{onset}}$  than Pt/C electrocatalyst,  $n = 3.82$ , and limiting current density at 0.7 V/RHE is  $5.34 \text{ mA cm}^{-2}$  [65].

Likewise, the work of Xiang *et al.* synthesized S-doped oxidized acetylene black display good catalytic activity for the ORR ( $E_{\text{onset}}= 0.93$  V/RHE,  $E_{1/2}= 0.71$  V/RHE, and  $n= 3.9$ ) [66].

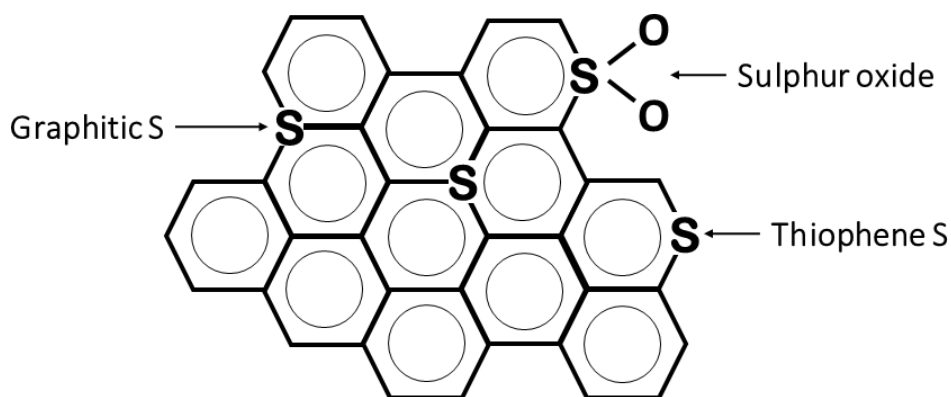


**Fig. 1.3.** Typical carbon structures contain graphitic and thiophene sulphur groups, and sulphur oxide [67].

Heteroatoms co-doping metal-free electrocatalysts have attracted much attention since this is a method to increase catalytic activity. Dual doping of heteroatoms in the carbon lattice was believed to produce a high number of active sites for the ORR. However, it does not guarantee a high catalytic activity, but rather a synergistic effect between the concentration and the spatial distribution of the heteroatoms [68, 69].

The electronegativity of the N/S co-doped structures is more favourable to creating positively charged sites that facilitate the adsorption process of the oxygen surface, which results in a better ORR activity compared to the mono-doped structures [70]. For example, N/S co-doped graphene has shown an enhanced catalytic activity for the ORR than graphene separately doped with S or N heteroatoms [71].

Besides, Yang *et al.* have shown that an N/S co-doped biocarbon generates a  $j$  value between -3 and -4.5 mA cm<sup>-2</sup>, with  $n$  between 3.2 and 3.9, and  $E_{\text{onset}}= 0.88$  V/RHE in alkaline media [72]. Additionally, the report by You *et al.* shows that N/S co-doped carbon nanospheres exhibit high catalytic activity for the ORR ( $E_{\text{onset}}= 0.88$  V/RHE,  $n= 3.82$ ) along with outstanding long-term stability (5% loss after 5.5 h of the test of the limit current density) in an alkaline media [73].

In the same manner, the report by Jiang *et al.* shows N/S co-doped OMC which exhibits high catalytic activity for the ORR ( $E_{\text{onset}}= 0.9$  V/RHE and  $n= 3.95$ ) in alkaline media. After 1500 cycles of the doped-carbon, the long-term stability is better than that of commercial Pt/C [74].

Table 1.1 shows the electrochemical parameters of sulphur and nitrogen doped and co-doped metal-free electrocatalysts for the ORR.

**Table 1.1.** Electrochemical parameters of different metal-free electrocatalysts for the ORR.

Electrocatalyst	Electrochemical parameters			Ref.
	$E_{\text{onset}}$ (V vs RHE)	$E_{1/2}$	n	
N-doped mesoporous nanocarbon	0.92	-- <sup>a</sup>	~4.0	[75]
N-doped carbon from cellulose	0.83	0.81	3.5	[76]
N-doped carbon hollow-tubes	-- <sup>a</sup>	0.82	~4.0	[77]
N-doped graphitic nanofiber	0.74	-- <sup>a</sup>	~4.0	[78]
N-doped carbon nanocages	-- <sup>a</sup>	0.78	~4.0	[79]
N-doped carbon nanospheres	0.95	0.83	~4.0	[80]
S-doped carbon from cassava residues	0.69	-- <sup>a</sup>	3.7	[81]
S-doped carbon spheres	0.88	0.74	3.9	[82]
S-doped reduced graphite oxide	0.85	-- <sup>a</sup>	~4.0	[83]
S-doped hierarchical graphene	0.87	< 0.81	-- <sup>a</sup>	[84]
S-doped carbon nanotubes	0.92	-- <sup>a</sup>	3.71	[85]
S-doped hollow porous carbon sphere	0.70	-- <sup>a</sup>	3.50	[86]
N/S co-doped hard carbon frameworks	0.98	0.82	3.96	[87]
N/S co-doped carbon from polyaniline	0.88	-- <sup>a</sup>	3.7	[88]
N/S co-doped ordered mesoporous carbon	1.02	-- <sup>a</sup>	~4.0	[89]
B/N co-doped hierarchical porous carbon	0.94	0.73	~3.8	[90]
N/F co-doped microporous carbon nanofibers	0.94	0.81	~4.0	[91]
N/P co-doped hollow carbon nanofiber	0.93	0.82	~3.9	[92]
N/S/F tri-doped porous carbon	0.98	0.86	~3.6	[93]

--<sup>a</sup>: not determined

To enhance the ORR activity of the metal-free electrocatalyst, the effect of heteroatoms doping, or the design of structural defects have been studied as well as the control of the chemical surface composition and the fabrication of hierarchical porous structure of the electrocatalysts. The structures used for the ORR include low-dimensional electrocatalysts (zero-dimensional, 0D), one-dimensional (1D), two-dimensional (2D), and three-dimensional (3D) carbon nanostructures [94, 95]. Among 3D carbon nanostructure highlights the ordered mesoporous carbon, with hollow structure, uniform and tunable mesopores size as well as high surface area, have gained enormous attention in energy storage, catalysis, sensors, drug delivery, etc., due to high active surface area, long-term durability, and short diffusion length in applications such as energy-storages devices and electrocatalysts [96, 97].

In comparison with various ordered mesoporous carbon, the Ordered Mesoporous Carbon Hollow Spheres (OMCHS) plays a decisive role in ORR studies. It offers an excellent morphology, high hierarchical surface area ( $\sim 2000 \text{ m}^2 \text{ g}^{-1}$ ), a high number of mesopores, and good electrical conductivity ( $30.2 \text{ S m}^{-1}$ ). However, in some reports, the ORR activity parameters such as  $E_{\text{onset}}$ , current density, and stability of this materials are insufficient when compared with the benchmark electrocatalysts [98, 99]. The electrochemical performance of different heteroatoms-doped OMCHSs are mentioned below.

### 1.2.1. Heteroatoms-doped OMCHS for the ORR

Han *et al.* report that OMCHS promotes the ORR in alkaline media with a catalytic activity like that of commercial Pt/C ( $E_{\text{onset}} = 0.9 \text{ V/RHE}$ ,  $n = 3.8$ ) [100]. Moreover, the investigation by Zhou *et al.* demonstrates that N-doped OMCHS exhibit comparable performance for the ORR to Pt/C ( $E_{\text{onset}} = 0.98 \text{ V/RHE}$ ,  $n = 3.9$ ) [101]. Besides, Qin *et al.* show that hollow mesoporous carbon nitride nanospheres a significantly enhance compared to bulk graphitic carbon nitride electrocatalytic activity ( $E_{\text{onset}} = 0.9 \text{ V/RHE}$ ,  $n = 3.7$ ) [102].

Additionally, the report by Yongyu *et al.* shows that mesoporous carbon hollow spheres promote the ORR in neutral and alkaline electrolyte ( $E_{\text{onset}} = 0.83 \text{ V/RHE}$ ,  $n = 4$ ) [103]. N/S co-doped hollow mesoporous carbon spheres investigated by Yong *et al.* exhibits a high  $E_{1/2}$ , high methanol tolerance, and high long-term durability ( $E_{\text{onset}} = 0.9 \text{ V/RHE}$ ,  $E_{1/2} = 0.85 \text{ V/RHE}$ ,  $n = 3.98$ ) [104]. Xiong *et al.* report that N/S co-doped hollow mesoporous carbon spheres show a good performance for the ORR and electrochemical stability ( $E_{\text{onset}} = 0.85 \text{ V/RHE}$ ,  $E_{1/2} = 0.77 \text{ V/RHE}$ ,  $n = 4$ ) [105].

Moreover, the analysis of N-doped hollow mesoporous carbon nanospheres by Duraisamy *et al.* indicate that electrocatalyst has an outstanding activity toward ORR ( $E_{\text{onset}} = 0.84 \text{ V/RHE}$ ,  $E_{1/2} = 0.83 \text{ V/RHE}$ ,  $n = 4$ ) [106]. Zhongyu *et al.* report that N-doped nano-hollow capsule carbon nanocages obtain and behaved high performance for the ORR and electrochemical stability in alkaline media ( $E_{\text{onset}} = 0.87 \text{ V/RHE}$ ,  $E_{1/2} = 0.73 \text{ V/RHE}$ ,  $n = 3.81$ ) [107]. Also, the investigation by Yan *et al.* show that N-doped hollow carbon polyhedron promotes the ORR in alkaline media with a catalytic activity like that of Pt/C ( $E_{\text{onset}} = 0.98 \text{ V/RHE}$ ,  $E_{1/2} = 0.86 \text{ V/RHE}$ ,  $n = 4$ ) [108]. Moreover, the report by Fan *et al.* N-doped carbon covered hollow carbon nanoparticles exhibit

high performance for the ORR and high long-term stability ( $E_{\text{onset}} = 0.87$  V/RHE,  $E_{1/2} = 0.76$  V/RHE,  $n = 3.7$ ) [109].

On another hand, the heteroatoms-doped OMCHS can be combined with metal-transitions (e.g., Fe, Co, Mo, Ni, etc.) to increase their catalytic activity [110–114]. The study of Xing *et al.* indicates that N-doped OMCHS embedded Co nanoparticles exhibit a high performance for the ORR ( $E_{\text{onset}} = 0.9$  V/RHE,  $E_{1/2} = 0.75$  V/RHE,  $n = 3.94$ ) [115]. The investigation by Su *et al.* show that Fe-N-doped hollow carbon spheres promotes the adsorption/desorption of oxygen and ORR intermediates, improving its catalytic activity [116]. In this context, the design and fabrication strategies play an important role for OMCHS to enhance their ORR performance [96].

### 1.3. Design and fabrication approaches for the synthesis of OMCHS

The synthesis path of the hollow carbon sphere can be classified in: i) soft-template route, which refers to the self-construction of the hollow structure via the use of organic molecules; and ii) hard-template route, based on the employment of a hard core that will be removed after the formation of the shell [117]. Table 1.2 shows the different advantages and disadvantages of soft-template and hard-template routes.

**Table 1.2.** Advantages and disadvantages of soft/hard-template routes [118–121].

Synthesis procedures	Advantages	Disadvantages
Soft-templating	<ul style="list-style-type: none"> <li>• Wide variety of carbon precursors</li> <li>• Template or temple-free strategy</li> <li>• Easily remove template</li> <li>• Relatively simple processes</li> <li>• Relatively high ordered pore arrangement</li> </ul>	<ul style="list-style-type: none"> <li>• Non-uniform in size, morphology</li> <li>• Polydisperse and highly aggregate</li> <li>• Difficulty reaction conditions</li> <li>• Non-uniform pores.</li> </ul>
Hard-templating	<ul style="list-style-type: none"> <li>• Wide variety of carbon precursors</li> <li>• Uniform in size and morphology</li> <li>• Uniform pores (3-10 nm)</li> <li>• High surface areas (<math>\sim 2000</math> m<sup>2</sup> g<sup>-1</sup>)</li> <li>• Inorganic or polymer are used as template</li> </ul>	<ul style="list-style-type: none"> <li>• Difficulty removing the template</li> <li>• Non-environmentally friendly process</li> <li>• Complicated synthetic routes</li> <li>• Less ordered pore arrangement</li> </ul>

The hard-template synthesis of OMCHS is presented in Fig. 1.4. This consists of four steps: i) core formation (e.g., silica-based spheres), ii) covering of core with a source of carbon and heteroatom, iii) carbonization and iv) leaching of silica spheres [122, 123].

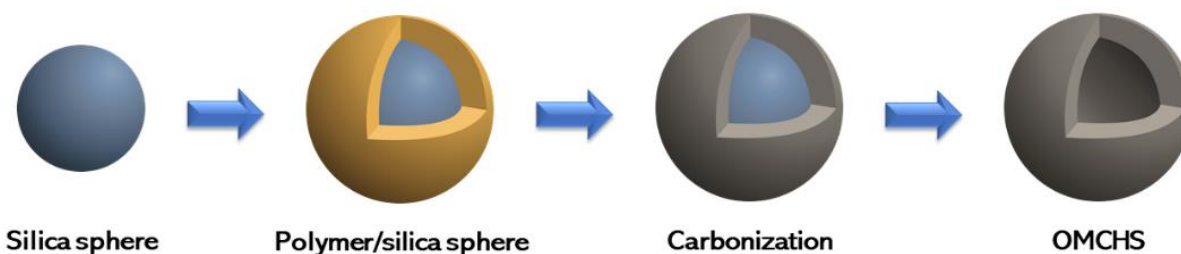


**Fig. 1.4.** Scheme of the synthesis of OMCHS [123].

The formation of silica core spheres can be produced by the hydrolysis and condensation of tetraethyl orthosilicate (TEOS) in the presence of alcohol, water, and a base catalyst. This process is known as the Stöber method [124–126]. The reactions that occur are:

- i) Hydrolysis:  $\equiv \text{Si} - \text{OR} + \text{H}_2\text{O} \leftrightarrow \equiv \text{Si} - \text{OH} + \text{ROH}$
- ii) Alcohol condensation:  $\equiv \text{Si} - \text{OR} + \equiv \text{Si} - \text{OH} \leftrightarrow \equiv \text{Si} - \text{O} - \text{Si} \equiv + \text{ROH}$
- iii) Water condensation:  $\equiv \text{Si} - \text{OH} + \equiv \text{Si} - \text{OH} \leftrightarrow \equiv \text{Si} - \text{O} - \text{Si} \equiv + \text{H}_2\text{O}$  [127].

After the formation of the core silica template, the porous-shell is formed using resorcinol and formaldehyde as carbon sources. The formation of the porous-shell starts with the hydrolysis of TEOS to form silica spheres, which interact with resorcinol-formaldehyde (R-F) oligomers and cetyltrimethylammonium chloride (CTAC) that work as surfactants, forming clusters that have a negative electrostatic charge. The absence of TEOS and CTAC in the synthesis avoids the formation of the shell. Next, the clusters are attracted by  $\text{NH}_4^+$  cations (because this reaction is carried out in alkaline solution) on the surface of the core, fully covering it with silica spheres.

Afterwards, the oligomers are condensed and cross-linked to develop a polymeric shell by the effect of hydrothermal treatment [113, 128, 129, 130]. Fig. 1.5 schematizes the development of the porous-shell. Previously, it was mentioned that OMCHS can be doped with different heteroatoms, therefore several studies indicate that doping is performed while the porous-shell is formed [131–135].

Porous-shell can be doped in two ways: i) *in-situ*, i.e., during their synthesis, or ii) post treatment, after their synthesis [136, 137]. Usually, during *in-situ* procedure, hollow mesoporous carbons can be doped using several sources of nitrogen such as gelatin, ethylenediamine, aniline, melamine-formaldehyde resin, triethanolamine, p-diaminobenzene, polydopamine, dopamine,

pyrrole, diaminobenzene, etc. [129, 138–141]. In the case of S-doped hollow mesoporous carbon, the sulphur sources used are: sulphuric acid, toluenesulfonic acid, poly(3,4-ethylenedioxythiophene), magnesium sulfate, sulfuric acid, thiourea, etc. [134, 142–146].

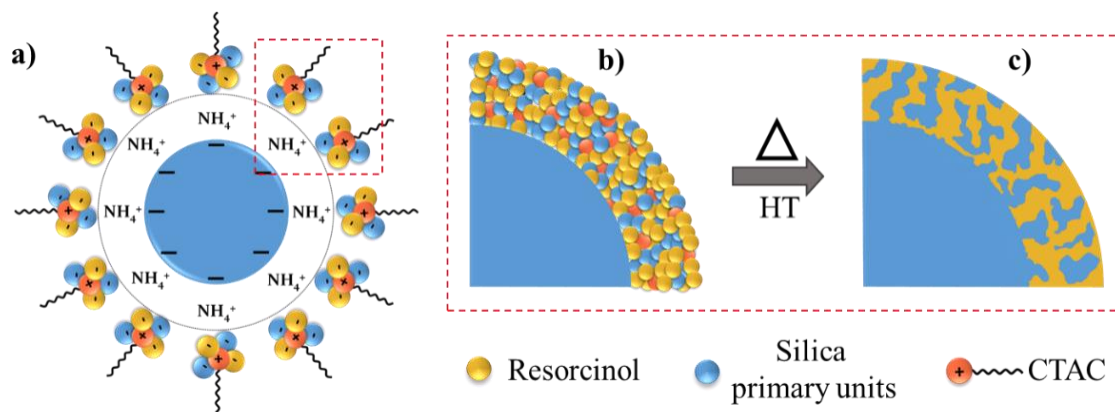


**Fig. 1.5.** a) Electrostatic interactions between R-F/silica primary units/CTAC and the silica cores. b) Polycondensation of polymeric and silica primary units. c) Formation of the shell during the hydrothermal treatment (HT) [122].

In this regard, Kiciński *et al.* have reported the synthesis of N and S doped and co-doped OMCHS, employing 2-pyridinecarboxaldehyde and 2-thiophenecarboxaldehyde as sources of heteroatoms. These compounds can take part in the polycondensation during the polymerization process, facilitating the addition of S and N into the porous shell of OMCHS, generating new or better properties (structural, morphology, textural, and electrochemical) derived from doping with these aldehydes [147, 148].

The mechanism of resorcinol-formaldehyde polymerization that proceeds in the porous-shell formation is shown in Fig. 1.6. This process occurs in 2 steps: i) the substitution of resorcinol with formaldehyde forming a hydroxymethyl derivative mono-, di- or trisubstituted resorcinol in the position ortho or para; and ii) the polycondensation of the intermediate, where hydroxymethyl resorcinol units react between them forming a cluster [149–151].

The polymerization can proceed at room temperature in the absence of catalysts, but the reaction is relatively low. To speed up the polymerization, acid or basic catalysts are used, while the temperature is increased up to 90 °C [125, 150, 152].

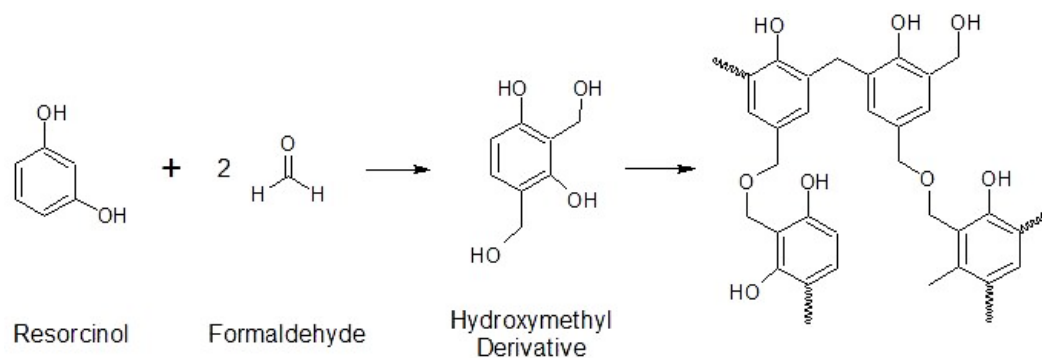


**Fig. 1.6.** The two-step polymerization process of R-F [149, 152].

After the formation of the R-F polymer/silica sphere composite, next step in the synthesis of OMCHS is the carbonization, carried out in oxygen-free or oxygen-limited conditions [153]. Finally, the hard silica sphere core and silica spheres in the shell are leached out with hydrofluoric acid, resulting in hollow spheres with ordered mesoporous walls [154].

#### 1.4. Theoretical study of R-F polymers

Over the past decades, a large amount of theoretical and experimental data has been generated in various areas of knowledge. Such an abundance of information is primarily due to the success of the Density Functional Theory (DFT) and the great advances that have been made in computational capabilities [155, 156].

Because of such success, the design and innovation of novel and inexpensive materials for several applications takes advantages of the knowledge developed by theoretical researchers to characterize their properties and correlate them with those obtained experimentally [157]. Of great relevance is the design of theoretical models, which is a crucial step for the interpretation of the experimental-theoretical results.

One strategy is the direct design of theoretical models, based on calculating the properties and compositions of materials. Generally, direct designs are divided in three categories: i) descriptive (it interprets and confirms experimental evidence), ii) predictive (it predicts properties of novel materials), and iii) predictive for a class of materials (it predicts new functionalities) [158]. On the basis this classification, developing more realistic models of the surface of the OMCHS represents an important advantage in understanding the catalytic activity for the ORR.



OMCHS have experienced an outstanding development owing to their size, morphology, porosity, and chemical properties that can be customized for a specific purpose, depending on the precursors employed during their synthesis [159]. Among the precursors more widely used R-F mixture stand out because OMCHS having high electrical conductivity, high surface area and porosity and three-dimensional nanoarchitecture are easily obtained from them [147, 150]. However, theoretical studies reported in the literature regarding R-F models are scarce.

#### 1.4.1. Theoretical models of the R-F reactions

R-F reactions are important because an important number of materials are obtained from them, having several applications (e.g., catalyst supports, adsorbents, energy storage materials) [160–162]. Therefore, research related to the development of R-F polymers requires a close combination between theoretical and experimental studies, aiming to better understand the correlations among synthesis procedures and structures obtained thereafter [163].

R-F polymers forms when resorcinol undergoes a substitution in its ortho and para sites, allowing up to three formaldehyde units to bind into its ring, generating hydroxymethyl derivatives. Subsequently, these derivatives react in a condensation reaction, resulting in the bridging of methylene and methylene ether compounds through the elimination of water molecules, thus forming a cross-linked polymeric network, as seen in Fig. 1.6 [164–166].

Theoretical models of R-F polymers have been used for different purposes, e.g., Pratt *et al.* reported the molecular modelling of alkaline degradation of R-F polymer exhibit that methylene crosslinks are oxidized to aldehyde or carboxylate groups, i.e., back to form the hydroxymethyl derivatives [167]. Li *et al.* have studied the theoretical R-F condensation reactions [168]. In the same fashion, Choi *et al.* have modeled the influence of hydrogen bonds and the steric hindrance by phenyl groups in the polycondensation of R-F resins [169]. Moreover, Martin *et al.* have described the growth of R-F polymers from monomers leading to the formation of interconnected primary clusters, evaluating their textural and fractal properties [170]. Nevertheless, no detailed model of the R-F polymer or their use to produce OMCHS, focusing on their application for the ORR has been found in the literature.

## Reference

- [1] F. Olsina, R. Pringles, C. Larisson, F. Garcés. Reliability payments to generation capacity in electricity markets. *Energy Policy* 73 (2014) 211–224.
- [2] G. Powells, H. Bulkeley, S. Bell, E. Judson. Peak electricity demand and the flexibility of everyday life. *Geoforum*. 55 (2014) 43–52.
- [3] I. Khan. Greenhouse gas emission accounting approaches in electricity generation systems: A review. *Atmos. Environ.* 200 (2019) 131–141.
- [4] M. Cellura, M. A. Cusenza, S. Longo. Energy-related GHG emissions balances: IPCC versus LCA. *Sci. Total Environ.* 628–629 (2018) 1328–1339.
- [5] M. Su, S. Pauleit, X. Yin, Y. Zheng, S. Chen, C. Xu. Greenhouse gas emission accounting for EU member states from 1991 to 2012. *Appl. Energy.* 184 (2016) 759–768.
- [6] S. Ahmed, M. T. Islam, M. A. Karim, N. M. Karim. Exploitation of renewable energy for sustainable development and overcoming power crisis in Bangladesh. *Renew. Energy* 72 (2014) 223–235.
- [7] V. Mehta J. S. Cooper. Review and analysis of PEM fuel cell design and manufacturing. *J. Power Sources.* 114, (2003) 32–53.
- [8] L. Carrette, K. A. Friedrich, U. Stimming. *Fuel Cells: Principles, Types, Fuels, and Applications*, Chem. Phys. Chem. 1 (2000) 162–193.
- [9] S.F. Lu, J. Pan, A.B. Huang, L. Zhuang, J.T. Lu. Alkaline polymer electrolyte fuel cells completely free from noble metal catalysts. *Proc. Natl. Acad. Sci. U.S.A* 105 (2008) 20611–20614.
- [10] X.W. Dong, J.B. Zhuang, N. Huang, C.H. Liang, L.S. Xu, W. Li, S.C. Zhang, M. Sun. Development of anion-exchange membrane for anion-exchange membrane fuel cells. *Mater. Res. Innov.* 19 (2015) S638–S641.
- [11] C.G. Arges, V. K. Ramani, P. N. Pintauro. The Chalkboard: Anion Exchange Membrane Fuel Cells. *Electrochem. Soc. Interface.* 19 (2010) 31.
- [12] D. Niblett, A. Mularczyk, V. Niasar, J. Eller, S. Holmes. Two-phase flow dynamics in a gas diffusion layer-gas channel-microporous layer system. *J. Power Sources.* 471 (2020) 228427.
- [13] J. Sim, M. Kang, K. Min. Effects of basic gas diffusion layer components on PEMFC performance with capillary pressure gradient. *Int. J. Hydrog. Energy.* 46 (2021) 27731–27748.
- [14] J.R. Varcoe, R.C.T. Slade. Prospects for alkaline anion-exchange membranes in low temperature fuel cells. *Fuel Cells.* 5 (2005) 187–200.
- [15] M. Hren, M. Božič, D. Fakin, K. S. Kleinschek, S. Gorgieva. Alkaline membrane fuel cells: anion exchange membranes and fuels. *Sustain. Energy Fuels.* 5 (2021) 604–637.
- [16] Z.F. Pan, L. An, T. S. Zhao, Z.K. Tang. Advances and challenges in alkaline anion exchange membrane fuel cells. *Prog. Energy Combust. Sci.* 66 (2018) 141–175.
- [17] J.R. Varcoe, P. Atanassov, D. Dekel, A. Herring, M. Hickner, P. Kohl, A. Kucernak, W. Mustain, K. Nijmeijer, K. Scott, T. Xu, L. Zhuang. Anion-exchange membranes in electrochemical energy systems. *Energy Environ. Sci.* 7 (2014) 3135–3191.
- [18] N. Lingappan, B. Li, T.H. Lee, Y.H. Lee. Designing bifunctional catalysts for oxygen reduction/evolution reactions for high efficiency and long lifetime. *Electrochim. Acta.* 313 (2019) 41–47.
- [19] H. Wang, M. Zhou, P. Choudhury, H. Luo. Perovskite oxides as bifunctional oxygen electrocatalysts for oxygen evolution/reduction reactions—A mini review. *Appl. Mater. Today.* 16 (2019) 56–71.
- [20] J. Wei, P. Liang, X. Huang. Recent progress in electrodes for microbial fuel cells. *Bioresour. Technol.* 102 (2011) 9335–9344.
- [21] D. Wang, D. Su. Heterogeneous nanocarbon materials for oxygen reduction reaction. *Energy and Environ. Sci.* 7 (2014) 576–591.
- [22] M. Sun, H. Liu, Y. Liu, J. Qu, J. Li. Graphene-based transition metal oxide nanocomposites for the oxygen reduction reaction. *Nanoscale* 7 (2015) 1250–1269.

- [23] M. I. Awad, T. Ohsaka. An electrocatalytic oxygen reduction by copper nanoparticles-modified Au(100)-rich polycrystalline gold electrode in 0.5 M KO.H J. Power Sources. 226 (2013) 306–312.
- [24] Y. Nie, L. Li, Z. Wei. Recent advancements in Pt and Pt-free catalysts for oxygen reduction reaction. Chem. Soc. Rev. 44 (2015) 2168–2201.
- [25] C. Yang. Preparation and characterization of electrochemical properties of air cathode electrode. Int. J. Hydrog. Energy. 29 (2004) 135–143.
- [26] Z. Yan, M. Wang, B. Huang, J. Zhao, and R. Liu, “Carboxyl multi-wall carbon nanotubes supported Pt-Ni alloy nanoparticles as cathode catalyst for microbial fuel cells,” Int. J. Electrochem. Sci. 7 (2012) 10825–10834.
- [27] N. Zhu, J. Huang, W. Shen, L. Tu, P. Wu, H. Ma. Carboxylic carbon nanotube: Catalyst support material and oxygen reduction reaction of microbial fuel cells. Int. J. Electrochem. Sci. 10 (2015) 2634–2645.
- [28] T. Zhou, R. Ma, Y. Zhou, R. Xing, Q. Liu, Y. Zhu, J. Wang. Efficient N-doping of hollow core-mesoporous shelled carbon spheres via hydrothermal treatment in ammonia solution for the electrocatalytic oxygen reduction reaction. Microporous and Mesoporous Mater. 261 (2017) 88–97.
- [29] X. Long, D. Li, B. Wang, Z. Jiang, W. Xu, B. Wang, D. Yang, Y. Xia. Heterocyclization Strategy for Construction of Linear Conjugated Polymers: Efficient Metal-Free Electrocatalysts for Oxygen Reduction. Angew. Chem. Int. Ed. 58 (2019) 11369–11373.
- [30] Z. Lu, D. Chang, J. Ma, G. Huang, L. Cai, L. Zhang. Behavior of metal ions in bioelectrochemical systems: A review. J. Power Sources. 275 (2015) 243–260.
- [31] T. Mittermeier, A. Weiß, H. A. Gasteiger, F. Hasché. Monometallic Palladium for Oxygen Reduction in PEM Fuel Cells: Particle-Size Effect, Reaction Mechanism, and Voltage Cycling Stability. J. Electrochem. Soc. 164 (2017) F1081–F1089.
- [32] J. Suntivich, Y. Shao-Horn. Trend in Oxygen Reduction Reaction on Transition Metal Oxide Surfaces. ECS Transactions. 58 (2013) 715–726.
- [33] S. Gupta, W. Kellogg, H. Xu, X. Liu, J. Cho, G. Wu. Bifunctional Perovskite Oxide Catalysts for Oxygen Reduction and Evolution in Alkaline Media. Asian J. Chem. 11 (2016) 10–21.
- [34] W. Chu, D. Higgins, Z. Chen. R. Cai. Non-precious Metal Oxides and Metal Carbides for ORR in Alkaline-Based Fuel Cells. Non-Noble Metal Fuel Cell Catalysts. (2014) 357–388.
- [35] F. Charretre, F. Jaouen, S. Ruggeri, J. P. Dodelet. Fe/N/C non-precious catalysts for PEM fuel cells: Influence of the structural parameters of pristine commercial carbon blacks on their activity for oxygen reduction. Electrochim. Acta. 53 (2008) 2925–2938.
- [36] . Li Tao, M. Qiao, R. Jin, Y. Li, Z. Xiao, Y. Wang, N. Zhang, C. Xie, Q. He, D. Jiang, G. Yu, Y. Li, S. Wang. Bridging the Surface Charge and Catalytic Activity of a Defective Carbon Electrocatalyst. Angew. Chem. 131 (2019) 1031–1036.
- [37] S. Wang, D. Yu, L. Dai, Polyelectrolyte functionalized carbon nanotubes as efficient metal-free electrocatalysts for oxygen reduction. J. Am. Chem. Soc. 133 (2011) 5182–5185.
- [38] L. Yang, J. Shui, L. Du, Y. Shao, J. Liu, L. Dai, Z. Hu. Carbon-Based Metal-Free ORR Electrocatalysts for Fuel Cells: Past, Present, and Future. Adv. Mater. 31 (2019) 1804799.
- [39] J. Lee, J. Lim, S. O. Kim, W. J. Lee, J. Lim, S. O. Kim. Nitrogen Dopants in Carbon Nanomaterials: Defects or a New Opportunity. Small Methods. 1 (2017) 1600014.
- [40] Y. Jia, K. Jiang, H. Wang, X. Yao. The Role of Defect Sites in Nanomaterials for Electrocatalytic Energy Conversion. Chem. 5 (2019) 1371–1397.
- [41] X. Zhao, X. Zou, X. Yan, C. Brown, Z. Chen, G. Zhub, X. Yao, Defect-driven oxygen reduction reaction (ORR) of carbon without any element doping. Inorg. Chem. Front. 3 (2016) 417–421.
- [42] J. Zhang, J. Zhang, F. He, Y. Chen, J. Zhu, D. Wang, S. Mu, H. Yang. Defect and Doping Co-Engineered Non-Metal Nanocarbon ORR Electrocatalyst. Nano-Micro Lett. 13 (2021) 1–30.
- [43] Y. Zhang, L. Guo, L. Tao, Y. Lu, S. Wang. Defect-Based Single-Atom Electrocatalysts. Small Methods. 3 (2019) 1800406

- [44] C. Xie, D. Yan, W. Chen, Y. Zou, R. Chen, S. Zang, Y. Wang, X. Yao, S. Wang. Insight into the design of defect electrocatalysts: From electronic structure to adsorption energy. *Mater. Today*. 31 (2019) 47–68.
- [45] R. Ma, G. Lin, Y. Zhou, Q. Liu, T. Zhang, G. Shan, M. Yang, J. Wang. A review of oxygen reduction mechanisms for metal-free carbon-based electrocatalysts. *NPJ Comput. Mater.* 5 (2019) 1–15.
- [46] Y. P. Zhu, C. Guo, Y. Zheng, S. Z. Qiao. Surface and Interface Engineering of Noble-Metal-Free Electrocatalysts for Efficient Energy Conversion Processes. *Acc. Chem. Res.* 50 (2017) 915–923.
- [47] Q. Wu, Q. Liu, Y. Zhou, Y. Sun, J. Zhao, Y. Liu, F. Liu, M. Nie, F. Ning, X. Jiang, X. Zhou, J. Zhong, Z. Kang. Carbon Defect-Induced Reversible Carbon-Oxygen Interfaces for Efficient Oxygen Reduction. *ACS Appl. Mater. Interfaces* 10 (2018) 39735–39744.
- [48] F. Dong, M. Wu, G. Zhang, X. Liu, D. Rawach, A. Tavares, S. Sun. Defect Engineering of Carbon-based Electrocatalysts for Rechargeable Zinc-air Batteries. *Chem. Asian J.* 15 (2020) 3737–3751.
- [49] L. Yang, J. Shui, L. Du, Y. Shao, J. Liu, L. Dai, Z. Hu. Carbon-Based Metal-Free ORR Electrocatalysts for Fuel Cells: Past, Present, and Future. *Adv. Mater.* 31 (2019) 1804799.
- [50] C. Zhang, L. Hou, C. Cheng, Z. Zhuang, F. Zheng, W. Chen. Nitrogen and Phosphorus Co-doped Hollow Carbon Spheres as Efficient Metal-Free Electrocatalysts for the Oxygen Reduction Reaction. *Chem. Electro. Chem.* 5 (2018) 1891–1898.
- [51] Q. Zhang, F. Luo, Y. Ling, L. Guo, K. Qu, H. Hu, Z. Yang, W. Cai, H. Cheng. Constructing Successive Active Sites for Metal-free Electrocatalyst with Boosted Electrocatalytic Activities Toward Hydrogen Evolution and Oxygen Reduction Reactions. *Chem. Cat. Chem.* 10 (2018) 5194–5200.
- [52] R. Xing, T. Zhou, Y. Zhou, R. Ma, Q. Liu, J. Luo, J. Wang. Creation of Triple Hierarchical Micro-Meso-Macroporous N-doped Carbon Shells with Hollow Cores Toward the Electrocatalytic Oxygen Reduction Reaction. *Nano-Micro Lett.* 10 (2018) 3.
- [53] D. Gu, Y. Zhou, R. Ma, F. Wang, Q. Liu, J. Wang. Facile Synthesis of N-Doped Graphene-Like Carbon Nanoflakes as Efficient and Stable Electrocatalysts for the Oxygen Reduction Reaction. *Nano-Micro Lett.* 10 (2018) 29.
- [54] X. Bao, D. von Deak, E. J. Biddinger, U. S. Ozkan, C. M. Hadad. A computational exploration of the oxygen reduction reaction over a carbon catalyst containing a phosphinate functional group. *Chem. Comm.* 46 (2010) 8621–8623.
- [55] H. Wang, T. Maiyalagan, X. Wang. Review on recent progress in nitrogen-doped graphene: Synthesis, characterization, and its potential applications. *ACS Catal.* 2 (2012) 781–794.
- [56] Y. Zhang, K. Fugane, T. Mori, L. Niu, J. Ye. Wet chemical synthesis of nitrogen-doped graphene towards oxygen reduction electrocatalysts without high-temperature pyrolysis. *J. Mater. Chem.* 22 (2012) 6575–6580.
- [57] C. Zhang, R. Hao, H. Liao, Y. Hou. Synthesis of amino-functionalized graphene as metal-free catalyst and exploration of the roles of various nitrogen states in oxygen reduction reaction. *Nano Energy.* 2 (2013) 88–97.
- [58] L. Qu, Y. Liu, J. B. Baek, L. Dai. Nitrogen-doped graphene as efficient metal-free electrocatalyst for oxygen reduction in fuel cells. *ACS Nano.* 4 (2010) 1321–1326.
- [59] Z. Chen, D. Higgins, H. Tao, R. S. Hsu, Z. Chen. Highly Active Nitrogen-Doped Carbon Nanotubes for Oxygen Reduction Reaction in Fuel Cell Applications. *J. Phys. Chem. C*, 113 (2019) 21008–21013.
- [60] S. Chen, J. Bi, Y. Zhao, L. Yang, C. Zhang, Y. Ma, Q. Wu, X. Wang, Z. Hu. Nitrogen-Doped Carbon Nanocages as Efficient Metal-Free Electrocatalysts for Oxygen Reduction Reaction. *Adv. Mater.* 24 (2012) 5593–5597.
- [61] X. Ge, A. Sumboja, D. Wu, T. An, B. Li, F.W.T. Goh, T.S. Andy Hor, Y. Zong, Z. Liu. Oxygen Reduction in Alkaline Media: From Mechanisms to Recent Advances of Catalysts,” *ACS Catalysis*, vol. 5, no. 8, pp. 4643–4667, Aug. 2015, doi: 10.1021/acscatal.5b00524.
- [62] S. Yang, L. Zhi, K. Tang, X. Feng, J. Maier, K. Müllen. Efficient synthesis of heteroatom (N or S)-doped graphene based on ultrathin graphene oxide-porous silica sheets for oxygen reduction reactions. *Adv. Funct. Mater.* 22 (2012) 3634–3640.

- [63] J.E. Park, Y. Jang, Y. Kim, M. Song, S. Yoon, D. Kim, S. Kim. Sulfur-doped graphene as a potential alternative metal-free electrocatalyst and Pt-catalyst supporting material for oxygen reduction reaction. *Phys. Chem. Chem. Phys.* 16 (2014) 103–109.
- [64] Z. Lu, S. Li, C. Liu, C. He, X. Yang, D. Ma, G. Xu, Z. Yang. Sulfur doped graphene as a promising metal-free electrocatalyst for oxygen reduction reaction: a DFT-D study. *RSC Adv.* 7 (2017) 20398–20405.
- [65] Z. Yang, Z. Yao, G. Li, G. Fang, H. Nie, Z. Liu, X. Zhou, X. Chen, S. Huang. Sulfur-doped graphene as an efficient metal-free cathode catalyst for oxygen reduction. *ACS Nano.* 6 (2012) 205–211.
- [66] Q. Xiang, X. Zou, Y. Qiang, B. Hu, Y. Cen, C. Xu, L. Liu, Y. Zhou, C. Chen. Self-assembly porous metal-free electrocatalysts templated from sulfur for efficient oxygen reduction reaction. *Appl. Surf. Sci.* 462 (2018) 65–72.
- [67] L. Zhang, J. Niu, M. Li, Z. Xia. Catalytic mechanisms of sulfur-doped graphene as efficient oxygen reduction reaction catalysts for fuel cells. *J. Phys. Chem. C.* 118 (2014) 3545–3553.
- [68] C. Zhang, L. Hou, C. Cheng, Z. Zhuang, F. Zheng, W. Chen. Nitrogen and Phosphorus Co-doped Hollow Carbon Spheres as Efficient Metal-Free Electrocatalysts for the Oxygen Reduction Reaction. *Chem. Electro. Chem.* 5 (2018) 1891–1898.
- [69] X. Duan, K. O'Donnell, H. Sun, Y. Wang, S. Wang. Sulfur and Nitrogen Co-Doped Graphene for Metal-Free Catalytic Oxidation Reactions. *Small.* 11 (2015) 3036–3044.
- [70] J. Chattopadhyay, T. S. Pathak, D. Pak. Heteroatom-Doped Metal-Free Carbon Nanomaterials as Potential Electrocatalysts. *Molecules.* 27 (2022) 670.
- [71] J. Liang, Y. Jiao, M. Jaroniec, S. Z. Qiao. Sulfur and nitrogen dual-doped mesoporous graphene electrocatalyst for oxygen reduction with synergistically enhanced performance. *Angew. Chemie. Int. Ed.* 51 (2012) 11496–11500.
- [72] S. Yang, X. Mao, Z. Cao, Y. Yin, Z. Wang, M. Shi, H. Dong. Onion-derived N, S self-doped carbon materials as highly efficient metal-free electrocatalysts for the oxygen reduction reaction. *Appl. Surf. Sci.* 427 (2018) 626–634.
- [73] C. You, S. Liao, H. Li, S. Hou, H. Peng, X. Zeng, F. Liu, R. Zheng, Z. Fu, Y. Li. Uniform nitrogen and sulfur co-doped carbon nanospheres as catalysts for the oxygen reduction reaction. *Carbon.* 69 (2014) 294–301.
- [74] T. Jiang, Y. Wang, K. Wang, Y. Liang, D. Wu, P. Tsiakaras, S. Song. A novel sulfur-nitrogen dual doped ordered mesoporous carbon electrocatalyst for efficient oxygen reduction reaction. *Appl. Catal. B.* 189 (2016) 1–11.
- [75] D. W. Kim, S. Heo, J. S. Lee, S. Y. Lim. Metal-free, NH<sub>3</sub>-activated N-doped mesoporous nanocarbon electrocatalysts for the oxygen reduction reaction. *Electrochem. Commun.* 129, (2021) 107092.
- [76] A. Wütscher, T. Eckhard, D. Hiltrop, K. Lotz, W. Schuhmann, C. Andronescu, M. Muhler. Nitrogen-Doped Metal-Free Carbon Materials Derived from Cellulose as Electrocatalysts for the Oxygen Reduction Reaction. *Chem. Electro. Chem.* 6 (2019) 514–521.
- [77] M. Zhu, P. Xie, L. F. Fan, M. Z. Rong, M. Q. Zhang, Z. P. Zhang. Performance improvement of N-doped carbon ORR catalyst via large through-hole structure. *Nanotechnology.* 31 (2020) 335717.
- [78] H. Tang, W. Chen, J. Wang, T. Dugger, L. Cruz, D. Kisailus. Electrocatalytic N-Doped Graphitic Nanofiber–Metal/Metal Oxide Nanoparticle Composites. *Small.* 14 (2018) 1703459.
- [79] N. Jia, Q. Weng, Y. Shi, X. Shi, X. Chen, P. Chen, Z. An, Y. Chen. N-doped carbon nanocages: Bifunctional electrocatalysts for the oxygen reduction and evolution reactions. *Nano Res.* 11 (2018) 1905–1916.
- [80] T. Jiang, W. Jiang, Y. Li, Y. Xu, M. Zhao, M. Deng, Y. Wang. Facile regulation of porous N-doped carbon-based catalysts from covalent organic frameworks nanospheres for highly-efficient oxygen reduction reaction. *Carbon.* 180 (2021) 92–100.
- [81] C. J. Mena-Durán, I. L. Alonso-Lemus, P. Quintana, R. Barbosa, L. C. Ordoñez, B. Escobar. Preparation of metal-free electrocatalysts from cassava residues for the oxygen reduction reaction: A sulfur functionalization approach. *Int. J. Hydrog. Energy.* 43 (2018) 3172–3179.

- [82] Y. Sun, J. Wu, J. Tian, C. Jin, R. Yang. Sulfur-doped carbon spheres as efficient metal-free electrocatalysts for oxygen reduction reaction. *Electrochim. Acta.* 178 (2015) 806–812.
- [83] M. Seredych, T. J. Bandosz. Confined space reduced graphite oxide doped with sulfur as metal-free oxygen reduction catalyst *Carbon* 66 (2014) 227–233.
- [84] Z. J. Peng, J. Zhao, L. Gu, X. Sun, H. Jia, M. Guan, S. Ma. S-Doped hierarchical graphene decorated with Co-porphyrins as an efficient electrocatalyst for zinc–air batteries. *New J. Chem.* 44 (2020) 14343–14349.
- [85] W. Li, D. Yang, H. Chen, Y. Gao, H. Li. Sulfur-doped carbon nanotubes as catalysts for the oxygen reduction reaction in alkaline medium. *Electrochim. Acta.* 165 (2015) 191–197.
- [86] G. Chen, J. Liu, Q. Li, P. Guan, X. Yu, L. Xing, J. Zhang, R. Che. A direct H<sub>2</sub>O<sub>2</sub> production based on hollow porous carbon sphere-sulfur nanocrystal composites by confinement effect as oxygen reduction electrocatalysts. *Nano Res.* 12 (2019) 2614–2622.
- [87] R. Jiao, W. Zhang, H. Sun, Z. Zhu, Z. Yang, W. Liang, A. Li. N- and S-doped nanoporous carbon framework derived from conjugated microporous polymers incorporation with ionic liquids for efficient oxygen reduction reaction. *Mater Today Energy*, 16 (2020) 100382.
- [88] K. P. Singh, M. Y. Song, J. S. Yu. Iodine-treated heteroatom-doped carbon: conductivity driven electrocatalytic activity. *J. Mater. Chem. A.* 2 (2014) 18115–18124.
- [89] L. Samiee, S. S. Hassani. N and S Co-doped Ordered Mesoporous Carbon: An Efficient Electrocatalyst for Oxygen Reduction Reaction in Microbial Fuel Cells. *Curr. Nanosci.* 16 (2019) 625–638.
- [90] F. Wang, J. Ren, Z. Zheng, Q. Liu, C. yang Zhang. Metal-Free B, N co-Doped Hierarchical Porous Carbon Electrocatalyst with an Excellent O<sub>2</sub> Reduction Performance. *ChemistryOpen.* 10 (2021) 713–719.
- [91] T. Gong, R. Qi, X. Liu, H. Li, Y. Zhang. N, F Co-doped Microporous Carbon Nanofibers as Efficient Metal-Free Electrocatalysts for ORR. *Nano-Micro Lett.* 11 (2019) 1–11.
- [92] Y. Gao, Z. Xiao, D. Kong, R. Iqbal, Q. H. Yang, L. Zhi. N, P co-doped hollow carbon nanofiber membranes with superior mass transfer property for trifunctional metal-free electrocatalysis. *Nano Energy.* 64 (2019) 103879.
- [93] Y. Lv, L. Yang, D. Cao. Sulfur, Nitrogen and Fluorine Triple-Doped Metal-Free Carbon Electrocatalysts for the Oxygen Reduction Reaction. *Chem. Electro. Chem.* 6 (2019) 741–747.
- [94] X. Wang, Z. Kong, J. Ye, C. Shao, B. Li. Hollow nitrogen-doped carbon nanospheres as cathode catalysts to enhance oxygen reduction reaction in microbial fuel cells treating wastewater. *Environ. Res.* 201 (2021) 111603.
- [95] T. Zhou, R. Ma, Y. Zhou, R. Xing, Q. Liu, Y. Zhu, J. Wang. Efficient N-doping of hollow core-mesoporous shelled carbon spheres via hydrothermal treatment in ammonia solution for the electrocatalytic oxygen reduction reaction. *Micropor. Mesopor. Mater.* 261 (2018) 88–97.
- [96] C. Zhang, J. Li, C. Li, W. Chen, C. Guo. Surface and interface engineering of hollow carbon sphere-based electrocatalysts for the oxygen reduction reaction. *J. Mater. Chem. A.* 9 (2021) 25706–25730.
- [97] T. Li, B. Ding, V. Malagras, J. Na, Z. Qin, X. Lu, Y. Bando, H. Nara, Z. Alothman, J. Wang, Y. Yamauchi. Hollow carbon architectures with mesoporous shells via self-sacrificial templating strategy using metal-organic frameworks. *Chem. Eng. J.* 420 (2021) 127635.
- [98] H. Xu, X. Yin, Z. Li, C. Liu, Z. Wang, M. Li, L. Zhang, L. Cheng. Tunable dielectric properties of mesoporous carbon hollow microspheres via textural properties. *Nanotechnology.* 29 (2018) 184003.
- [99] S. Liang, Y. Qin, W. Gao, M. Wang. A lightweight polyurethane-carbon microsphere composite foam for electromagnetic shielding. *E-Polym.* 22 (2022) 223–233.
- [100] C. Han, S. Wang, J. Wang, M. Li, J. Deng, H. Li, Y. Wang. Controlled synthesis of sustainable N-doped hollow core-mesoporous shell carbonaceous nanospheres from biomass. *Nano Res.* 7 (2014) 1809–1819.
- [101] T. Zhou, Y. Zhou, R. Ma, Z. Zhou, G. Liu, Q. Liu, Y. Zhu, J. Wang. Nitrogen-doped hollow mesoporous carbon spheres as a highly active and stable metal-free electrocatalyst for oxygen reduction. *Carbon.* 114 (2017) 177–186.

- [102] Y. Qin, J. Li, J. Yuan, Y. Kong, Y. Tao, F. Lin, S. Li. Hollow mesoporous carbon nitride nanosphere/three-dimensional graphene composite as high efficient electrocatalyst for oxygen reduction reaction. *J. Power Sources*. 272 (2014) 696–702.
- [103] Y. Pang, K. Wang, H. Xie, Y. Sun, M. M. Titirici, G. L. Chai. Mesoporous Carbon Hollow Spheres as Efficient Electrocatalysts for Oxygen Reduction to Hydrogen Peroxide in Neutral Electrolytes. *ACS Catal.* 10 (2020) 7434–7442.
- [104] Y. Zheng, S. Chen, K. Zhang, J. Guan, X. Yu, W. Peng, H. Song, J. Zhu, J. Xu, X. Fan, C. Zhang, T. Liu. Template-free construction of hollow mesoporous carbon spheres from a covalent triazine framework for enhanced oxygen electroreduction. *J. Colloid Interface Sci.* 608 (2022) 3168–3177.
- [105] W. Xiong, H. Li, R. Cao. Nitrogen and sulfur dual-doped hollow mesoporous carbon spheres as efficient metal-free catalyst for oxygen reduction reaction. *Inorg. Chem. Commun.* 114 (2020) 107848.
- [106] V. Duraisamy, R. Krishnan, S. M. Senthil Kumar. N-Doped Hollow Mesoporous Carbon Nanospheres for Oxygen Reduction Reaction in Alkaline Media. *ACS Appl. Nano Mater.* 3 (2020) 8875–8887.
- [107] Z. Qiu, N. Huang, X. Ge, J. Xuan, P. Wang. Preparation of N-doped nano-hollow capsule carbon nanocage as ORR catalyst in alkaline solution by PVP modified F127. *Int. J. Hydrog. Energy.* 45 (2020) 8667–8675.
- [108] J. Yan, X. Zheng, C. Wei, Z. Sun, K. Zeng, L. Shen, J. Sun, M. Rummeli, R. Yang. Nitrogen-doped hollow carbon polyhedron derived from salt-encapsulated ZIF-8 for efficient oxygen reduction reaction. *Carbon.* 171 (2021) 320–328.
- [109] M. Fan, X. Pan, W. Lin, H. Zhang. Carbon-Covered Hollow Nitrogen-Doped Carbon Nanoparticles and Nitrogen-Doped Carbon-Covered Hollow Carbon Nanoparticles for Oxygen Reduction. *ACS Appl. Nano Mater.* 3 (2020) 3487–3493.
- [110] X. Wu, S. Li, B. Wang, J. Liu, M. Yu. Mesoporous NiCo based nanowire arrays supported on three-dimensional N-doped carbon foams as non-noble catalysts for efficient oxygen reduction reaction. *Micropo. Mesopo. Mater.* 231 (2016) 128–137.
- [111] Y. Guo, J. Tang, J. Henzie, B. Jiang, H. Qian, Z. Wang, H. Tan, Y. Bando, Y. Yamamuchi. Assembly of hollow mesoporous nanoarchitectures composed of ultrafine Mo<sub>2</sub>C nanoparticles on N-doped carbon nanosheets for efficient electrocatalytic reduction of oxygen. *Mater. Horiz.* 4 (2017) 1171–1177.
- [112] Q. Gao, Q. Lai, Y. Liang. Iron–nitrogen co-doped hollow carbon sphere with mesoporous structure for enhanced oxygen reduction reaction. *RSC Adv.* 5 (2015) 103302–103307.
- [113] T. Jiang, W. Luan, Y. Ren, C. Fan, Q. Feng, L. Turyanska. Synergistic heat treatment derived hollow-mesoporous-microporous Fe–N–C-SHT electrocatalyst for oxygen reduction reaction. *Micropo. Mesopo. Mater.* 305 (2020) 110382.
- [114] F. Hu, H. Yang, C. Wang, Y. Zhang, H. Lu, Q. Wang. Co-N-Doped Mesoporous Carbon Hollow Spheres as Highly Efficient Electrocatalysts for Oxygen Reduction Reaction. *Small.* 13 (2017) 1602507.
- [115] R. Xing, Y. Zhou, R. Ma, Q. Liu, J. Luo, M. Yang, J. Wang. Nitrogen-Doped Hollow Carbon Spheres with Embedded Co Nanoparticles as Active Non-Noble-Metal Electrocatalysts for the Oxygen Reduction Reaction. *C.* 4 (2018) 11.
- [116] P. Su, W. Huang, J. Zhang, U. Guharoy, Q. Du, Q. Sun, Q. Jiang, Y. Cheng, J. Yang, X. Zhang, Y. Liu, S. Jiang, J. Liu. Fe atoms anchored on defective nitrogen doped hollow carbon spheres as efficient electrocatalysts for oxygen reduction reaction. *Nano Res.* 14 (2020) 1069–1077.
- [117] S. Li, A. Pasc, V. Fierro, A. Celzard. Hollow carbon spheres, synthesis, and applications—a review. *J. Mater. Chem. A.* 4 (2016) 12686–12713.
- [118] T. Liu, L. Zhang, B. Cheng, J. Yu. Hollow Carbon Spheres and Their Hybrid Nanomaterials in Electrochemical Energy Storage. *Adv. Energy Mater.* 9 (2019) 1803900.
- [119] Z.J. Shi, M.G. Ma. Synthesis, Structure, and Applications of Lignin-Based Carbon Materials: A Review. *Sci. Adv. Mater.* 11 (2018) 18–32.
- [120] J. Lee, J. Kim, T. Hyeon. Synthesis of new nanostructured carbon materials using silica nanostructured templates by Korean research groups. *Int. J. Nanotechnol.* 3 (2006) 253–279.

- [121] Y. Zhao, M. Chen, L. Wu. Recent progress in hollow sphere-based electrodes for high-performance supercapacitors. *Nanotechnology*. 27 (2016) 342001.
- [122] S. Mezzavilla, C. Baldizzone, K. J. J. Mayrhofer, F. Schüth. General Method for the Synthesis of Hollow Mesoporous Carbon Spheres with Tunable Textural Properties. *ACS Appl. Mater Inter.* 7 (2015) 12914–12922.
- [123] F. Xu, Z. Tang, S. Huang, L. Chen, Y. Liang, W. Mai, H. Zhong, R. Fu, D. Wu. Facile synthesis of ultrahigh-surface-area hollow carbon nanospheres for enhanced adsorption and energy storage. *Nat. Commun.* 6 (2015) 7221 (2015).
- [124] J. Liu, S. Qiao, H. Liu, J. Orpe, D. Zhao, G. Lu. Revisiting the Stöber method: Inhomogeneity in silica shells. *J. Am. Chem Soc.* 133 (2011) 11422–11425.
- [125] J. Liu, S. Qiao, H. Liu, J. Orpe, D. Zhao, G. Lu. Extension of the stöber method to the preparation of monodisperse resorcinol-formaldehyde resin polymer and carbon spheres. *Angew. Chem. Int. Ed.* 50 (2011) 5947–5951.
- [126] K. Nozawa, H. Gaihanou, L. Raison, P. Panizza, H. Ushiki, E. Sellier, J.P. Delville, and M.H: Delville. Smart control of monodisperse stöber silica particles: Effect of reactant addition rate on growth process. *Langmuir*. 21 (2005) 1516–1523.
- [127] D. Zeng, H. Zhang, B. Wang, K. Sang, J. Yang. Effect of Ammonia Concentration on Silica Spheres Morphology and Solution Hydroxyl Concentration in Stöber Process. *J. Nanosci. Nanotechnol.* 15, (2015) 7407–7411.
- [128] Y. Li, T. Li, M. Yao, S. Liu. Metal-free nitrogen-doped hollow carbon spheres synthesized by thermal treatment of poly( $\sigma$ -phenylenediamine) for oxygen reduction reaction in direct methanol fuel cell applications. *J. Mater. Chem.* 22, (2012) 10911–10917.
- [129] C. Liu, J. Wang, J. Li, M. Zeng, R. Luo, J. Shen, X. Sun, W. Han, L. Wang. Synthesis of N-Doped Hollow-Structured Mesoporous Carbon Nanospheres for High-Performance Supercapacitors. *ACS Appl. Mater. Interfaces.* 8 (2016) 7194–7204.
- [130] H. Zhang, O. Noonan, X. Huang, Y. Yang, C. Xu, L. Zhou, C. Yu. Surfactant-Free Assembly of Mesoporous Carbon Hollow Spheres with Large Tunable Pore Sizes. *ACS Nano* 10 (2016) 4579–4586.
- [131] J. Du, L. Liu, Y. Yu, Z. Hu, B. Liu, A. Chen. N-Doped Hollow Carbon Spheres/Sheets Composite for Electrochemical Capacitor. *ACS Appl. Mater. Interfaces.* 10 (2018) 40062–40069.
- [132] T. Yang, J. Liu, R. Zhou, Z. Chen, H. Xu, S. Qiao, M. Monteiro. N-doped mesoporous carbon spheres as the oxygen reduction reaction catalysts. *J. Mater. Chem. A.* 2 (2014) 18139–18146.
- [133] Q. Wu, W. Li, D. Wang, S. Liu. Preparation and characterization of N-doped visible-light-responsive mesoporous TiO<sub>2</sub> hollow spheres. *Appl. Surf. Sci.* 299 (2014) 35–40.
- [134] J. Y. Hong, S. Huh. Hollow S-doped carbon spheres from spherical CT/PEDOT composite particles and their CO<sub>2</sub> sorption properties. *J. Colloid Interface Sci.* 436 (2014) 77–82.
- [135] J. Wang, H. C. Zeng. Hybrid OER Electrocatalyst Combining Mesoporous Hollow Spheres of N, P-Doped Carbon with Ultrafine Co<sub>2</sub>NiO<sub>x</sub>. *ACS Appl. Mater. Interfaces.* 12 (2020) 50324–50332.
- [136] Y. Deng, Y. Xie, K. Zou, X. Ji. Review on recent advances in nitrogen-doped carbons: preparations and applications in supercapacitors. *J. Mater. Chem. A.* 4 (2016) 1144–1173.
- [137] L. Hadidi, E. Davari, M. Iqbal, T. K. Purkait, D. G. Ivey, J. G. C. Veinot. Spherical nitrogen-doped hollow mesoporous carbon as an efficient bifunctional electrocatalyst for Zn-air batteries. *Nanoscale* 7 (2015) 20547–20556.
- [138] J. Tang, J. Liu, C. Li, Y. Li, M. Tade, S. Dai, Y. Yamauchi. Synthesis of nitrogen-doped mesoporous carbon spheres with extra-large pores through assembly of diblock copolymer micelles. *Angew. Chem. Int. Ed.* 54 (2015) 58–93.
- [139] W. Zhou, C. Wang, Q. Zhang, H. Abruña, Y. He, J. Wang, S. Mao, X. Xiao. Tailoring Pore Size of Nitrogen-Doped Hollow Carbon Nanospheres for Confining Sulfur in Lithium-Sulfur Batteries. *Adv. Energy Mater.* 5 (2015) 1401752.



- [140] J. Tang, J. Liu, R. R. Salunkhe, T. Wang, Y. Yamauchi. Nitrogen-doped hollow carbon spheres with large mesoporous shells engineered from diblock copolymer micelles. *Chem. Commun.* 52 (2015) 505–508.
- [141] J. Yu, M. Guo, F. Muhammad, A. Wang, F. Zhang, Q. Li, G. Zhu. One-pot synthesis of highly ordered nitrogen-containing mesoporous carbon with resorcinol-urea-formaldehyde resin for CO<sub>2</sub> capture. *Carbon.* 69 (2014) 502–514.
- [142] D. Ni, W. Sun, Z. Wang, Y. Bai, H. Lei, X. Lai, K. Sun. Heteroatom-Doped Mesoporous Hollow Carbon Spheres for Fast Sodium Storage with an Ultralong Cycle Life. *Adv. Energy Mater.* 9 (2019) 1900036.
- [143] L. Miao, D. Zhu, M. Liu, H. Duan, Z. Wang, Y. Lv, W. Xiong, Q. Zhu, L. Li, X. Chai, L. Gan. Cooking carbon with protic salt: Nitrogen and sulfur self-doped porous carbon nanosheets for supercapacitors. *Chem. Engin. J.* 347 (2018) 233–242.
- [144] X. Ma, G. Ning, Y. Kan, Y. Ma, C. Qi, B. Chen, Y. Li, X. Lan, J. Gao. Synthesis of S-doped mesoporous carbon fibres with ultrahigh S concentration and their application as high-performance electrodes in supercapacitors. *Electrochim. Acta.* 150 (2014) 108–113.
- [145] A. L. Cazetta, A. C. Martins, O. Pezoti, K. Bedin, K. Beltrame, T. Asefa, V. Almeida. Synthesis and application of N–S-doped mesoporous carbon obtained from nanocasting method using bone char as heteroatom precursor and template. *Chem. Engin. J.* 300 (2016) 54–63.
- [146] H. Zhang, Z. Jia, A. Feng, Z. Zhou, C. Zhang, K. Wang, N. Liu, G. Wu. Enhanced microwave absorption performance of sulfur-doped hollow carbon microspheres with mesoporous shell as a broadband absorber. *Compos. Commun.* 19 (2020) 42–50.
- [147] W. Kiciński, M. Norek, B. J. Jankiewicz. Heterogeneous carbon gels: N-doped carbon xerogels from resorcinol and n-containing heterocyclic aldehydes. *Langmuir.* 30 (2014) 14276–14285.
- [148] W. Kiciński, M. Norek, A. Dziura, M. Polański. Copolycondensation of heterocyclic aldehydes: A general approach to sulfur and nitrogen dually-doped carbon gels. *Micro. Meso. Mater.* 225 (2016) 198–209.
- [149] S. J. Taylor, M. D. Haw, J. Sefcik, and A. J. Fletcher. Gelation mechanism of resorcinol-formaldehyde gels investigated by dynamic light scattering. *Langmuir.* 30 (2014) 10231–10240.
- [150] K. Z. Gaca, J. Sefcik. Mechanism and kinetics of nanostructure evolution during early stages of resorcinol-formaldehyde polymerisation. *J. Colloid Interface Sci.* 406 (2013) 51–59.
- [151] F. Barroso-Bujans, C. Silvina, P. Palomino, E. Enciso, R. Svemir, F. Fernández-Alonso, A. Alegría, J. Colmenero de León. Dynamics and Structure of Poly(ethylene oxide) Intercalated in the Nanopores of Resorcinol-Formaldehyde Resin Nanoparticles. *Macromolecules.* 49 (2016) 5704–5713.
- [152] C. Lin, J. A. Ritter. Effect of synthesis pH on the structure of carbon xerogels. *Carbon.* 35 (1997) 1271–1278.
- [153] F. Ronsse, R. W. Nachenius, W. Prins. Carbonization of Biomass. *Recent Advances in Thermochemical Conversion of Biomass.* Elsevier (2015) 293–324.
- [154] Y. Seo, K. Kim, Y. Jung, R. Ryoo. Synthesis of mesoporous carbons using silica templates impregnated with mineral acids. *Micro. Meso. Mater.* 207 (2015) 156–162.
- [155] M. J. Eslamibidgoli, J. Huang, T. Kadyk, A. Malek, M. Eikerling. How theory and simulation can drive fuel cell electrocatalysis. *Nano Energy.* 29 (2016) 334–361.
- [156] L. Yu, X. Pan, X. Cao, P. Hu, X. Bao. Oxygen reduction reaction mechanism on nitrogen-doped graphene: A density functional theory study. *J. Catal.* 282 (2011) 183–190.
- [157] E. A. Carter. Challenges in modeling materials properties without experimental input. *Science.* 321, (2008) 800–803.
- [158] G. R. Schleder, A. C. M. Padilha, C. M. Acosta, M. Costa, A. Fazzio. From DFT to machine learning: Recent approaches to materials science-A review. *J. Phys. Mater.* 2 (2019) 032001.
- [159] N. Rey-Raap, S. F. Villanueva, J. A. Menéndez, A. Arenillas. Microporous carbon spheres derived from resorcinol-formaldehyde solutions. A new approach to coat supports. *Micro. Meso. Mater.* 252 (2017) 154–160.

- [160] M. Mirzaeian, Q. Abbas, D. Gibson, M. Mazur. Effect of nitrogen doping on the electrochemical performance of resorcinol-formaldehyde based carbon aerogels as electrode material for supercapacitor applications. *Energy*. 173 (2019) 809–819.
- [161] E. A. Oyedoh, A. B. Albadarin, G. M. Walker, M. Mirzaeian, M. N. M. Ahma. Preparation of controlled porosity resorcinol formaldehyde xerogels for adsorption applications. *Chem. Eng. Trans.* 32 (2013) 1651–1656.
- [162] F. Li, L. Xie, G. Sun, Q. Kong, F. Su, Y. Cao, J. Wei, A. Ahmad, X. Guo, C. Chen. Resorcinol-formaldehyde based carbon aerogel: Preparation, structure, and applications in energy storage devices. *Micro. Meso. Mater.* 279 (2019) 293–315.
- [163] L. Q. Chen, L. Chen, S. Kalinin, G. Klimeck, S. K. Kumar, J. Neugebauer, I. Terasaki. Design and discovery of materials guided by theory and computation. *NPJ Compu. Mater.* 1 (2015) 15007.
- [164] R. W. Pekala. Organic aerogels from the polycondensation of resorcinol with formaldehyde. *J. Mater. Sci.* 24 (1989) 3221–3227.
- [165] S. A. Al-Muhtaseb J. A. Ritter. Preparation and Properties of Resorcinol-Formaldehyde Organic and Carbon Gels. *Adv. Mater.* 15 (2003) 101–114.
- [166] J. Laskowski, B. Milow, L. Ratke. Subcritically dried resorcinol-formaldehyde aerogels from a base-acid catalyzed synthesis route. *Micro. Meso. Mater.* 197 (2014) 308–315.
- [167] L. M. Pratt, R. Szostak, I. M. Khan, J. Bibler. Alkaline degradation of resorcinol-formaldehyde resins: Solid-state NMR, thermal adsorption and desorption analysis, and molecular modeling. *J. Macromol. Sci.-Pure Appl. Chem.* 34 (1997) 281–289.
- [168] T. Li, M. Cao, J. Liang, X. Xie, G. Du. Mechanism of Base-Catalyzed Resorcinol-Formaldehyde and Phenol-Resorcinol-Formaldehyde Condensation Reactions: A Theoretical Study. *Polymers*. 9 (2017) 426.
- [169] S. S. Choi. Influence of Polycondensation Type on Structure of Resorcinol Formaldehyde Resin Studied by Molecular Simulation. *Polym. Korea*. 8 (2000) 125–130.
- [170] E. Martin, M. Prostedny, A. Fletcher, P. Mulheran. Modelling organic gel growth in three dimensions: Textural and fractal properties of resorcinol–formaldehyde gels. *Gels*. 6 (2020) 1–16.

## CHAPTER II.

### Hypothesis

---

The substitutional doping with N, S or N-S heteroatoms of the carbon lattice of OMCHS along with the intrinsic properties of the hollow sphere will provide a catalytic surface with adequate features, resulting in metal-free electrocatalysts for the ORR in alkaline media.

### Objectives

---

#### General objective

To experimentally evaluate the effect of doping OMCHS with N, S, and N/S heteroatoms on their catalytic activity for the ORR and develop a theoretical surface of the OMCHS.

#### Specific Objectives

- ❖ To analyze the effect of implementing 2-pyridinecarboxaldehyde, pyrrole, and 2-thiophenemethanol as nitrogen and sulphur sources, respectively, aiming to evaluate the capacity to modify the structure, textural, and morphology properties of the OMCHS.
- ❖ To study the structural and electronic variation in N-doped, S-doped, and N/S co-doped on the catalytic activity and electrochemical stability of OMCHS for the ORR.
- ❖ To identify the species responsible for the electrochemical stability of N-doped, S-doped, and N/S co-doped OMCHS through chemical superficial composition analysis.
- ❖ To develop a theoretical R-F model, aiming to describe the surface of the OMCHS.

## CHAPTER III.

### Materials and methods

---

3.1 Reagents and gases From Sigma-Aldrich: ethanol anhydrous ( $\leq 0.005\%$  water), tetraethyl orthosilicate (TEOS, 98%), cetyltrimethylammonium chloride (CTAC, 25%), resorcinol (99%), formaldehyde solution (37%), 2-pyridinecarboxaldehyde (99%), pyrrole (98%), 2-thiophenemethanol (98%), methanol anhydrous (99.8%), potassium hydroxide (90%), 2-propanol anhydrous (99.5%), Nafion® 117 solution (5 wt. %). From J.T. Baker: ammonium hydroxide (28-30%), hydrofluoric acid (48-52%). From Infra: ultra high purity (UHP) nitrogen and oxygen (99.999%).

### 3.2 Synthesis of N-doped, S-doped, and N/S co-doped OMCHS

The heteroatoms-doped OMCHS were synthesized modifying the hard template method reported by Mezzavilla *et al.* [1].

Hard silica cores were obtained by the Stöber method as follows: a mixture of 60 mL of ethanol, 11.4 mL of deionized water, 1.3 mL of ammonium hydroxide, and 2.4 mL of TEOS was stirred for 7 h. Afterward, 183 mL of deionized water and 37.2 mL of ethanol were added to the mixture and stirred for 10 min. Then, 6.2 mL of CTAC were slowly added to the solution, keeping the stirring for 15 min.

For the synthesis of the shells of the hollow spheres, the solution containing the hard silica cores was mixed with resorcinol and formaldehyde as carbon precursors, along with 2-pyridinecarboxaldehyde, pyrrole, and 2-thiophenemethanol (separately) as doping agents to promote the formation of N-pyridinic, N-pyrrolic, and thiophene species, respectively. The electrocatalysts were labeled as N1-OMCHS, N2-OMCHS, and S-OMCHS, respectively.

The synthesis of co-doped OMCHS was carried out by separately mixing solution containing the hard silica cores with 2-pyridinecarboxaldehyde or pyrrole with 2-thiophenemethanol, to obtain N-pyridinic/thiophene (labeled N1-S-OMCHS) and N-pyrrole/thiophene (labeled N2-S-OMCHS) species. The molar concentration of each precursor is summarized in Table 3.1.

Subsequently, 2.5 mL of TEOS were added. The resulting solutions were stirred for 12 h, placed in sealed steel autoclaves covered with Teflon, and heated at 100 °C for 24 h.

**Table 3.1.** Molar concentration of reagents used for the synthesis of the electrocatalysts.

Reagent		Electrocatalysts				
		N1-OMCHS	N2-OMCHS	S-OMCHS	N1-S-OMCHS	N2-S-OMCHS
Resorcinol		0.0036	0.0055	0.0064	0.0055	0.0055
Formaldehyde		0.0067	0.0076	0.0086	0.0078	0.0074
2-Pyridinecarboxaldehyde	(Mol)	0.0074	-- <sup>a</sup>	-- <sup>a</sup>	0.0036	-- <sup>a</sup>
Pyrrole		-- <sup>a</sup>	0.0046	-- <sup>a</sup>	-- <sup>a</sup>	0.0034
2-Thiophenemethanol		-- <sup>a</sup>	-- <sup>a</sup>	0.0034	0.0017	0.0019

--<sup>a</sup>: not added

After solvothermal treatment, the powders were recovered by filtration, washed with an ethanol/water solution, and dried at 60 °C. Then, the powders were carbonized at 1000 °C under N<sub>2</sub> atmosphere in a tubular furnace for 4 h with a heating rate of 5 °C min<sup>-1</sup>.

The silica hard cores were leached from the black powders obtained after carbonization with an aqueous solution of 10% of hydrofluoric acid for 48 h, then the products were washed with deionized water and dried at 60 °C. For comparison purposes, non-doped OMCHS were synthesized by the same methodology, without adding any source of heteroatoms.

The OMCHS, N1-OMCHS, N2-OMCHS, S-OMCHS, N1-S-OMCHS, and N2-S-OMCHS electrocatalysts were functionalized with methanol by the intermittent microwave heating method as follows: 1 g of each electrocatalyst was dispersed separately in 100 mL of 0.5 M methanol solution in an ultrasonic bath for 30 min and magnetically stirred for 1 h. Then, the solution was placed in a home-modified microwave oven and heated under refluxing conditions with 25 s on/15 s off pulses for 8 min. Finally, the powders were filtered, washed with deionized water, dried at 60 °C, and calcined at 200 °C for 30 min in air atmosphere.

### 3.1. Physicochemical characterization

The structural features of the electrocatalysts were examined by Raman spectroscopy in a Raman Thermo Scientific DXR2 model (wavelength = 633 nm, in the 100 to 3500 cm<sup>-1</sup> range). Also, by X-ray diffraction (XRD) in a Bruker D2 Phaser 2nd Gen. apparatus in a 10-100° (2θ) range with a step scan of 0.01° per 0.4 s.

The textural features were analyzed by N<sub>2</sub> adsorption/desorption technique in a Quantachrome Nova- Win at 77 K. The specific surface area was calculated by the non-local-density functional theory (NLDFT) method. The pore size distribution curves were determined from the desorption of the isotherms using the Barrett-Joyner-Halenda (BJH) model.

The morphology of the metal-free electrocatalysts was characterized by Field-Emission Scanning Electron Microscopy (FESEM), in a Jeol JSM-7800F Prime microscope, using a Bruker Quantax detector, and by Transmission Electron Microscopy (HR-TEM), in a Hitachi HT7700 equipment with an acceleration voltage of 100 kV.

### 3.2. Electrochemical measurements

The electrochemical characterization was performed with a Bio-Logic VSP-300 bipotentiostat coupled to a Rotating Ring Disk Electrode (RRDE) set-up, in a three-electrode cell configuration. The reference electrode was an Ag/AgCl (saturated in KCl solution) placed in a Luggin capillary with a membrane at the tip, while the counter electrode was a Pt coil in a separate compartment also with a membrane at the tip. All measurements were performed in 0.5 mol L<sup>-1</sup> KOH solution. In this work, all potentials have been referred to the Reversible Hydrogen Electrode (RHE).

For the preparation of the working electrodes, catalyst inks with the following composition were dispersed by ultrasound for 30 min, separately: 10 mg of the corresponding electrocatalyst, 1 mL of 2-propanol, and 60 μL of Nafion<sup>®</sup> solution. An aliquot of 10 μL was deposited on a glassy carbon electrode (5.61 mm diam) embedded in a PEEK structure with a gold ring (Pine Inst.). The nominal catalyst loading at the electrodes was 381 mg cm<sup>-2</sup>.

Cyclic voltammograms (CVs) were obtained in N<sub>2</sub>-saturated electrolyte in a potential range of 1.2 to 0.05 V/RHE at a scan rate of 20 mV s<sup>-1</sup>. The catalytic activity for the ORR was evaluated in the same potential interval. First, a CV in N<sub>2</sub>-saturated electrolyte at a scan rate of 5 mV s<sup>-1</sup> and rotating rate of 2000 rpm was recorded to assess the background current. Then, CVs were acquired in O<sub>2</sub>-saturated electrolyte at the scan rate of 5 mV s<sup>-1</sup> at several rotation rates ( $\omega$ = 400, 800, 1200, 1600, and 2000 rpm). Subsequently, the background current was subtracted from the

CVs in O<sub>2</sub> atmosphere. In this work, only the negative scans of the CVs were shown. The current density (*j*) was normalized concerning the geometric area of the glassy carbon.

At the same time, the current in the Au ring, which correlates to the hydrogen peroxide produced from the ORR, was collected by fixing it a constant potential of 1.2 V/RHE. The percentage of hydrogen peroxide produced (%HO<sub>2</sub><sup>-</sup>) and the number of electrons transferred (*n*) were determined with the following equations [2]:

$$\%HO_2^- = \frac{\frac{200 * I_R}{N}}{I_D + (I_R/N)} \quad (1)$$

$$n = \frac{4 * I_D}{I_D + (I_R/N)} \quad (2)$$

where *I<sub>D</sub>* is the disk current, *I<sub>R</sub>* is the ring current and *N* is the collection efficiency (0.37 in alkaline media, provided by the manufacturer). For comparison purposes, a commercial 20 wt. % Pt/C (E-tek), considered as benchmark for the ORR by the US Department of Energy was also characterized.

The mass catalytic activity of Pt/C and metal-free electrocatalysts were obtained according to the procedure reported by Jaouen *et al.* [3], using the equations (3), (4), and (5).

$$i_k = \frac{i \times i_d}{i - i_d} \quad (3)$$

$$I_M = \frac{i_k}{m_{catalyst}} \quad (4)$$

$$I_M(\text{Pt/C}) = \frac{i_k}{m_{carbon}} \quad (5)$$

where *i* is the experimental current collected at the working electrode, *i<sub>d</sub>* is the diffusion-limiting current at 0.2 V vs RHE, *i<sub>k</sub>* is the kinetic current, *I<sub>M</sub>* is the mass current density, and *m<sub>catalyst</sub>* is the amount of carbon in the electrocatalyst loading on the glassy carbon. Likewise, the mass activity of the Pt/C electrocatalyst is defined by eq. (5), where *m<sub>carbon</sub>* is the mass content deposited in the glassy carbon of the electrode considering the wt. % of C indicated by the

manufacturer. Obtaining Pt/C mass activity allows a better comparison of performance with the metal-free electrocatalysts.

Accelerated degradation tests (ADT) were carried out according to the recommendations of the US Department of Energy (DOE) [4] as follows: 3000 cycles were performed in the potential range between 0.6 and 1.0 V/RHE at a scan rate of 50 mV s<sup>-1</sup> in N<sub>2</sub>-atmosphere. Then, a CV was recorded to determine the background current between 1.2 and 0.05 V/ RHE at 5 mV s<sup>-1</sup> in the N<sub>2</sub>-saturated electrolyte. Afterwards, a CV was obtained in O<sub>2</sub>-saturated electrolyte in the same potential interval, at 2000 rpm and a scan rate of 5 mV s<sup>-1</sup>, aiming to evaluate the catalytic activity after ADT and compare it to that before. In addition, %HO<sub>2</sub><sup>-</sup> and n after ADT were determined too.

### 3.3. Chemical surface composition of N-doped, S-doped, and N/S co-doped OMCHS before and after ADT.

The surface chemistry of OMCHS, N1-OMCHS, N2-OMCHS, S-OMCHS and N1-S-OMCHS and N2-S-OMCHS was determined by X-ray photoelectron spectroscopy (XPS), in a Thermo Scientific K-Alpha<sup>+</sup>XPS apparatus, equipped with a monochromator (Al-K $\alpha$  radiation,  $h\nu = 1486.68$  eV). Surface charging effects were compensated by referencing the binding energies to the C 1s spectrum of carbon at 284.8 eV. Before ADT, a catalyst ink containing 0.05 g of each electrocatalyst, 500 mL of ethanol, and 300 mL of Nafion<sup>®</sup> solution was dispersed by ultrasound for 1 h. The solvent was left to evaporate, and the obtained powders were evaluated.

For characterization after ADT, a Rotating Disk Electrode (Pine Inst.) was modified to obtain the minimum amount of electrocatalysts required for XPS analysis. For this purpose, the glassy carbon disk was removed from the rotating disk electrode, leaving a void in the Teflon U-cup within the PEEK shroud (Fig. 3.1). Several aliquots of catalyst ink with the same composition mentioned in the previous paragraph were added into the Teflon U-cup, allowing for the evaporation of the solvent at 50 °C. The addition of catalyst ink was repeated until the U-cup was filled with dry electrocatalyst powder. Afterwards, the electrocatalysts underwent ADT, as described above. Then, the powders were recovered and submitted to XPS characterization.



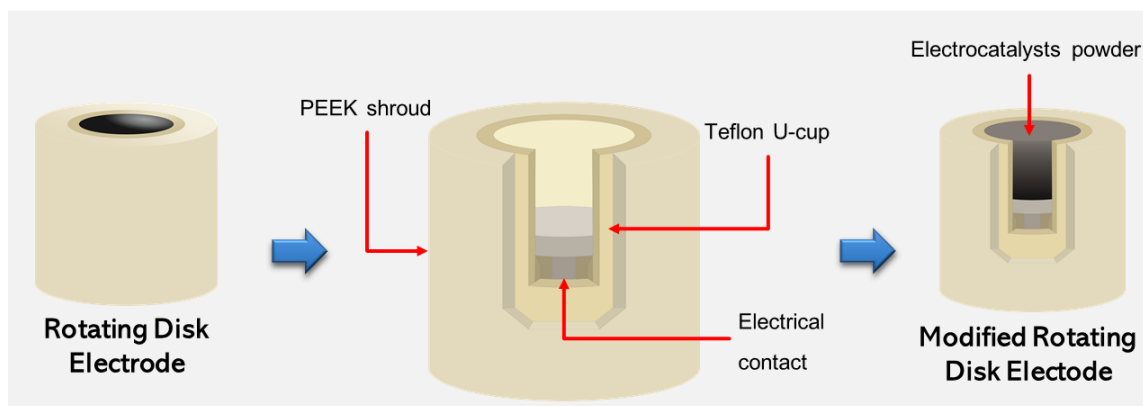


**Fig. 3.1.** Scheme of the Rotating Disk Electrode modified for the XPS characterization of the metal-free electrocatalysts after ADT.

### 3.4. Theoretical study of the resorcinol-formaldehyde (R-F) reaction

#### 3.4.1. Synthesis of R-F polymers

RF polymers were synthesized by solubilizing 0.62 g of resorcinol powder in 2 mL of water and heating it to 80 °C. Then, 0.84, 0.63, 0.42 and 0.21 mL of formaldehyde were added to obtain a mixture with a nominal molar ratio of 1:2, 1:1.5, 1:1, and 1:0.5, respectively. Afterwards, the mixtures were heated to 100 °C for 24 h, allowing them to cool down to room temperature. The polymers were labeled as RF2, RF1.5, RF1, and RF0.5, according to the respective formaldehyde concentration. Then, the polymers obtained were characterized by XRD technique using a Panalytical Empyrean spectrometer using the Cu K $\alpha$  ( $\lambda = 0.154$  nm) radiation in 5-65° ( $2\theta$ ) range with a step scan of 0.03° per second.

#### 3.4.2. Theoretical calculation

Density functional theory (DFT) calculations were performed using the Vienna *Ab initio* simulation package (VASP). Wave functions were described within the projector augmented wave method (PAW) and the generalized gradient approximation (GGA) was used in the Perdew-Burke-Ernzerhof (PBE) scheme to describe the exchange-correlation functional. Expansion of plane waves was performed with a 600 eV energy cut-off and a k-point sampling with a density of at least 4000-points/atom, considering a gamma-centered grid in the Brillouin zone which guarantees convergence criteria of ionic forces of  $1 \times 10^{-3}$  eV [5].

The bulk modulus was derived from a third-order Birch-Murnaghan equation of states (EOS) accounting for a 10% volume change of the unit cell [6]. Formation enthalpies  $\Delta H_f$  were calculated according to Eq. (6), where  $E_{\text{tot}}$  is the total energy,  $E_{\text{pha}}$  is the energy of the resorcinol phase, and  $E_{\text{form}}$  is the energy of the formaldehyde molecule.

$$\Delta H_f = E_{\text{tot}} - (E_{\text{pha}} + nE_{\text{form}}) \quad (6)$$

The crystalline phases of  $\alpha$ -resorcinol and  $\beta$ -resorcinol were used for the theoretical calculations [7]. The structure corresponds to a Pna<sub>21</sub> orthorhombic space group and contains four molecules in the unit cell. In the first stage,  $\alpha$ -resorcinol and the  $\beta$ -resorcinol unit cells were saturated with two, four, six, and eight hydroxymethyl molecules (labeled as 2HMR, 4HMR, 6HMR, and 8HMR, respectively) in ortho and para positions of resorcinol (2 and 4 places in the ring, respectively). In the second stage, methylene and methylene ether bridges were formed through the elimination of water molecules and labeled as 2MR, 4MR, 6MR, and 8MR. Full relaxation of all structural phases was performed. From these structures, the amorphized diffraction patterns were obtained with the software GDIS Molecule Modeller and compared with the XRD of the materials obtained in section 3.4.1.

## References

- [1] S. Mezzavilla, C. Baldizzone, K.J.J. Mayrhofer, F. Schüth. General Method for the Synthesis of Hollow Mesoporous Carbon Spheres with Tunable Textural Properties, *ACS Appl. Mater. Interfaces*. 7 (2015) 12914–12922.
- [2] G.A. Ferrero, A.B. Fuertes, M. Sevilla, M. Titirici. Efficient metal-free N-doped mesoporous carbon catalysts for ORR by a template-free approach. *Carbon*. 106 (2016) 179–187.
- [3] S.M. Alia, C. Ngo, S. Shulda, M.A. Ha, A.A. Dameron, J.N. Weker, K. Neyerlin, S. Kocha, S. Pylypenko, B. Pivovar. Exceptional Oxygen Reduction Reaction Activity and Durability of Platinum-Nickel Nanowires through Synthesis and Post-Treatment Optimization. *ACS Omega*. 2 (2017) 1408–14188.
- [4] F. Jaouen, J. Herranz, M. Lefèvre, J.-P. Dodelet, U.I. Kramm, I. Herrmann, P. Bogdanoff, J. Maruyama, T. Nagaoka, A. Garsuch, J.R. Dahn, T. Olson, S. Pylypenko, P. Atanassov, E.A. Ustinov. Cross-Laboratory Experimental Study of Non-Noble-Metal Electrocatalysts for the Oxygen Reduction Reaction. *ACS Appl. Mater. Interfaces* 1 (2009) 1623–1639.
- [5] M. Arango-Ramirez, A. Vargas-Calderon, A.M. Garay-Tapia. On the importance of hexagonal phases in TM (TM = Ti, Zr, and Hf) mono-nitrides. *J. Appl. Phys.* 128 (2020) 105106–105117.
- [6] F. Birch. Finite elastic strain of cubic crystals. *Phys. Rev.* 71 (1947) 809–824.
- [7] G.E. Bacon, E.J. Lisher. A neutron powder diffraction study of deuterated  $\alpha$ - and  $\beta$ -resorcinol. *Acta Cryst.* B36 (1980) 1908–1916.

## CHAPTER IV.

### Insight into the performance and stability of N-doped Ordered Mesoporous Carbon Hollow Spheres for the ORR: Influence of the nitrogen species on their catalytic activity after ADT

#### 4.1. Physicochemical characterization of N-doped OMCHS

Raman spectra of OMCHS, N1-OMCHS, and N2-OMCHS are shown in Figs. 4.1 a, b, and c) respectively. The spectra show the two main typical signals of carbon-based materials, i.e., the D-band ( $\approx 1325 \text{ cm}^{-1}$ ), which is representative of defects and structural disorder in the graphitic lattice, caused by the breakage of the six-fold symmetry; and the G-band ( $\approx 1595 \text{ cm}^{-1}$ ), which is due to the in-plane stretching of symmetric vibrations of the  $\text{sp}^2 \text{ C}=\text{C}$  bonds [1].

The intensity ratio between the D and G interbands ( $I_{\text{D}}/I_{\text{G}}$ ) has been determined after deconvoluting the data in the spectra by Lorentzian fitting. This ratio gives an approach to the density of defect sites in the carbon lattice [2]. The  $I_{\text{D}}/I_{\text{G}}$  value of OMCHS, N1-OMCHS, and N2-OMCHS is 1.51, 1.44, and 1.32, respectively.

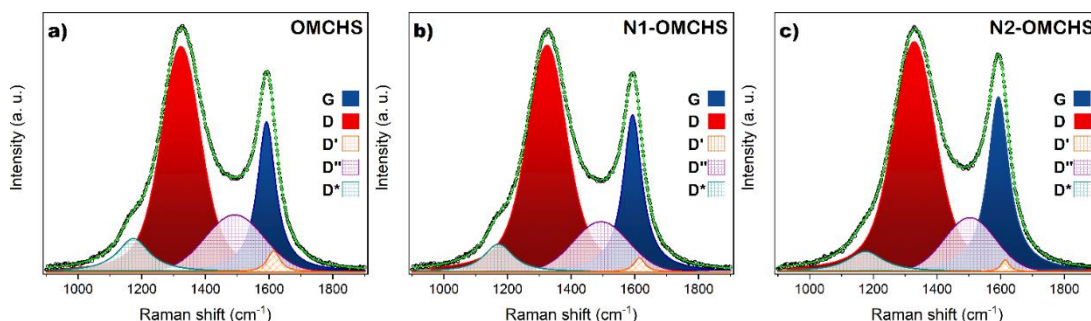


**Fig. 4.1.** Raman spectra of (a) OMCHS, (b) N1-OMCHS, and (c) N2-OMCHS. The G, D, D', and D\* bands were fitted with a Lorentzian function, whereas the D'' band was fitted with a Gaussian function.

As can be seen, the  $I_{\text{D}}/I_{\text{G}}$  slightly decreases when the carbon structures are doped with nitrogen species. This feature indicates that the 2-pyridinecarboxaldehyde and pyrrole nitrogen precursors promote the formation of a more ordered structure. At this point, it should be briefly mentioned that the nitrogen content, determined by XPS, is 0.99, 2.56, and 1.65. % for OMCHS, N1-OMCHS, and N2-OMCHS respectively, thereby confirming the presence of nitrogen; however, the XPS results are widely discussed below.

Moreover, the D' ( $\approx 1615\text{ cm}^{-1}$ ), D'' ( $\approx 1500\text{ cm}^{-1}$ ), and D\* ( $\approx 1170\text{ cm}^{-1}$ ) interbands have been developed from the deconvolution of all the spectra. The D' interband usually merges with the G band and is due to phonon confinement caused by the defects [3]. Meanwhile, the D'' interband has been assigned to interstitial defects of amorphous carbon fragments containing  $sp^2$  bonds [4–6]. In this regard, the relative intensity of D'' is 17.3, 14.5, and 13.5 for OMCHS, N1-OMCHS, and N2-OMCHS, respectively. As can be seen, the relative intensity of the D'' interband decreases at N1-OMCHS and N2-OMCHS, compared to OMCHS.

Now, considering that the  $I_D/I_G$  ratio slightly decreases with the incorporation of both nitrogen precursors, this behavior indicates that 2-pyridinecarboxaldehyde and pyrrole promote the formation of carbon fragments bonded with  $sp^2$  nanodomains. This outcome is in good agreement with the observations reported by Vollebregt *et al.* [7], who suggest that the intensity of the D'' interband decreases as the crystallinity of the sample increases.

Meanwhile, the D\* interband can be attributed to stretching vibrations of the  $sp^2$ - $sp^3$  (C-C and C=C) bonds of polyene-like structures [8–10]. Furthermore, the  $I_{D^*}/I_G$  ratio intensity has been calculated and is 0.23, 0.18, and 0.11 for OMCHS, N1-OMCHS, and N2-OMCHS, respectively, confirming that the crystallinity increases when doping the hollow spheres with the N-precursors [11]. Also, it should be noted that pyrrole promotes the formation of relatively more crystalline carbons than 2-pyridinecarboxaldehyde.

The XRD patterns of OMCHS, N1-OMCHS, and N2-OMCHS are shown in Fig. 4.2 a). All patterns show two well-defined peaks, the most intense at  $2\theta = 22\text{--}25^\circ$ , which are assigned to the (002) graphite interlayer. The second peak at  $2\theta = 43\text{--}45^\circ$  corresponds to (101) graphite plane [12, 13]. It is observed that for both N-doped electrocatalysts, the (002) plane shifts to higher angles by ca.  $2^\circ$  ( $2\theta$ ), related to the OMCHS electrocatalysts. This shift indicates a reduction of the interlayer distance for the N-doped electrocatalysts compared to OMCHS, which is in good agreement with previous reports [14].

Fig. 4.2b) depicts the  $N_2$  adsorption/desorption isotherms of the metal-free electrocatalysts, which show a hysteresis loop characteristic of type IV(a) isotherms. According to the most recent technical report by the International Union of Pure and Applied Chemistry (IUPAC) [15],

type IV(a) isotherms are characteristic of mesoporous materials. Moreover, it can be observed that the three isotherms show a combination of H2 and H3-type hysteresis.

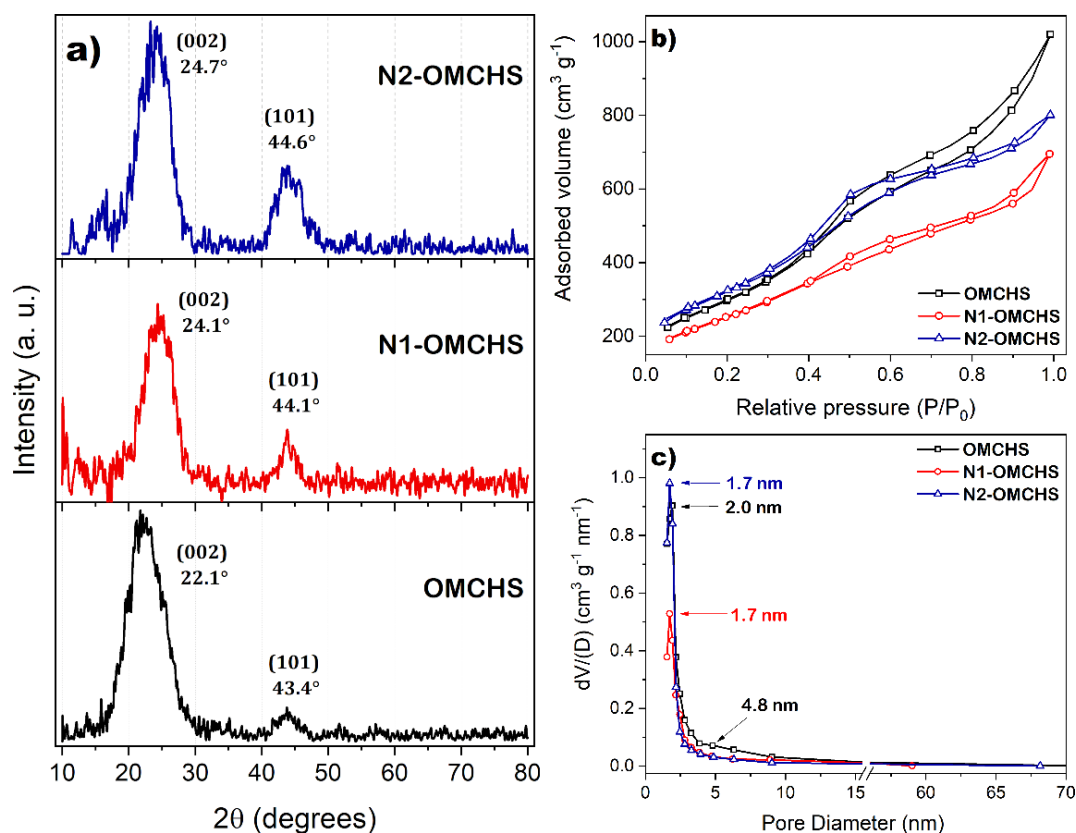


**Fig. 4.1.** (a) XRD patterns, (b) N<sub>2</sub> adsorption-desorption isotherms, and (c) BJH desorption pore size distribution of OMCHS, N1-OMCHS, and N2-OMCHS.

The hysteresis can be divided in two capillary condensation steps, i.e., in the  $P/P_0 = 0.40$  to  $0.79$  (H2-type) and the  $P/P_0 = 0.80$  to  $0.90$  (H3-type) intervals. The former is associated with the filling of mesoporous by adsorbed N<sub>2</sub>, while the latter can be attributed to the continuous adsorption of N<sub>2</sub> onto the hollow core [16–19].

**Table 4.1.** Textural and morphological features of the N-doped OMCHS.

Sample	SSA <sub>DFT</sub> (m <sup>2</sup> g <sup>-1</sup> )	Average Pore size (nm)	Pore volume (cm <sup>3</sup> g <sup>-1</sup> )	Average diameter (avg., nm)	Wall thickness (avg., nm)
OMCHS	810	2.0	1.37	301 ± 1.9	52
N1-OMCHS	662	1.7	0.94	255 ± 1.4	43
N2-OMCHS	873	1.7	1.11	231 ± 1.8	27

As can be observed, for the N-doped electrocatalysts, the shape of the isotherms changes slightly related to that of OMCHS, an indication that when nitrogen species are incorporated into the carbon lattice, both textural and structural properties are modified. The textural properties of the metal-free electrocatalysts are summarized in Table 4.1.

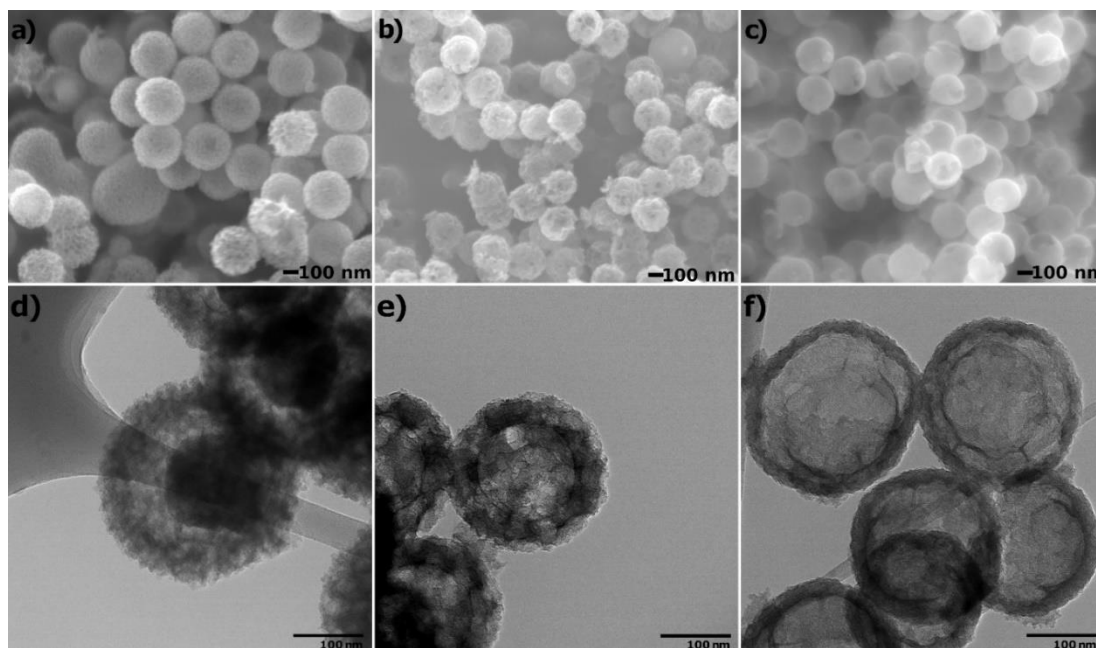


**Fig. 4.3.** FE-SEM and TEM images of (a, d) OMCHS; (b, e) N1-OMCHS; and (c, f) N2-OMCHS.

The specific surface area ( $SSA_{DFT}$ ) is 810, 662, and 873  $m^2 g^{-1}$  at OMCHS, N1-OMCHS, and N2-OMCHS. The average pore size distribution curves show the existence of mesopores centered at 2.0 nm in OMCHS. Additionally, slightly enlarged pores at 4.8 nm are also found at this electrocatalyst, which is likely positioned in the shell of the carbon spheres. Meanwhile, N1-OMCHS and N2-OMCHS have an average pore size distribution centered at 1.7 nm. The pore volume is 1.37, 0.94, and 1.11  $cm^3 g^{-1}$  for OMCHS, N1-OMCHS, and N2-OMCHS, respectively (Table 4.1). Thus, there is a noticeable effect of the nitrogen precursor on the  $SSA_{DFT}$  values of electrocatalysts.

FE-SEM images of OMCHS, N1-OMCHS, and N2-OMCHS are shown in Figs. 4.3 a-c). Their morphology is that of well-defined nanospheres having a rough surface. It is observed that the diameter of the nanospheres becomes smaller after doping (Table 4.1), with a more important effect at N2-OMCHS (231 nm). Even more, the surface of N2-OMCHS seems less rough compared to OMCHS and N1-OMCHS.

Figs. 4.3 d-f) show the TEM images of OMCHS, N1-OMCHS, and N2-OMCHS, at which the effect of the nitrogen precursor on their morphology can be seen more clearly. For example, the average diameter of the spheres at OMCHS is  $301 \pm 1.9$  nm (its sphere diameter distribution is shown in Fig. 4.4a), while its wall thickness is ca. 52 nm.

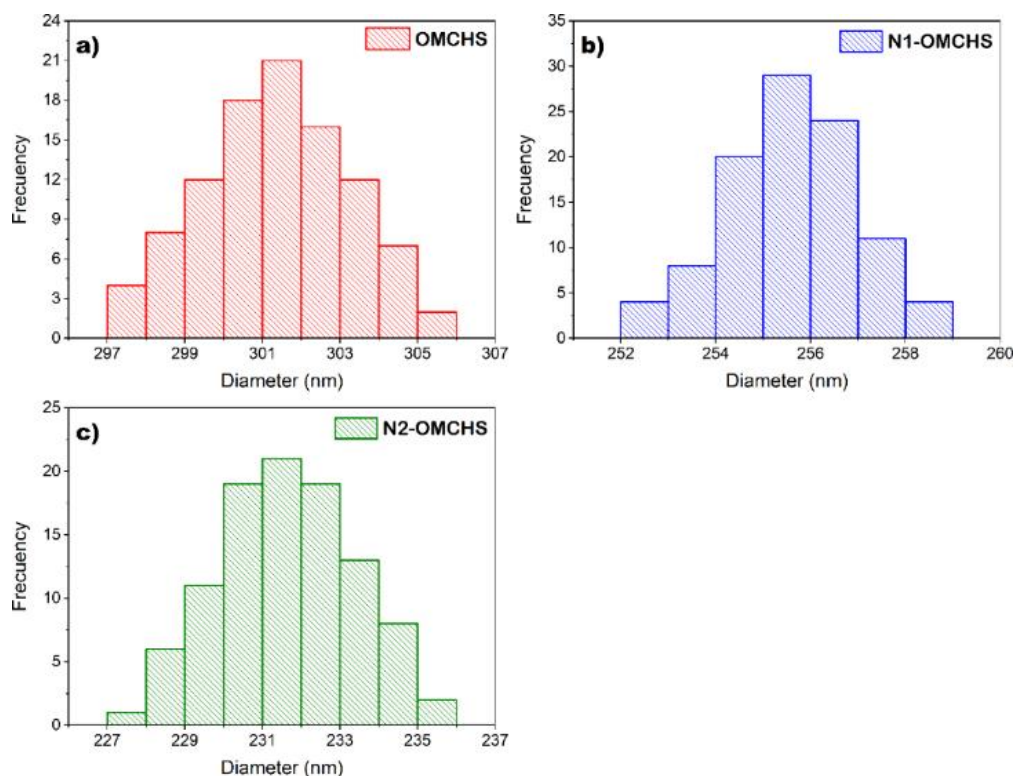


**Fig. 4.4.** Spheres diameter distribution of (a) OMCHS, (b) N1-OMCHS, and (c) N2-OMCHS.

The spheres are rough in nature. The darker circular zones in Fig. 4.3d) are attributed to residual silicon not being removed during leaching. N1-OMCHS (Fig. 4.3e) shows an average diameter of  $255 \pm 1.4$  nm with a wall thickness of 43 nm (Table 4.1 and Fig. 4.4b) and hollow nanospheres without residual silicon. Moreover, there is a clear effect of the doping since the morphology of the spheres differs from that of OMCHS, with a rougher surface that resulted in a lower  $SSA_{DFT}$  value and a slightly smaller average pore size (Table 4.1).

The micrograph of N2-OMCHS in Fig. 4.3 f) also shows differences in morphology due to the doping compared to the other electrocatalysts. Its average diameter is  $231 \pm 1.8$  nm (the smallest among the electrocatalysts, Fig. 4.4c), with a wall thickness of 27 nm, significantly thinner compared to OMCHS and N1-OMCHS. Moreover, it should be noted that the surface of the

spheres of N2-OMCHS is the smoothest, although its  $SSA_{DFT}$  value is the highest (Table 4.1), with an average pore size of 1.7 nm.

Therefore, this analysis demonstrates the significant effect of doping on the textural and morphological features of the electrocatalysts, and more importantly, that the surface modification strongly depends on the nitrogen precursor.

#### 4.2. The catalytic activity of the N-doped OMCHS for the ORR

Fig. 4.5 a) shows the CVs of OMCHS, N1-OMCHS, and N2-OMCHS, with a semi-rectangular shape that suggests an effect of electric double-layer capacitance by non-faradaic processes [16]. In some cases, there is a relationship between the shape of the CV and the textural properties of the electrocatalysts, since larger pores and higher  $SSA_{DFT}$  generally improve the electrolyte diffusion and the ion transport, increasing  $j$  [20].

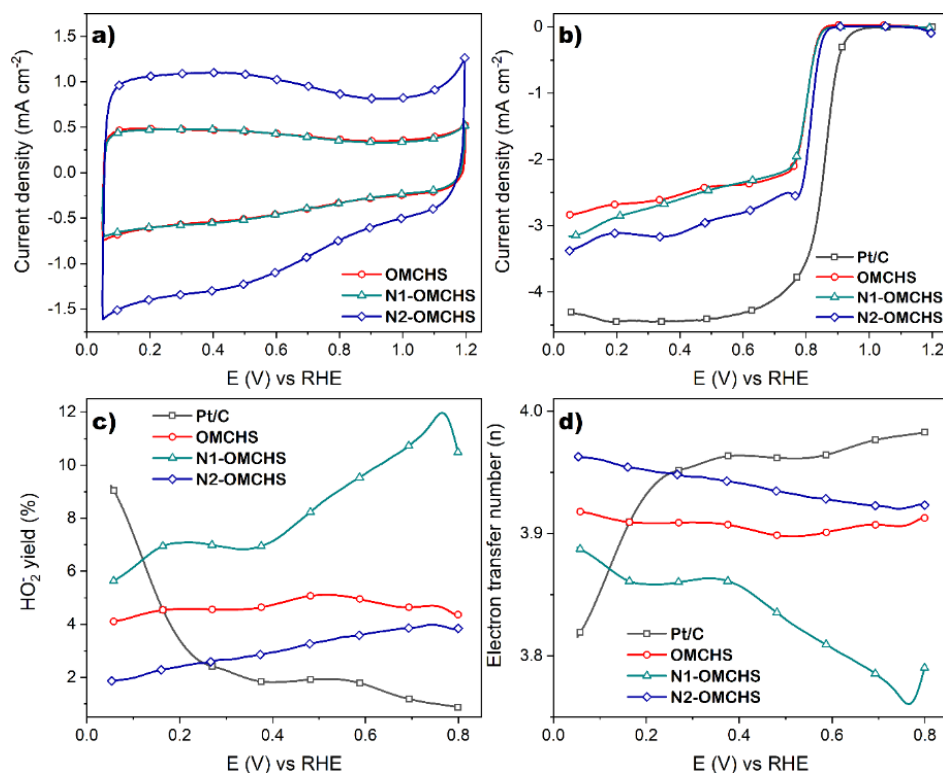


**Fig. 4.5.** (a) CVs of OMCHS, N1-OMCHS, and N2-OMCHS were collected at  $20 \text{ mV s}^{-1}$ . Electrolyte:  $\text{N}_2$ -saturated  $0.5 \text{ mol L}^{-1}$  KOH. (b) Negative scan only of the CVs of the ORR at 2000 rpm of OMCHS, N1-OMCHS, N2-OMCHS, and Pt/C. Electrolyte:  $\text{O}_2$ -saturated  $0.5 \text{ mol L}^{-1}$  KOH. (c)  $\% \text{HO}_2^-$ , and (d)  $n$  plots at the electrocatalysts.



Nevertheless, even though OMCHS and N2-OMCHS have similar  $SSA_{DFT}$  values, the CV of the latter has the largest area within the curve. Such enhancement suggests that pyrrole promotes the formation of extrinsic defects and active sites, which in addition modify the surface wettability of N2-OMCHS providing pseudocapacitive properties and thus higher  $j$  values over the potential scanned [21].

A similar analysis comparing OMCHS and N1-OMCHS can be done. The values in Table 4.1 show that the  $SSA_{DFT}$  of the former is at least 22% higher than that of the latter. Despite this, their CVs (i.e., the areas within the curves) are very similar. It is hypothesized that 2-pyridinecarboxaldehyde promotes the formation of defects and active sites, modifying the surface chemistry of N1-OMCHS. By doing so, the electrode-electrolyte interface of the electrocatalyst is improved, increasing its electrochemical double layer although N1-OMCHS has a lower  $SSA_{DFT}$  than OMCHS.

In addition, it is noticeable that the defects and active sites from the doping with pyrrole are not promoted by 2-pyridinecarboxaldehyde, and therefore the electrochemical properties differ between N2-OMCHS and N1-OMCHS.

Polarization curves of the ORR (i.e., the negative scan only of the CVs after background current correction) at 2000 rpm of the metal-free and Pt/C electrocatalysts are shown in Fig 4.5b). The kinetic, mixed, and diffusion-controlled characteristic regions of the ORR can be discerned at the metal-free electrocatalysts. The onset potential ( $E_{onset}$ ) before ADT (1<sup>st</sup> cycle) of N2-OMCHS (0.88 V/RHE) is more positive than those of N1-OMCHS and OMCHS, confirming the advantageous effect of the nitrogen incorporation (Table 4.2).

The  $E_{onset}$  value of N2-OMCHS is comparable with some recent works on N-doped mesoporous carbon materials. Several groups have reported the  $E_{onset}$  values of hollow spheres (1.0 V/RHE, [22]), carbon nanoflowers (0.90 V/RHE, [23]), mesoporous carbon (0.90 V/RHE, [24]) and mesoporous carbon spheres (0.90 V/RHE, [25]). Nevertheless,  $E_{onset}$  at N2-OMCHS is still 130 mV more negative than that of Pt/C (Table 4.2.).

The polarization curves of the ORR at Pt/C, OMCHS, N1-OMCHS, and N2-OMCHS at different rotation rates are shown in Fig. 4.6. As expected, the current density increases with

increasing  $\omega$  because oxygen molecules diffuse at a higher rate towards the surface of the electrocatalysts. Fig. 4.7 shows plots of IR at the electrocatalysts also at several values of  $\omega$ .

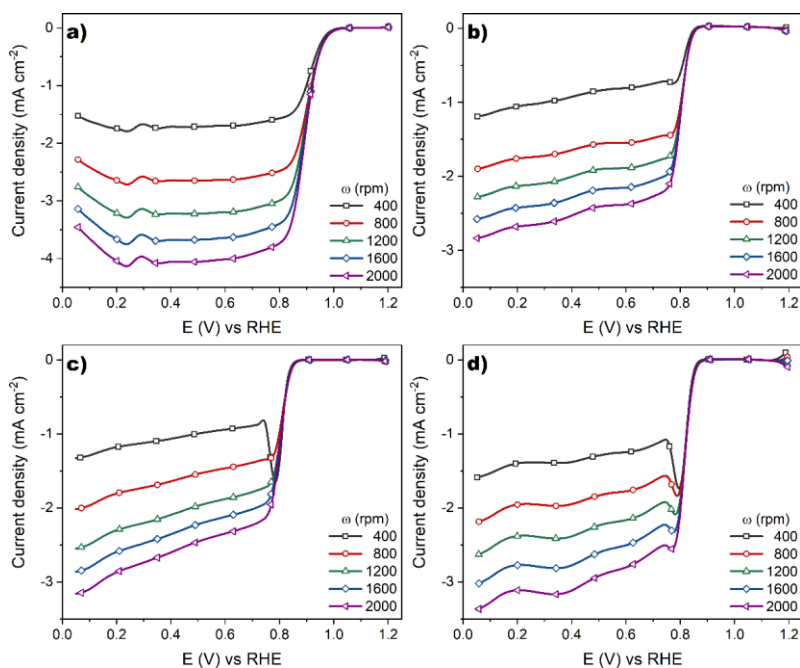


**Fig. 4.6.** Polarization curves of the ORR of (a) Pt/C, (b) OMCHS, (c) N1-OMCHS, and (d) N2-OMCHS. Electrochemical test performed in O<sub>2</sub>-saturated 0.5 mol L<sup>-1</sup> KOH, at a scan rate of 5 mV s<sup>-1</sup>.

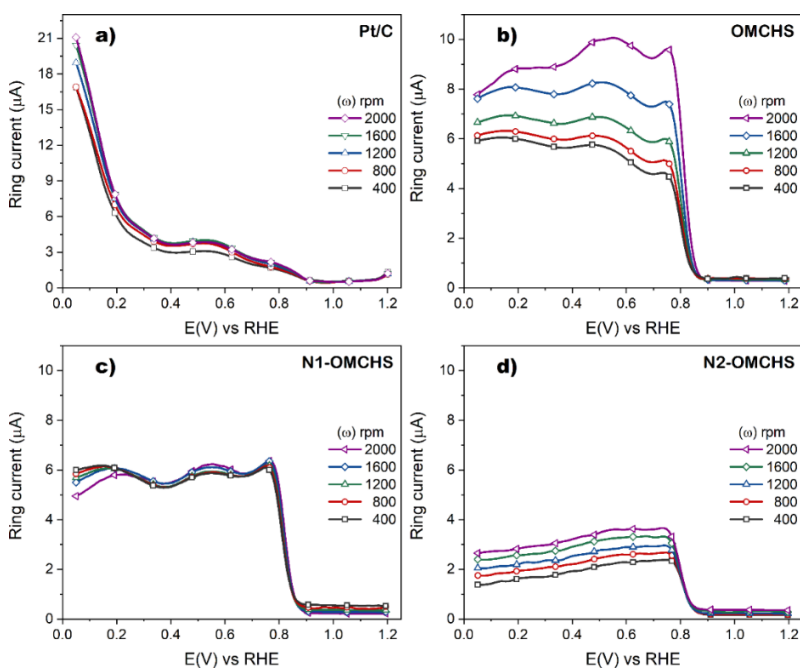


**Fig. 4.7.** Ring-current-potential curves of the ORR at (a) Pt/C, (b) OMCHS, (c) N1-OMCHS, and (d) N2-OMCHS performed in O<sub>2</sub>-saturated 0.5 mol L<sup>-1</sup> KOH, at a scan rate of 5 mV s<sup>-1</sup> at 1<sup>st</sup> cycle.

Table 4.2 also shows the 1<sup>st</sup> cycle half-wave potential ( $E_{1/2}$ ) values of the electrocatalysts, which is a good indicator of the electrocatalyst capability to reduce the overpotential [26]. As can be seen, it is 20 mV more positive at N2-OMCHS (0.82 V/RHE) than those of OMCHS and N1-OMCHS (0.80 V/RHE), and only 70 mV more negative than that of Pt/C (0.89 V/RHE).

**Table 4.2.** Electrochemical parameters of the ORR at the electrocatalysts at the 1<sup>st</sup> and after 3000<sup>th</sup> cycles.

Samples	$E_{\text{onset}}$ (V/RHE)		$E_{1/2}$ (V/RHE)		$j$ at 0.8 V/RHE (mA cm <sup>-2</sup> )		HO <sub>2</sub> <sup>-</sup> (%)		n	
	1 <sup>st</sup>	3000 <sup>th</sup>	1 <sup>st</sup>	3000 <sup>th</sup>	1 <sup>st</sup>	3000 <sup>th</sup>	1 <sup>st</sup>	3000 <sup>th</sup>	1 <sup>st</sup>	3000 <sup>th</sup>
	OMCHS	0.86	0.84	0.80	0.79	-1.14	-0.67	4.8	1.24	3.90
N1-OMCHS	0.87	0.87	0.80	0.81	-1.18	-1.37	8.7	1.17	3.83	3.98
N2-OMCHS	0.88	0.86	0.82	0.80	-2.10	-1.63	3.8	1.67	3.92	3.97
Pt/C	1.01	0.97	0.89	0.86	-3.53	-3.29	2.0	7.90	3.97	3.84

**Table 4.3.** Comparison of the catalytic performance for the ORR in terms of the  $E_{\text{onset}}$ ,  $E_{1/2}$ , n, and %HO<sub>2</sub><sup>-</sup>, of recently reported non-platinum electrocatalysts.

Catalyst	$E_{\text{onset}}$ (V/RHE)	$E_{1/2}$ (V/RHE)	n	HO <sub>2</sub> <sup>-</sup> (%)	Reference
N-Doping of graphene oxide	0.84	0.7	3.91	-- <sup>a</sup>	Chem. Commun., 2017, 53, 873-876.
Trioxotriangulene derivates	0.85	-- <sup>a</sup>	2.71	60	Chem. Commun., 2019, 2, 46-8.
Iron and nitrogen-doped graphene	0.93	0.8	3.80	10	J. Mater. Chem A., 2015, 3, 1058-1067.
Non-doped graphene nanosheets	0.83	-- <sup>a</sup>	3.3	21	ACS Appl. Mater. Interfaces, 2014, 6, 19726-19736.
Cu <sub>6</sub> Ni <sub>7</sub> / thermalized triazine-based frameworks	0.82	0.68	3.94	3.3	Am. Chem. Soc., 2017, 44, 38486-38498.

--<sup>a</sup>: not determined

On other hand,  $j$  values at 0.8 V/RHE (1<sup>st</sup> cycle) are -2.10, -1.18, and -1.14 mA cm<sup>-2</sup> for N2-OMCHS, N1-OMCHS, and OMCHS, respectively. This parameter is smaller at N2-OMCHS compared to Pt/C (Table 4.2); however, the performance of the former is the highest among the carbon-based electrocatalysts.

Figs. 4.5c) and d) show the 1<sup>st</sup> cycle plots of % HO<sub>2</sub><sup>-</sup> and n, calculated from equations (1) and (2), respectively, from data at  $\omega = 2000$  rpm. These electrochemical parameters are also summarized in Table 4.2. N2-OMCHS shows a remarkably high performance with %HO<sub>2</sub><sup>-</sup> = 3.8 % and n = 3.92, very low values which approximate those of Pt/C (%HO<sub>2</sub><sup>-</sup> = 2.0 and n= 3.97). Moreover, it is striking that the performance of OMCHS is better than that of N1-OMCHS. Nevertheless, the results indicate that the ORR at N2-OMCHS, N1-OMCHS, and OMCHS follows a 4e<sup>-</sup> pathway with a very low percentage of HO<sub>2</sub><sup>-</sup> produced. It should be noted

that all the metal-free electrocatalysts synthesized in this chapter have very promising %HO<sub>2</sub><sup>-</sup> and n values compared to other metal-free electrocatalysts reported in the literature (see Table 4.3).

Considering the results of electrochemical parameters so far in Fig. 4.5 and Table 4.2 (1<sup>st</sup> cycle), N2-OMCHS shows an enhanced performance for the ORR, compared to OMCHS and N1-OMCHS. Its high catalytic activity can be attributed to a synergistic effect of nitrogen content (1.65 at. %), degree of graphitization ( $I_D/I_G = 1.25$ ),  $SSA_{DFT}$  ( $873 \text{ m}^2 \text{ g}^{-1}$ ), and an adequate pore volume ( $1.1 \text{ cm}^3 \text{ g}^{-1}$ ), which are decisive factors for generating large amounts of exposed active sites, favoring the electron transfer pathway, and mass transport between electrocatalyst and electrolyte, as reported by Huang *et al.* [27].

#### 4.3. Surface chemical composition of the N-doped OMCHS before ADT

The surface chemical composition of powders of the N-doped OMCHS, determined by XPS, is shown in Table 4.4. The electrocatalysts are composed of carbon (C 1s), oxygen (O 1s), nitrogen (N 1s), and silicon (Si 2p), without additional elements being detected. It calls the attention that OMCHS contains 0.99 at. % Nitrogen, although the presence of this element is attributed to residual ammonium hydroxide used during its synthesis.

**Table 4.4.** Surface chemical composition of OMCHS, N1-OMCHS and N2-OMCHS by XPS.

Samples	C 1s	O 1s	N 1s	Si 2p
	(at. %)			
OMCHS	94.06	4.05	0.99	0.89
N1-OMCHS	91.14	5.74	2.56	0.55
N2-OMCHS	91.38	6.04	1.65	0.93

The nitrogen content increases at N1-OMCHS and N2-OMCHS (2.56 and 1.65 at. %, respectively) confirming the incorporation of nitrogen species during the *in-situ* doping of both electrocatalysts. Moreover, the oxygen concentration increases in the order OMCHS < N1-OMCHS < N2-OMCHS. The presence of low concentrations of silicon at the electrocatalysts (between ca. 0.5 and 0.9 at. %) is due to the residual Si not being removed during the leaching process.

In the same line of analysis, the surface chemical composition of the catalyst inks of OMCHS, N1-OMCHS, and N2-OMCHS, i.e., those deposited on glassy carbon for ORR measurement (and the same used to fill the U-cup in Fig. 3.1), has also been evaluated by XPS prior to ADT.

This analysis has been carried out to study all the chemical species involved during the ORR, including those provided by the Nafion<sup>®</sup> solution used as a binder in this work. This approach is also helpful for comparing the surface chemistry of the electrocatalysts before and after ADT, as shown later. The results of the XPS analysis before ADT are depicted in Fig. 4.8.

First, the deconvolution of the high-resolution C 1s spectra corresponding to the catalyst ink of OMCHS, N1-OMCHS, and N2-OMCHS is shown in Figs. 4.8a-c). Eight peaks have been identified at a binding energy (BE) that corresponds to: C=C sp<sup>2</sup> hybridization (284.7 eV), C-C sp<sup>3</sup> hybridization (285.7 eV), C-O (286.6 eV), C=O (287.6 eV), CF<sub>2</sub>-SO<sub>3</sub>H (288.96 eV), CF (290.4 eV), CF<sub>2</sub> (291.8 eV), and CF<sub>3</sub> (293.1 eV). Therefore, the peaks between a BE of 287 and 294 eV correspond to functional groups related to Nafion<sup>®</sup> [28, 29].

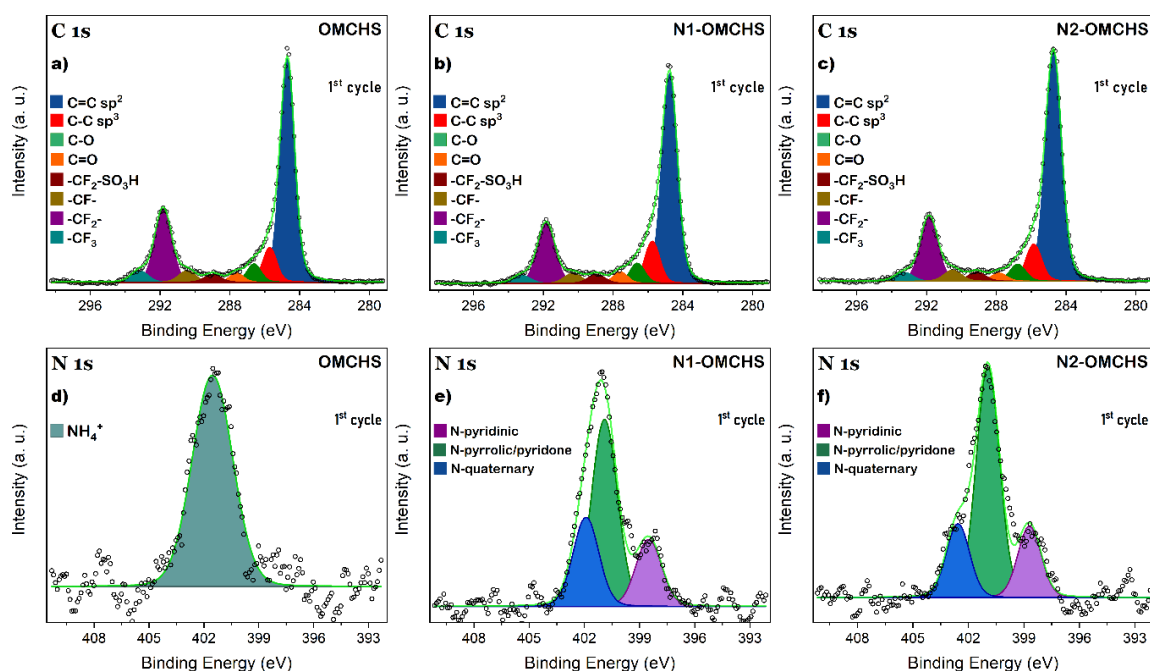


**Fig.4.8.** Deconvolution of high-resolution XPS spectra of the N-doped OMCHS (catalyst inks). (a-c) C 1s and (d-f) N 1s region. 1<sup>st</sup> cycle.

The relative concentration of species at the electrocatalysts before ADT is shown in Table 4.5 (1<sup>st</sup> cycle data). As can be seen, OMCHS, N1-OMCHS, and N2-OMCHS are mainly composed of C=C sp<sup>2</sup> hybridization (56.1, 55.8, and 59.5 at. %, respectively), confirming the presence of a graphitic structure, which is in good agreement with the Raman results. Moreover, as expected, the relative concentration of Nafion<sup>®</sup> species is similar in all electrocatalysts (OMCHS= 29.2, N1-OMCHS= 25.7, and N2-OMCHS= 25.4 at. %).

The relative concentration of C-O plus C=O species at N1-OMCHS (7.9 at. %) increases compared to OMCHS (6.5 at. %) and N2-OMCHS (6.1 at. %). The presence of the C-O and C=O carbonyl groups on the surface of the N-doped OMCHS can be assigned to the functionalization with methanol. Figs. 6.8 d-f) show the deconvolution of the high-resolution spectra in the N 1s region of the electrocatalysts. At OMCHS (Fig 6.8d) a single peak has been identified at BE= 401.52 eV, which corresponds to  $\text{NH}_4^+$  species, confirming that the nitrogen detected in this electrocatalyst is due to the residual ammonia from the synthesis process.

In the case of N1-OMCHS, three peaks are observed (Fig. 4.8e) corresponding to the N-pyridinic (398.49 eV), N-pyrrolic/pyridone (400.89 eV), and N-quaternary (401.90 eV) species. Meanwhile, the same three nitrogen species are detected at N2-OMCHS (Fig. 4.8 f), where the peaks shift towards higher BE: N-pyridinic (398.69 eV), N-pyrrolic/pyridone (400.94 eV), and N-quaternary (402.55 eV). These results confirm the successful nitrogen doping of N1-OMCHS and N2-OMCHS. The nitrogen species of both N-doped OMCHS are the same, with just slight differences in the relative atomic concentration (see Table 4.5). It has been reported that the chemical state of N-pyrrolic and N-pyridone is similar [30, 31], and therefore, it is difficult to distinguish between them.

Now, the nitrogen precursor at N1-OMCHS is 2-pyridinecarboxaldehyde, a molecule formed basically by a pyridine anchored to a hydroxyl group; therefore, it can be inferred that the peak at 400.89 eV in Fig. 4.8e is mainly N-pyridone. Similarly, it can be assumed that the peak at 400.94 eV in N2-OMCHS (Fig. 4.8f) corresponds to N-pyrrolic species because pyrrole is the source of nitrogen.

Regarding the catalytic activity for the ORR, it is widely reported that N-pyridinic species promotes active sites for oxygen adsorption in adjacent carbon atoms due to modifications of the chemical environment [32, 33], and N-quaternary provides active sites which can increase the limiting current density [34, 35]. Moreover, it has been also reported that N-pyrrolic promotes high catalytic activity by improving parameters such as  $E_{\text{onset}}$  and promoting a four-electron mechanism pathway [36].

Furthermore, some authors have speculated that an adequate concentration of the three species (N-pyrrolic, N-pyridinic, and N-quaternary) can enhance the catalytic activity for the ORR of

metal-free electrocatalysts [37, 38]. With this background in mind, the enhanced performance of N2-OMCHS for the ORR (1<sup>st</sup> cycle) can be attributed to the fact that it contains the three nitrogen species that promote the reaction.

On the other hand, despite containing N-pyridinic and N-quaternary, N1-OMCHS has the N-pyridone species which to the best of our knowledge has not been reported to provide catalytic sites for the reaction. On this issue, OMCHS contains only the NH<sup>+</sup> species. In addition to the three N-species, other factors such as SSA<sub>DFT</sub>, pore-volume, and pore size play an important role in the catalytic activity of N2-OMCHS for the ORR.

#### 4.4. Catalytic activity for the ORR and surface chemical composition of the N-doped OMCHS after ADT

Figs. 4.9 a-c) show the polarization curves of the ORR at the N-doped OMCHS in the 1<sup>st</sup> and 3000<sup>th</sup> cycles. After ADT, E<sub>onset</sub> shifts by 20 mV towards more negative values at OMCHS and N2-OMCHS, compared to the 1<sup>st</sup> cycle. The displacement in E<sub>1/2</sub> is of 10 and 20 mV at these electrocatalysts, respectively, after ADT (Table 4.2).

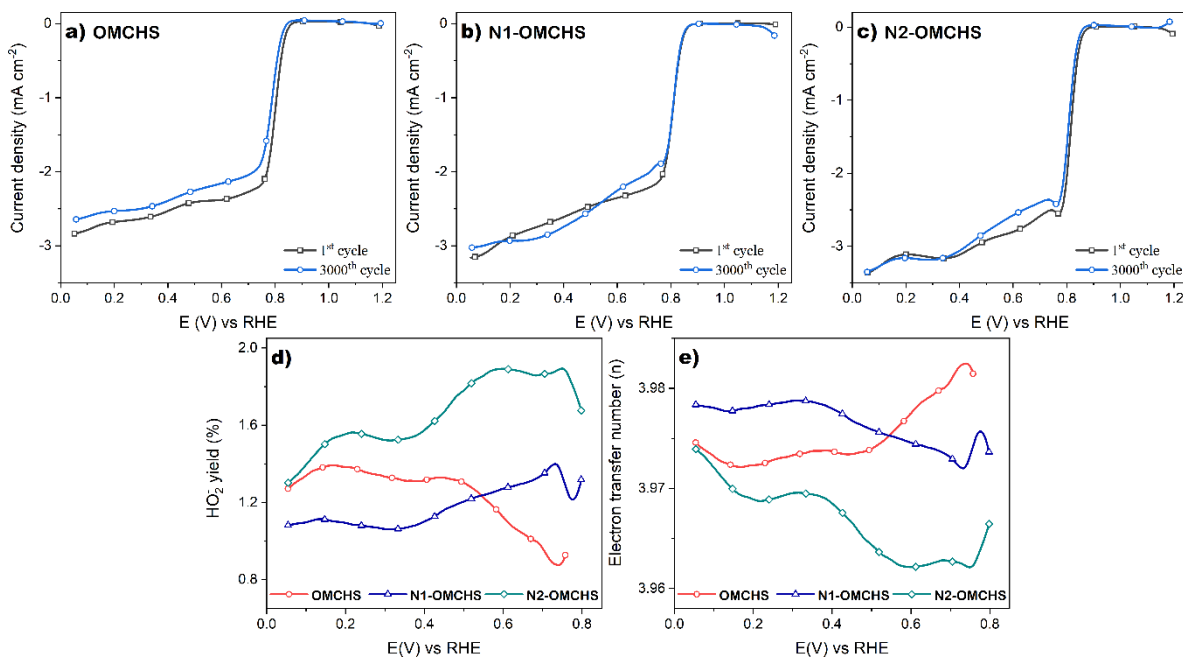


**Fig. 4.9.** Negative scan only of the CVs of the ORR at 2000 rpm (1<sup>st</sup> and 3000<sup>th</sup> cycles) at (a) OMCHS, (b) N1-OMCHS, and (c) N2-OMCHS. Electrolyte: O<sub>2</sub>-saturated 0.5 mol L<sup>-1</sup> KOH, scan rate = 5 mV s<sup>-1</sup> at 2000 rpm. d) %HO<sub>2</sub><sup>-</sup> and e) n plots at the 3000<sup>th</sup> cycle.


In contrast, it is noteworthy to analyze the performance of N1-OMCHS. At this electrocatalyst,  $E_{\text{onset}}$  remains constant and  $E_{1/2}$  shifts 10 mV towards more positive potentials after ADT, which gives an insight into its high electrochemical stability. As a comparison,  $E_{\text{onset}}$  and  $E_{1/2}$  become 40 and 30 mV more negative, respectively, at Pt/C after ADT (Table 4.2). In addition,  $j$  at 0.8 V/RHE decreases after ADT as follows OMCHS > N1-OMCHS > Pt/C (41.6, 22.3, and 6.4 %, respectively), observing an increase only for N2-OMCHS (16 %) in  $j$  after ADT. In the case of  $n$ , there is also a clear increase after ADT, reaching almost a 4  $e^-$  value. These values show superior stability of the metal-free electrocatalysts compared with Pt/C, since here %HO<sub>2</sub><sup>-</sup> shows an almost 4-fold increase, while  $n$  falls to 3.84.

The remarkable high stability of OMCHS, N1-OMCHS, and N2-OMCHS can be largely attributed to their mesoporous structure that keeps the active sites dispersed avoiding their agglomeration, contrary to what happens with the Pt/C electrocatalyst. Therefore, the mesoporous structure not only improves the kinetics and the mass transport of reagents/products in or out of the active sites but also maintains its features after potential cycling in alkaline media [39]. To understand the electrochemical stability and improved performance of OMCHS, N1-OMCHS, and N2-OMCHS towards the ORR, their surface chemical composition after ADT has been analyzed by XPS.

Figs. 4.10 a-c) show the high-resolution spectra in the C1s region of the metal-free electrocatalysts after the 3000<sup>th</sup> cycle. In this BE interval, the same eight signals detected prior to ADT have been identified, with the only difference being a variation in their relative concentration (Table 4.5).

The relative concentrations of the Nafion-related species after ADT are 26.9, 25.2, and 16.7 at. % for OMCHS, N1-OMCHS, and N2-OMCHS, respectively. This means that the relative concentration of the species due to the binder decreases at OMCHS and N2-OMCHS, remaining about the same at N1-OMCHS. It is hypothesized that a lower concentration of Nafion-species may contribute to the detachment of electrocatalyst during cycling, i.e., in the cases of OMCHS and N2-OMCHS.





Since only slight variations are observed in the relative atomic concentration of species in the C 1s region at the electrocatalysts, the analysis has been extended to the high-resolution O 1s region (Fig. 4.11), which provides more detailed information about the modification of the oxidized species before and after ADT.

**Table 4.5.** XPS atomic relative concentration of the C 1s and N1s regions of OMCHS, N1-OMCHS, and N2-OMCHS before (1<sup>st</sup> cycle) and after (3000<sup>th</sup> cycle) ADT.

Samples	State	Species	1 <sup>st</sup> cycle		3000 <sup>th</sup> cycle	
			BE (eV)	Relative concentration (at. %)	BE (eV)	Relative concentration (at. %)
OMCHS	C 1s	C=C	284.68	56.12	284.83	57.82
	C 1s	C-C	285.69	8.18	285.93	8.91
	C 1s	C-O	286.60	4.33	286.89	4.44
	C 1s	C=O	287.59	2.13	288.00	1.90
	C 1s	CF <sub>2</sub> -SO <sub>3</sub> H	288.96	2.17	289.13	2.23
	C 1s	CF	290.43	3.23	290.61	2.37
	C 1s	CF <sub>2</sub>	291.80	20.68	292.24	17.67
	C 1s	CF <sub>3</sub>	293.14	3.16	293.65	4.66
	N 1s	NH <sub>4</sub> <sup>+</sup>	401.52	100	--	--
N1-OMCHS	C 1s	C=C	284.74	55.83	284.71	58.69
	C 1s	C-C	285.74	10.57	285.71	11.27
	C 1s	C-O	286.60	5.05	286.67	3.80
	C 1s	C=O	287.57	2.84	287.69	1.06
	C 1s	CF <sub>2</sub> -SO <sub>3</sub> H	288.94	2.59	289.55	0.80
	C 1s	CF	290.29	2.95	291.02	1.30
	C 1s	CF <sub>2</sub>	291.82	17.84	292.15	18.80
	C 1s	CF <sub>3</sub>	293.20	2.33	293.46	4.28
	N 1s	N-pyridinic	398.49	19.5	398.27	37.0
	N 1s	N-pyrrolic/pyridone	400.89	54.5	400.77	51.1
	N 1s	N-quaternary	401.90	26.0	401.90	11.9
N2-OMCHS	C 1s	C=C	284.71	59.45	284.57	60.16
	C 1s	C-C	285.84	9.05	285.53	15.79
	C 1s	C-O	286.76	4.17	286.20	4.27
	C 1s	C=O	287.83	1.96	287.07	3.08
	C 1s	CF <sub>2</sub> -SO <sub>3</sub> H	289.11	2.42	289.14	1.60
	C 1s	CF	290.48	3.02	290.76	0.63
	C 1s	CF <sub>2</sub>	291.84	17.56	291.95	11.29
	C 1s	CF <sub>3</sub>	293.25	2.37	293.14	3.18
	N 1s	N-pyridinic	398.69	19.0	398.25	22.6
	N 1s	N-pyrrolic/pyridone	400.94	61.3	400.43	51.8
	N 1s	N-quaternary	402.55	19.7	401.85	25.6

Prior to ADT, OMCHS (Fig. 4.11a), N1-OMCHS (Fig. 4.11b), and N2-OMCHS (Fig. 4.11c) show three peaks at 532.3, 533.8 and 535.7 eV corresponding to C=O, SO<sub>3</sub>, C-O, and OCF<sub>2</sub>, respectively. N2-OMCHS (Fig. 4.11c) show the same species, with the addition of a fourth peak at 530.8 eV attributed to C=O. The presence of C-O and C=O is in good agreement with the results of the C 1s region of each electrocatalyst, while the SO<sub>3</sub> and OCF<sub>2</sub> peaks are functional groups of Nafion<sup>®</sup> [40].

The existence of these functional groups can provide a greater surface hydrophilic character, improving the electrocatalyst-electrolyte interaction [41]. Moreover, the electronegativity of oxygen attracts electrons from adjacent carbon atoms, giving them a partially positive charge that could improve the adsorption of intermediate oxygen species during the ORR [42].

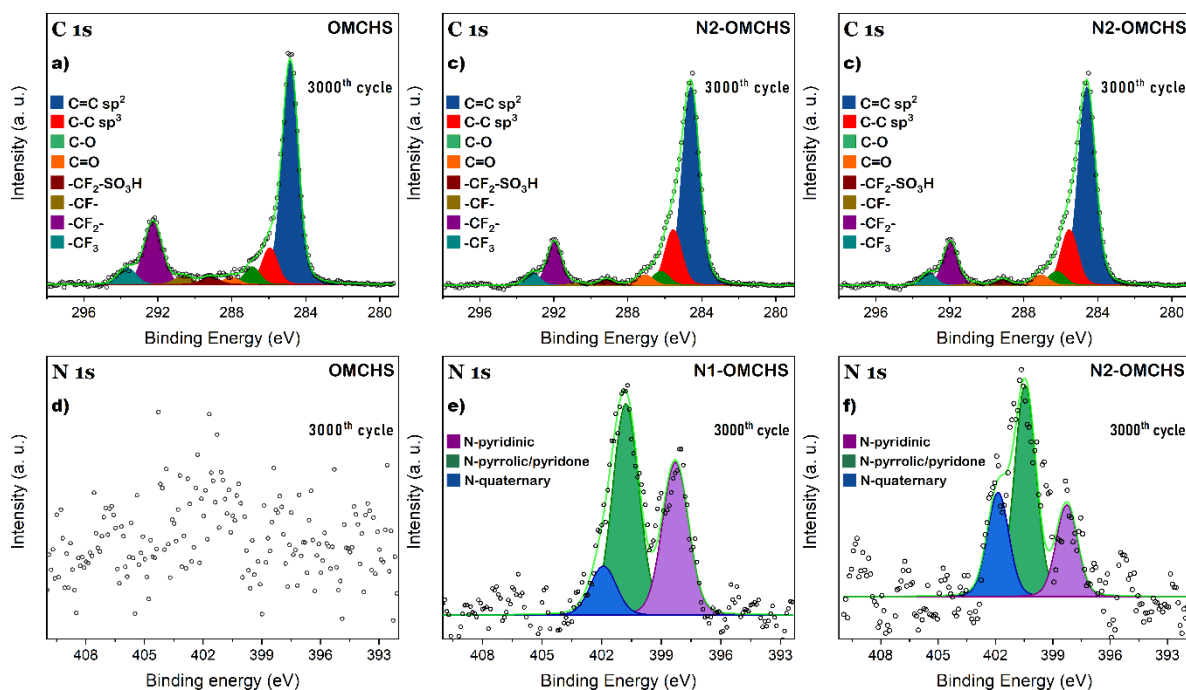


**Fig. 4.10.** Deconvolution of the high-resolution XPS spectra of the N-doped OMCHS (catalyst inks). (a-c) C 1s and (d-f) N 1s region. 3000<sup>th</sup> cycle.

Figs. 4.11 d-f) show the deconvolution of the high-resolution spectra in the O 1s region at the 3000<sup>th</sup> cycle of the electrocatalysts. As can be observed, the relative concentration of the C=O, SO<sub>3</sub>, C-O, and OCF<sub>2</sub>, species change after ADT.

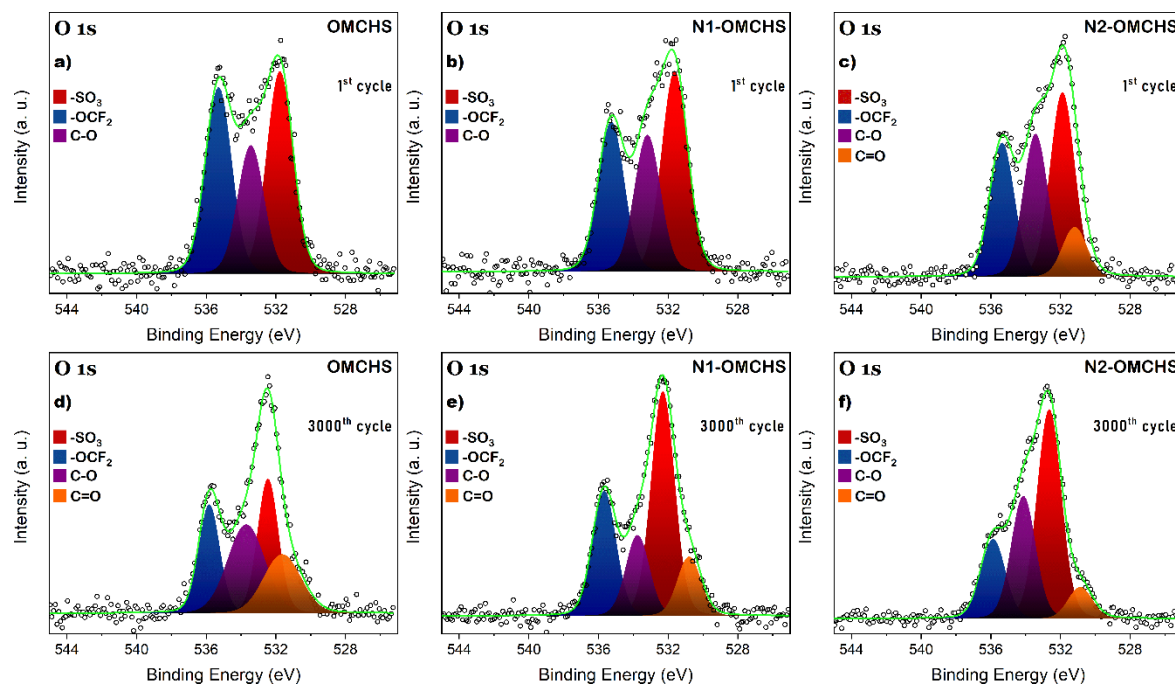


**Fig. 4.11.** XPS O 1s spectra of OMCHS, N1-OMCHS, and N2-OMCHS at the 1<sup>st</sup> and 3000 cycles.

It should be noted that C=O emerges at OMCHS and N1-OMCHS after ADT. On this matter, the increase in the relative concentration of carbonyl species facilitates the pore filling by the electrolyte improving the electrode-electrolyte contact and thus the performance for the ORR [43]. On the other hand, the decrease in the relative intensity of the SO<sub>3</sub> and OCF<sub>2</sub> species can be due to the degradation of Nafion<sup>®</sup> during cycling.

The deconvoluted N 1s region of the electrocatalysts at the 3000<sup>th</sup> cycle is shown in Figs. 4.10 d-f). The OMCHS electrocatalyst no longer shows the signal due to NH<sub>4</sub><sup>+</sup> (Fig. 4.10d), indicating that this species is neither stable nor strongly anchored on the electrocatalyst surface. Meanwhile, N1-OMCHS (Fig. 4.10 e) shows peaks at 398.27, 400.77, and 401.90 eV, attributed to N-pyridinic, N-pyrrolic/pyridone, and N-quaternary with a relative concentration of 37.0, 51.1, and 11.9 at. %, respectively (Table 4.5).

These results confirm that the nitrogen species are modified during potential cycling where possibly the C-N bonds of the N-quaternary species are broken leading to an increase in N-pyridinic species, coupled with the formation of N-pyrrolic species at the expense of a decrease in N-pyridone species. Therefore, the relative concentration of two of the species that promote the catalytic activity for the ORR increases after ADT at N1-OMCHS.

The spectrum of N2-OMCHS after 3000 cycles in Fig. 4.10f shows peaks at 398.69, 400.94, and 402.55 eV, with a relative concentration of 22.6, 51.8, and 25.6 at. %. At this electrocatalyst, the relative concentration of N-pyridinic and N-quaternary species increases after ADT, likely due to a decrease in the concentration of N-pyrrolic/pyridine. Such change can be due to the oxidation of N-pyrrolic to N-quaternary during ADT [44]. The increase in the relative concentration of N-pyridinic and N-quaternary promotes a 4 e<sup>-</sup> pathway and decrease the production of HO<sub>2</sub><sup>-</sup>. Therefore, the electrochemical stability and enhancement in catalytic activity for the ORR of N1-OMCHS, and N2-OMCHS after ADT is related to the modification of their surface chemistry, particularly the N-species.

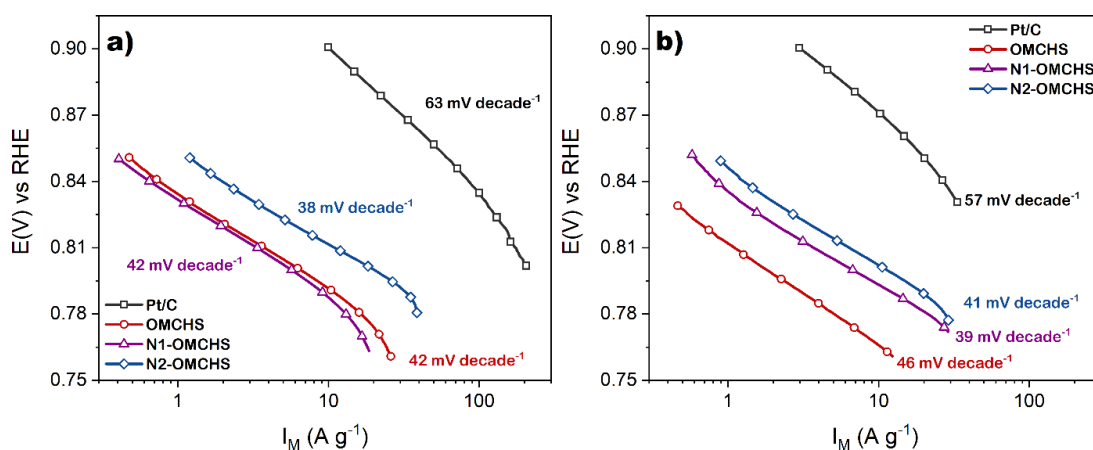


**Fig. 4.12.** The mass catalytic activity of Pt/C, OMCHS, N1-OMCHS, and N2-OMCHS at 2000 rpm at (a) 1<sup>st</sup> cycle and (b) 3000<sup>th</sup> cycle.

Fig. 4.12 shows mass catalytic activity plots of the electrocatalysts. Before ADT, Pt/C has a Tafel slope of 63 mV decade<sup>-1</sup>, close to the value typically expected at low overpotentials (60 mV decade<sup>-1</sup>). The N-doped OMCHS show lower Tafel slope values, indicating their activity to promote a fast ORR. Even though, their mass catalytic activity is lower than that of Pt/C.

After ADT, the mass performance of Pt/C decreases, while that of OMCHS, N1-OMCHS, and N2-OMCHS remains in a similar value as before cycling, confirming their high electrochemical stability. In terms of mass loading, N2-OMCHS shows a higher performance before and after ADT compared to the two other metal-free electrocatalysts.

#### 4.5. Conclusions

The most relevant conclusions of this work are the following:

- It is confirmed that the structural and textural properties, morphology, and surface chemical composition of the metal-free electrocatalysts are directly associated with the nitrogen precursor used during synthesis.
- The incorporation of nitrogen species promotes the formation of N-doped OMCHS structures with greater crystallinity compared to the undoped electrocatalyst.
- The high performance of N1-OMCHS and N2-OMCHS electrocatalysts after ADTs is due to the modification of the nitrogen species during potential cycling. For example, N1-OMCHS shows remarkable high stability due to the modification of N-quaternary to N-pyridinic species, while the N-pyrrolic species oxidizes to N-quaternary at N2-OMCHS.
- This work is a first approximation to evaluate the potential use of N-doped OMCHS as cathode electrocatalysts for Anion Exchange Membrane Fuel Cells applications. The performance of all the metal-free electrocatalysts for the ORR is still lower than that of commercial Pt/C. However, N-doped OMCHS electrocatalysts have remarkably high stability, overcoming Pt/C on this issue.

## References

- [1] M. Ignat, C.J. Van Oers, J. Vernimmen, M. Mertens, S. Potgieter-Vermaak, V. Meynen, E. Popovici, P. Cool. Textural property tuning of ordered mesoporous carbon obtained by glycerol conversion using SBA-15 silica as template. *Carbon*. 48 (2010) 1609–1618.
- [2] J.C. Carrillo-Rodríguez, S. García-Mayagoitia, R. Pérez-Hernández, M.T. Ochoa-Lara, F. Espinosa-Magaña, F. Fernández-Luqueño, P. Bartolo-Pérez, I.L. Alonso-Lemus, F.J. Rodríguez-Varela. Evaluation of the novel Pd CeO<sub>2</sub>-NR electrocatalyst supported on N-doped graphene for the Oxygen Reduction Reaction and its use in a Microbial Fuel Cell. *J. Power Sources*. 414 (2019) 103–114.
- [3] K.N. Kudin, B. Ozbas, H.C. Schniepp, R.K. Prud'homme, I.A. Aksay, R. Car. Raman Spectra of Graphite Oxide and Functionalized Graphene Sheets. *Nano Lett.* 8 (2008) 36–41.
- [4] A. Sadezky, H. Muckenhuber, H. Grothe, R. Niessner, U. Pöschl. Raman microspectroscopy of soot and related carbonaceous materials: Spectral analysis and structural information. *Carbon* 43 (2005) 1731–1742.
- [5] A. Kaniyoor, S. Ramaprabhu. A Raman spectroscopic investigation of graphite oxide derived graphene. *AIP Adv.* 2 (2012).
- [6] J. Xu, S. Su, Z. Sun, M. Qing, Z. Xiong, Y. Wang, L. Jiang, S. Hu, J. Xiang. Effects of steam and CO<sub>2</sub> on the characteristics of chars during devolatilization in oxy-steam combustion process. *Appl. Energy* 182 (2016) 20–28.
- [7] S. Vollebregt, R. Ishihara, F.D. Tichelaar, Y. Hou, C.I.M. Beenakker. Influence of the growth temperature on the first and second-order Raman band ratios and widths of carbon nanotubes and fibers. *Carbon*. 50 (2012) 3542–3554.
- [8] P.A. Goodman, H. Li, Y. Gao, Y.F. Lu, J.D. Stenger-Smith, J. Redepenning. Preparation and characterization of high surface area, high porosity carbon monoliths from pyrolyzed bovine bone and their performance as supercapacitor electrodes. *Carbon* 55 (2013) 291–298.
- [9] O. Beyssac, B. Goffé, J.P. Petitet, E. Froigneux, M. Moreau, J.N. Rouzaud. On the characterization of disordered and heterogeneous carbonaceous materials by Raman spectroscopy. *Spectrochim. Acta - Part A Mol. Biomol. Spectrosc.* 59 (2003) 2267–2276.
- [10] X. He, X. Liu, B. Nie, D. Song. FTIR and Raman spectroscopy characterization of functional groups in various rank coals. *Fuel* 206 (2017) 555–563.
- [11] S. Claramunt, A. Varea, D. López-Díaz, M.M. Velázquez, A. Cornet, A. Cirera. The Importance of Interbands on the Interpretation of the Raman Spectrum of Graphene Oxide. *J. Phys. Chem. C* 119 (2015) 10123–10129.
- [12] I.A. Pašti, N.M. Gavrilov, A.S. Dobrota, M. Momčilović, M. Stojmenović, A. Topalov, D.M. Stanković, B. Babić, G. Ćirić-Marjanović, S. V. Mentus. The Effects of a Low-Level Boron, Phosphorus, and Nitrogen Doping on the Oxygen Reduction Activity of Ordered Mesoporous Carbons. *Electrocatalysis* 6 (2015) 498–511.
- [13] L. Sui, Y. Wang, W. Ji, H. Kang, L. Dong, L. Yu. N-doped ordered mesoporous carbon/graphene composites with supercapacitor performances fabricated by evaporation induced self-assembly. *Int. J. Hydrogen Energy* 42 (2017) 29820–29829.
- [14] J. Zhu, J. Yang, R. Miao, Z. Yao, X. Zhuang, X. Feng. Nitrogen-enriched, ordered mesoporous carbons for potential electrochemical energy storage. *J. Mater. Chem. A* 4 (2016) 2286–2292.
- [15] M. Thommes, K. Kaneko, A. V. Neimark, J.P. Olivier, F. Rodriguez-Reinoso, J. Rouquerol, K.S.W. Sing. Physisorption of gases, with special reference to the evaluation of surface area and pore size distribution (IUPAC Technical Report). *Pure Appl. Chem.* 87 (2015) 1051–1069.
- [16] A. Chen, Y. Yu, Y. Li, Y. Wang, Y. Li, S. Li, K. Xia. Synthesis of macro-mesoporous carbon materials and hollow core/mesoporous shell carbon spheres as supercapacitors. *J. Mater. Sci.* 51 (2016) 1–8.
- [17] T. Cai, W. Xing, Z. Liu, J. Zeng, Q. Xue, S. Qiao, Z. Yan. Superhigh-rate capacitive performance of heteroatoms-doped double shell hollow carbon spheres. *Carbon* 86 (2015) 235–244.

- [18] J. Liu, X. Wang, J. Gao, Y. Zhang, Q. Lu, M. Liu. Hollow porous carbon spheres with hierarchical nanoarchitecture for application of the high-performance supercapacitors. *Electrochim. Acta* 211 (2016) 183–192.
- [19] Z. Guo, C. Li, W. Li, H. Guo, X. Su, P. He, Y. Wang, Y. Xia. Ruthenium oxide coated ordered mesoporous carbon nanofiber arrays: A highly bifunctional oxygen electrocatalyst for rechargeable Zn-air batteries. *J. Mater. Chem. A* 4 (2016) 6282–6289.
- [20] Q. Zhang, L. Li, Y. Wang, Y. Chen, F. He, S. Gai, P. Yang. Uniform fibrous-structured hollow mesoporous carbon spheres for high-performance supercapacitor electrodes. *Electrochim. Acta* 176 (2015) 542–547.
- [21] C. Yuan, X. Liu, M. Jia, Z. Luo, J. Yao. Facile preparation of N- and O-doped hollow carbon spheres derived from poly(o-phenylenediamine) for supercapacitors. *J. Mater. Chem. A* 3 (2015) 3409–3415.
- [22] Z. Yan, L. Gao, C. Dai, M. Zhang, X. Lv, P.K. Shen. Metal-free mesoporous carbon with higher contents of active N and S codoping by template method for superior ORR efficiency to Pt/C. *Int. J. Hydrogen Energy* 43 (2018) 3705–3715.
- [23] J. Zhang, M. Lv, D. Liu, L. Du, Z. Liang. Nitrogen-doped carbon nanoflower with superior ORR performance in both alkaline and acidic electrolyte and enhanced durability. *Int. J. Hydrogen Energy* 43 (2018) 4311–4320.
- [24] G.A. Ferrero, A.B. Fuertes, M. Sevilla, M.-M.M. Titirici. Efficient metal-free N-doped mesoporous carbon catalysts for ORR by a template-free approach. *Carbon* 106 (2016) 179–187.
- [25] J. Tang, J. Liu, C. Li, Y. Li, M.O. Tade, S. Dai, Y. Yamauchi. Synthesis of nitrogen-doped mesoporous carbon spheres with extra-large pores through assembly of diblock copolymer micelles. *Angew. Chem. Int. Ed. Engl.* 54 (2015) 588–93.
- [26] C. Wang, L. Ma, L. Liao, S. Bai, R. Long, M. Zuo, Y. Xiong. A unique platinum-graphene hybrid structure for high activity and durability in oxygen reduction reaction. *Sci. Rep.* 3 (2013) 2580.
- [27] J. Huang, J. Han, T. Gao, X. Zhang, J. Li, Z. Li, P. Xu, B. Song. Metal-free nitrogen-doped carbon nanoribbons as highly efficient electrocatalysts for oxygen reduction reaction. *Carbon* 124 (2017) 34–41.
- [28] K.J. Peng, J.Y. Lai, Y.L. Liu. Preparation of poly(styrenesulfonic acid) grafted Nafion with a Nafion-initiated atom transfer radical polymerization for proton exchange membranes. *RSC Adv.* 7 (2017) 37255–37260.
- [29] A.K. Friedman, W. Shi, Y. Losovyj, A.R. Siedle, L.A. Baker. Mapping Microscale Chemical Heterogeneity in Nafion Membranes with X-ray Photoelectron Spectroscopy. *J. Electrochem. Soc.* 165 (2018) H733–H741.
- [30] W. Kiciński, M. Norek, B.J. Jankiewicz. Heterogeneous carbon gels: N-doped carbon xerogels from resorcinol and n-containing heterocyclic aldehydes. *Langmuir* 30 (2014) 14276–14285.
- [31] S. Biniak, G. Szymański, J. Siedlewski, A. Świątkoski. The characterization of activated carbons with oxygen and nitrogen surface groups. *Carbon* 35 (1997) 1799–1810.
- [32] R. Wang, H. Wang, T. Zhou, J. Key, Y. Ma, Z. Zhang, Q. Wang, S. Ji. The enhanced electrocatalytic activity of okara-derived N-doped mesoporous carbon for oxygen reduction reaction. *J. Power Sources* 274 (2015) 741–747.
- [33] R. Ma, G. Lin, Y. Zhou, Q. Liu, T. Zhang, G. Shan, M. Yang, J. Wang. A review of oxygen reduction mechanisms for metal-free carbon-based electrocatalysts. *npj Comput. Mater.* 5 (2019) 78.
- [34] X. Liu, L. Dai. Carbon-based metal-free catalysts. *Nat. Rev. Mater.* 1 (2016) 16064.
- [35] Z. Yang, H. Nie, X. Chen, X. Chen, S. Huang. Recent progress in doped carbon nanomaterials as effective cathode catalysts for fuel cell oxygen reduction reaction. *J. Power Sources* 236 (2013) 238–249.
- [36] S.M. Unni, S. Devulapally, N. Karjule, S. Kurungot. Graphene enriched with pyrrolic coordination of the doped nitrogen as an efficient metal-free electrocatalyst for oxygen reduction. *J. Mater. Chem.* 22 (2012) 23506–23513.
- [37] T. Sharifi, G. Hu, X. Jia, T. Wågberg. Formation of Active Sites for Oxygen Reduction Reactions by Transformation of Nitrogen Functionalities in Nitrogen-Doped Carbon Nanotubes. *ACS Nano* 6 (2012) 8904–8912.



- [38] X. Bai, Y. Shi, J. Guo, L. Gao, K. Wang, Y. Du, T. Ma. Catalytic activities enhanced by abundant structural defects and balanced N distribution of N-doped graphene in oxygen reduction reaction. *J. Power Sources* 306 (2016) 85–91.
- [39] G.A. Ferrero, K. Preuss, A.B. Fuertes, M. Sevilla, M.M. Titirici. The influence of pore size distribution on the oxygen reduction reaction performance in nitrogen doped carbon microspheres. *J. Mater. Chem. A* 4 (2016) 2581–2589.
- [40] I.-K. Oh, J.-H. Jung, J.-H. Jeon, S. Vadahanambi. Electro-chemo-mechanical characteristics of fullerene-reinforced ionic polymer–metal composite transducers. *Smart Mater. Struct.* 19 (2010) 075009.
- [41] Y.C. Hsieh, J.Y. Chen, P.W. Wu. Electrochemical degradation of Nafion ionomer to functionalize carbon support for methanol electro-oxidation. *J. Power Sources* 196 (2011) 8225–8233.
- [42] Z. Liu, Z. Zhao, Y. Wang, S. Dou, D. Yan, D. Liu, Z. Xia, S. Wang. In Situ Exfoliated, Edge-Rich, Oxygen-Functionalized Graphene from Carbon Fibers for Oxygen Electrocatalysis. *Adv. Mater.* 29 (2017) 1606207.
- [43] K.H. Kangasniemi, D.A. Condit, T.D. Jarvi. Characterization of Vulcan Electrochemically Oxidized under Simulated PEM Fuel Cell Conditions. *J. Electrochem. Soc.* 151 (2004) E125.
- [44] V. Perazzolo, E. Građzka, C. Durante, R. Pilot, N. Vicentini, G.A. Rizzi, G. Granozzi, A. Gennaro. Chemical and Electrochemical Stability of Nitrogen and Sulphur Doped Mesoporous Carbons. *Electrochim. Acta* 197 (2016) 251–262.

## CHAPTER V.

### Influence of the sulfur and nitrogen species on catalytic activity to the ORR of N-S-co-doped OMCHS after ADT: a study of the performance and stability

#### 5.1. Physicochemical characterization of N-S-doped OMCHS

Fig. 5.1 displays the Raman spectra of S-OMCHS, N1-S-OMCHS, and N2-S-OMCHS, having the typical signals of carbon-based materials: i) D band at ca.  $1329\text{ cm}^{-1}$  related to lattice disorder, attributed to the C-C vibrations of the  $\text{sp}^3$  defect sites; and ii) the G signal at ca.  $1588\text{ cm}^{-1}$  corresponding to  $\text{sp}^2$  hybridization from C=C bonds (graphitized lattice) due to  $\pi$  interactions [1, 2]. The Raman spectral analysis grants the evaluation of the disorder and defects in carbon materials through the measurement of the D and G intensity ratio. The  $I_D/I_G$  ratios of S-OMCHS, N1-S-OMCHS, and N2-S-OMCHS are 1.57, 1.67, and 1.84, respectively.

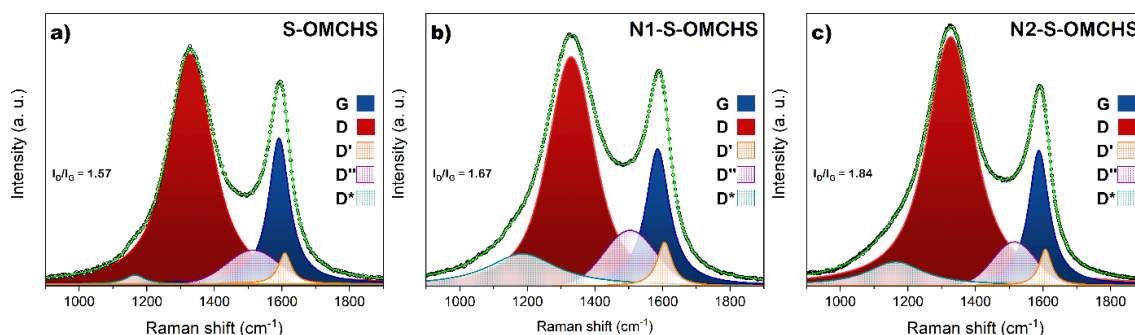


**Fig. 5.1.** Raman spectra of (a) S-OMCHS, (b) N1-S-OMCHS, and (c) N2-S-OMCHS. The G, D, D', and D\* bands were fitted with a Lorentzian function, whereas the D'' band was fitted with a Gaussian function.

It can be noticed that the  $I_D/I_G$  ratio increases when the carbon structures are co-doped with nitrogen and sulfur species. These are higher than those of OMCHS, N1-OMCHS, and N2-OMCHS in Chapter 4 (1.51, 1.44, and 1.32, respectively). This feature suggests that using two different heteroatoms as dopants promotes the formation of less ordered structures. The substitutional co-doping influences the OMCHS, expanding their lattice due to the presence of aromatic groups and  $\text{sp}^3$  bonds, which increases the intensity of the D interband (defective sites). Nevertheless, it is necessary to re-examine whether the  $I_D/I_G$  ratio provides accurate information, especially in high amorphous carbon because attenuates all the Raman interbands [3, 4].

The Raman deconvolution spectra have been investigated to find alternatives to the  $I_D/I_G$  ratio showing the formation of five interband: D' (ca.  $1607\text{ cm}^{-1}$ ), D'' (ca.  $1510\text{ cm}^{-1}$ ), and D\* (ca.

1173  $\text{cm}^{-1}$ ) interbands. The D' interband correspond to stretching vibrations of aromatic rings in graphite crystallites shielded by oxygen functional groups or attached to edge carbon atoms. Meanwhile, the D'' interband is explained by asymmetric vibrational stretching modes of  $\text{sp}^2$  carbons near defects, causing out-of-plane deformations. Nevertheless, the origin of the D'' interband is still discussed [5–9]. The  $I_{\text{D}''}/I_{\text{G}}$  ratios are increasing in the order S-OMCHS < N2-S-OMCHS < N1-S-OMCHS (0.23 < 0.32 < 0.41, respectively). This increase in  $I_{\text{D}''}/I_{\text{G}}$  ratios is in accord with the investigation by Claramunt *et al.* show that the intensity of the G interband decreases when the intensity of the D'' interband increases [10].

Meanwhile, the D\* interband can be attributed to amorphous impurities in the graphitic lattice, adsorbed ions, or stretching vibrations of the  $\text{sp}^2$ - $\text{sp}^3$  bonds of polyene-like structures [11–13]. The  $I_{\text{D}^*}/I_{\text{G}}$  ratio intensity is 0.06, 0.24, and 0.18 for S-OMCHS, N1-S-OMCHS, and N2-S-OMCHS, respectively. N1-S-OMCHS shows the highest  $I_{\text{D}''}/I_{\text{G}}$  and  $I_{\text{D}^*}/I_{\text{G}}$  ratios indicating a high defects number, indicating a high number of defects, favouring oxygen chemisorption by interrupting  $\pi$  conjugation on the electrocatalyst surface [14–16].

The XRD patterns of S-OMCHS, N1-S-OMCHS, and N2-S-OMCHS are shown in Fig. 5.2a). The three patterns show two well-defined peaks, the first at  $2\theta$  around  $23\text{--}25^\circ$ , which are assigned to the (002) plane of the graphite interlayer. The second peak at  $\sim 44^\circ$  ( $2\theta$ ) corresponds to the (101) graphite plane [17]. A slight shift towards a higher angle is observed for the (002) plane by more than  $1^\circ$  ( $2\theta$ ) in the N/S co-doped OMCHS when compared to S-OMCHS electrocatalyst. This displacement of the (002) plane indicates a decrease in the interlayer distance of the N/S-doped OMCHS electrocatalysts.

When comparing the (002) plane of the S-OMCHS and N/S-doped OMCHS with the electrocatalysts of the previous chapter (OMCHS and N-doped OMCHS), two observations can be made: i) S-OMCHS shows a shift in the (002) plane compared to OMCHS, and ii) N1-S-OMCHS and N2-S-OMCHS have the most important displacement regarding that reflection, which confirm the important lattice contraction when co-doping OMCHS. The carbons materials that are obtained at a lower temperature of synthesis, lower rate of temperature increase during the pyrolysis and short time of annealing are characterized by greater interplanar distances [18–19].

Fig. 5.2b) shows the N<sub>2</sub> adsorption/desorption isotherms of the metal-free electrocatalysts, which show a hysteresis loop characteristic of type IV(a) isotherms. The N1-S-OMCHS and N2-S-OMCHS show an H1-type hysteresis, indicating the presence of a mesopore framework with a uniform size, which is characteristic of mesoporous materials [20, 21]. On the other hand, the S-OMCHS isotherm shows a combination of H2(a) and H3-type hysteresis. As mentioned in the previous chapter, this behavior within P/P<sub>0</sub> intervals of 0.40 to 0.79 and 0.80 to 0.90 is attributed to the initial filling of the mesoporous of the shell, followed by the adsorption of N<sub>2</sub> in the hollow core [22, 23].

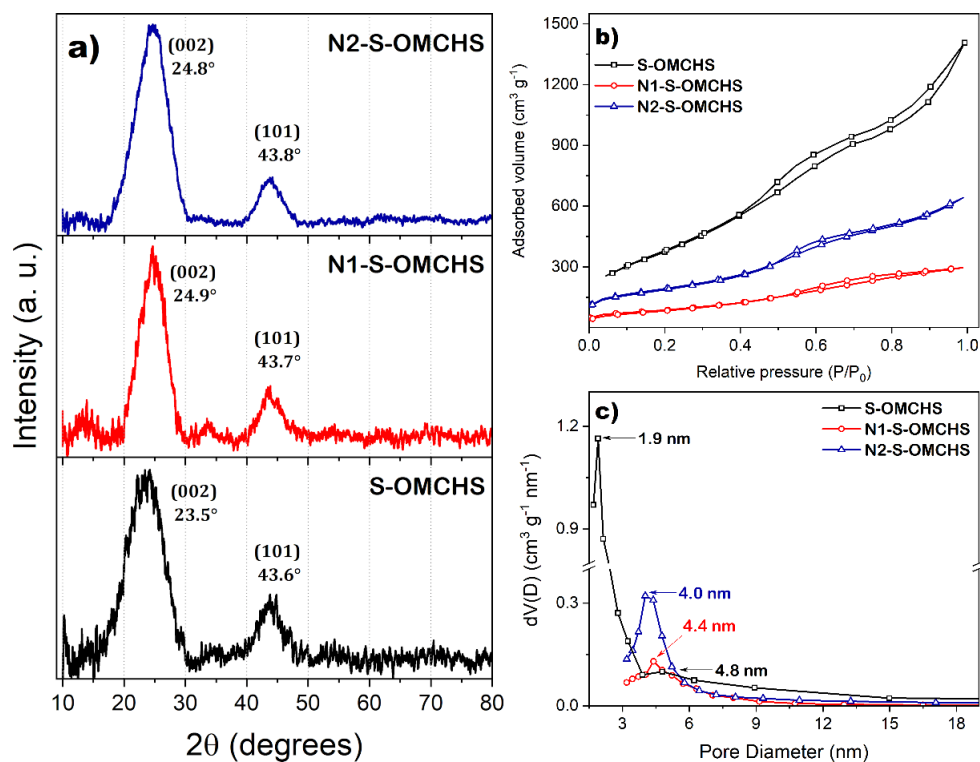


**Fig. 5.2.** (a) XRD patterns, (b) N<sub>2</sub> adsorption-desorption isotherms, and (c) BJH desorption pore size distribution of S-OMCHS, N1-S-OMCHS, and N2-S-OMCHS.

The textural properties of the metal-free electrocatalysts are summarized in Table 5.1. The specific surface area ( $SSA_{DFT}$ ) is 1007, 283, and 622 m<sup>2</sup> g<sup>-1</sup> for S-OMCHS, N1-S-OMCHS, and N2-S-OMCHS, respectively. Co-doping results in a significantly lower  $SSA_{DFT}$  (particularly for N1-S-OMCHS) while doping only with the S heteroatom increases it to a value even higher than that of non-doped OMCHS (810 m<sup>2</sup> g<sup>-1</sup>, Chapter 4).

The average pore size distribution curves (Fig. 5.2c) show the existence of rough nanopores (1.9 nm) in S-OMCHS, with large mesopores centred at 4.8 nm, which pore size is in the shell of the carbon spheres. Meanwhile, N1-S-OMCHS and N2-S-OMCHS have an average pore size distribution centred at 4.4 and 4.0 nm, respectively, indicating their mesoporous nature in the shell. These are higher than those of OMCHS, N1-OMCHS and N2-OMCHS (2.0, 1.7, and 1.7 nm, respectively, Chapter 4). The pore volume is 1.88, 0.43, and 0.91 cm<sup>3</sup> g<sup>-1</sup> for S-OMCHS, N1-S-OMCHS, and N2-S-OMCHS, respectively. S-OMCHS shows a higher pore volume even higher than that of OMCHS (1.37 cm<sup>3</sup> g<sup>-1</sup>, Chapter 4). Moreover, N/S co-doped OMCHS have the lowest pore volume than those of N1-OMCHS and N2-OMCHS (0.94 and 1.11 cm<sup>3</sup> g<sup>-1</sup>, Chapter 4).

These results suggest that the mixture of 2-pyridinecarboxaldehyde/2-thiophenemethanol and pyrrole/2-thiophenemethanol as nitrogen/sulfur sources are responsible for the variations in the SSA<sub>DFT</sub> and pore features. The combination of these nitrogen/sulfur sources can form non-graphitic carbon structures after pyrolysis, and these have a higher tendency to collapse resulting in higher pore size and lower SSA<sub>DFT</sub> [24, 25].

**Table 5.2.** Textural, and morphological features of S-OMCHS, N1-S-OMCHS, and N2-S-OMCHS.

Sample	SSA <sub>DFT</sub> (m <sup>2</sup> g <sup>-1</sup> )	Average pore size (nm)	Pore volume (cm <sup>3</sup> g <sup>-1</sup> )	Average diameter (avg., nm)	Wall thickness (avg., nm)
S-OMCHS	1007	1.9	1.88	262 ± 15	45
N1-S-OMCHS	283	4.4	0.43	260 ± 19	46
N2-S-OMCHS	622	4.0	0.91	-- <sup>a</sup>	-- <sup>a</sup>

--<sup>a</sup>: not determined

FE-SEM images of S-OMCHS and N1-S-OMCHS are shown in Figs. 5.3 a-b), both having a well-defined morphology of rough nanospheres. Nevertheless, the spheres forming N1-S-OMCHS are rougher and more irregular in shape than that of S-OMCHS, a relevant feature attributed to the co-doping with both heteroatoms. The micrograph of N1-S-OMCHS shows several spheres broken due to the leaching of the hard core. Even though, the average diameter of both electrocatalysts is rather similar (Table 5.1). Figs. 5.3c-d) show TEM images of S-OMCHS and N1-S-OMCHS, respectively, at which the effect of co-doping with sulfur-nitrogen compared to mono-heteroatom doping on their morphology is more clearly observed. The rough

sphere of S-OMCHS shows a relatively thin hollow-shell interface and a rather homogeneous wall thickness.

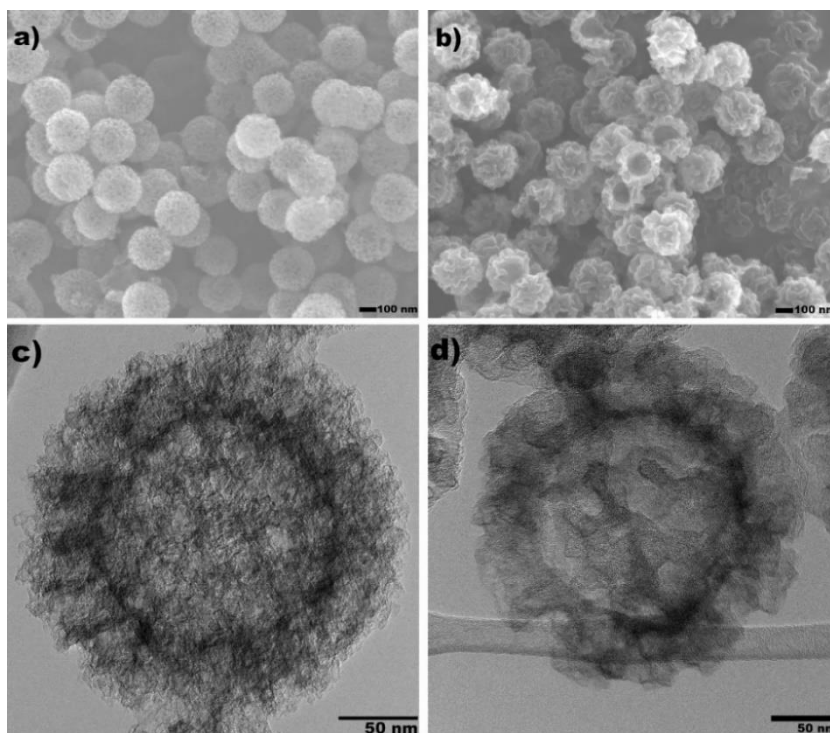


**Fig. 5.3.** FE-SEM and TEM images of (a, c) S-OMCHS and (b, d) N1-S-OMCHS.

On the contrary, N1-S-OMCHS has an irregular wall with some pits in the outer layer, along with a less defined and thicker hollow-shell interface. This morphology resembles that of N1-OMCHS (Chapter 4). These features are responsible for the low  $SSA_{DFT}$  value of N1-S-OMCHS. However, the wall-thickness is about the same for both electrocatalysts (Table 5.1). It was not possible to obtain FE-SEM and TEM images of the N2-S-OMCHS electrocatalyst.

## 5.2. Catalytic activity of the N/S co-doped OMCHS for the ORR

Fig. 5.4a) shows the CVs of S-OMCHS, N1-S-OMCHS, and N2-S-OMCHS, with a semi-rectangular shape that indicates an effect of electronic double-layer capacitance by non-faradaic processes. The  $j$  values of S-OMCHS are higher compared with the two other electrocatalysts, in good accordance with its higher  $SSA_{DFT}$ . In the case of the co-doped electrocatalysts, there is a discrepancy between the  $j$  generated and  $SSA_{DFT}$  value. Although N1-S-OMCHS has the smallest surface area, it delivers a higher  $j$  than N2-S-OMCHS, which suggests that other surface phenomena besides  $SSA_{DFT}$  influences the electrochemical behavior of the co-doped

electrocatalysts (e.g., enhanced electrocatalyst-electrolyte interactions). N2-S-OMCHS generates a lower  $j$  than N2-OMCHS (Chapter 4), indicating that the use of these sources of heteroatoms may hinder such electrocatalyst-electrolyte interaction reducing its electrochemical performance. Meanwhile, N1-S-OMCHS has about the same behavior as N1-OMCHS in Chapter 4.

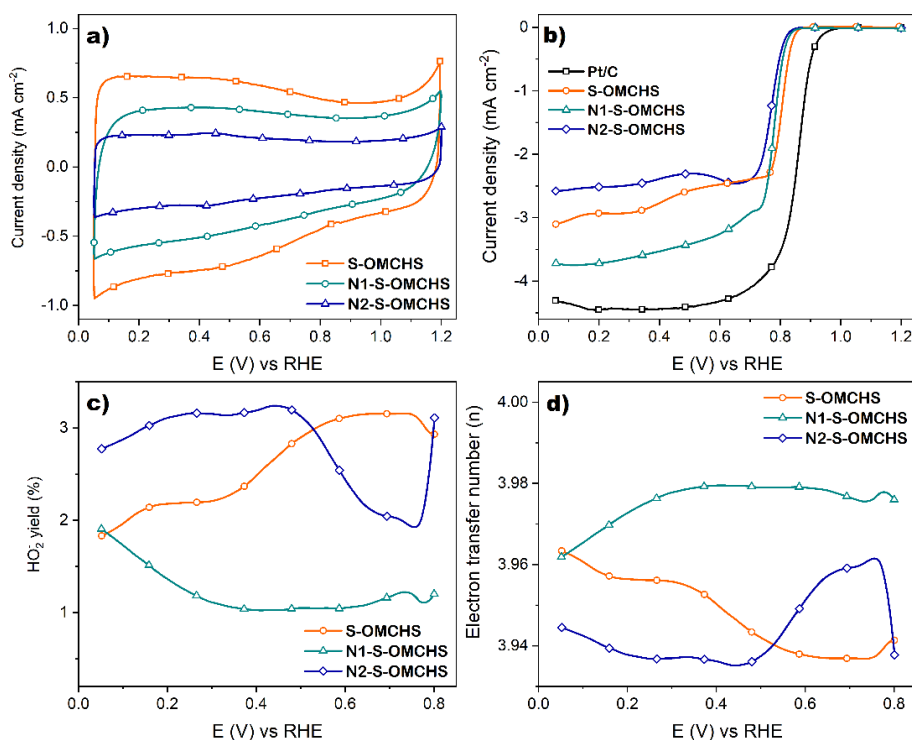


**Fig.5.4.** (a) CVs of S-OMCHS, N1-S-OMCHS, and N2-S-OMCHS were collected at 20 mV s<sup>-1</sup>. Electrolyte: N<sub>2</sub>-saturated 0.5 mol L<sup>-1</sup> KOH. (b) Negative scan only of the CVs of the ORR at 2000 rpm of S-OMCHS, N1-S-OMCHS, N2-S-OMCHS, and Pt/C. Electrolyte: O<sub>2</sub>-saturated 0.5 mol L<sup>-1</sup> KOH. (c) %HO<sub>2</sub><sup>-</sup>, and (d) n plots at the electrocatalysts.

Polarization curves of the ORR at 2000 rpm of the metal-free and Pt/C electrocatalysts are shown in Fig. 5.4b). The  $E_{\text{onset}}$  at 1<sup>st</sup> cycle (0.88 V/RHE, Table 5.2) of S-OMCHS is more positive than those of N1-S-OMCHS and N2-S-OMCHS, confirming the advantageous effect of the S heteroatom on this electrochemical parameter. The  $E_{\text{onset}}$  of S-OMCHS is more positive also than that of some recent works of S-doped carbon materials. Several groups have reported  $E_{\text{onset}}$  values of S-doped porous graphene frameworks (0.77 V/RHE [26]), S-doped reduces graphene oxide (0.74 V/RHE [27]), S-doped carbon nanohorns (0.60 V/RHE [28]), and S-doped ordered mesoporous carbon (0.85 V/RHE [29]).

Meanwhile, the  $E_{\text{onset}}$  values of N1-S-OMCHS and N2-S-OMCHS (0.86 and 0.85 V/RHE, Table 5.2) are lower and in one case similar to those of some recent works of N/S co-doped carbon materials, i.e., N/S co-doped porous carbon nanosphere (1.01 V/RHE [30]), N/S self-doped biocarbon (0.88 V/RHE [31]). N/S co-doped granular carbon (0.85 V/RHE [32]), N/S-doped carbon nanotubes (0.95 V/RHE [33]), N/S-doped porous carbons (0.91 V/RHE [34]).

**Table 5.2.** Electrochemical parameters of the ORR at N/S co-doped OMCHS at the 1<sup>st</sup> and after 3000<sup>th</sup> cycles.

Samples	$E_{\text{onset}}$		$E_{1/2}$		$j$ at 0.8 V/RHE		$\text{HO}_2^-$ at 0.4 V/RHE		$n$ at 0.4 V/RHE	
	(V/RHE)		(V/RHE)		(mA cm <sup>-2</sup> )		(%)			
	1 <sup>st</sup>	3000 <sup>th</sup>	1 <sup>st</sup>	3000 <sup>th</sup>	1 <sup>st</sup>	3000 <sup>th</sup>	1 <sup>st</sup>	3000 <sup>th</sup>	1 <sup>st</sup>	3000 <sup>th</sup>
S-OMCHS	0.88	0.88	0.81	0.82	-1.49	-1.69	2.4	1.11	3.95	3.97
N1-S-OMCHS	0.86	0.88	0.78	0.78	-0.60	-0.72	1.0	1.90	3.97	3.96
N2-S-OMCHS	0.85	0.84	0.77	0.76	-0.42	-0.30	3.2	4.10	3.93	3.91

Table 5.2 shows the 1<sup>st</sup> cycle  $E_{1/2}$  values of the S-doped and N/S co-doped OMCHS electrocatalyst. It is 30 and 40 more positive at S-OMCHS (0.81 V/RHE) compared to N1-S-OMCHS (0.78 V/RHE) and N2-S-OMCHS (0.77 V/RHE), respectively. Moreover, the  $j$  values at 0.8 V/RHE (Table 5.2, 1<sup>st</sup> cycle) are -1.49, -0.60, and -0.42 mA cm<sup>-2</sup> for S-OMCHS, N1-S-OMCHS, and N2-S-OMCHS, respectively. However, considering the electrochemical parameters so far discussed, S-OMCHS has a higher catalytic activity than the co-doped electrocatalysts. N1-S-OMCHS generates the highest  $j$  at potentials more negatives than ca. 0.75 V/RHE (Fig. 5.4b), which indicates a high performance for the reaction as well, even though such relevant values are at high overpotentials.

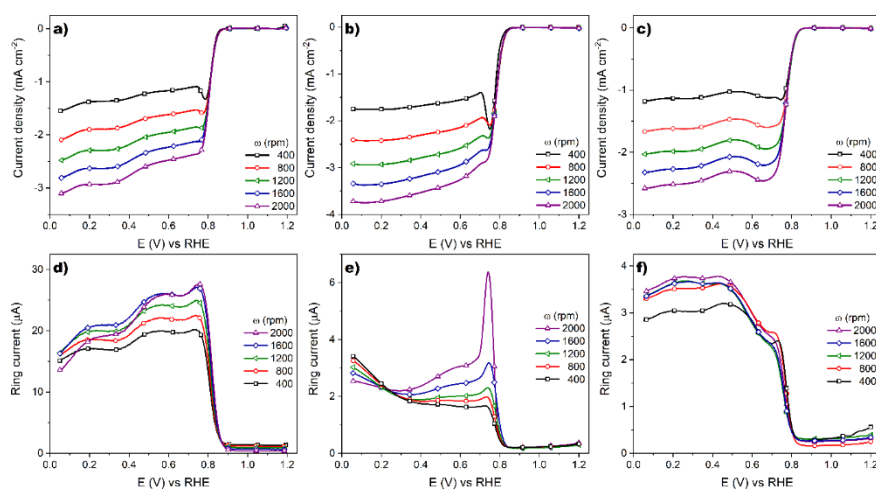


**Fig. 5.5.** 1<sup>st</sup> cycle polarization and ring current potential curves of the ORR at (a-d) S-OMCHS, (b-e) N1-S-OMCHS, and (c-f) N2-S-OMCHS performed in O<sub>2</sub>-saturated 0.5 mol L<sup>-1</sup> KOH, at a scan rate of 5 mV s<sup>-1</sup>.



Figs 5.5a-c) show 1<sup>st</sup> cycle polarization curves of the ORR at several rotation rates. The three electrocatalysts show kinetic, mixed, and diffusion-controlled characteristic regions of the ORR. Moreover, Figs 5.5d-e) shows plots of ring current at the same rotation rate of the ORR. From the data of the ORR polarization curves and ring current plots obtained at 2000 rpm, the %HO<sub>2</sub><sup>-</sup> and n values are obtained.

The %HO<sub>2</sub><sup>-</sup> and n values of N2-S-OMCHS are the highest in Table 5.2, even though it is not a poor performance. These results imply that the ORR at S-OMCHS, N1-S-OMCHS, and N2-S-OMCHS follows a 4e<sup>-</sup> transfer mechanism, with a very low %HO<sub>2</sub><sup>-</sup> yield. It should be mentioned that the electrocatalysts shown in this work outperform other carbon-based electrocatalysts in terms of %HO<sub>2</sub><sup>-</sup> and n values, as shown in Table 5.3.

**Table 5.3.** Comparison of catalytic performance for the ORR in terms of the E<sub>onset</sub>, E<sub>1/2</sub>, %HO<sub>2</sub><sup>-</sup>, and n of recently reported non-platinum electrocatalysts.

Catalyst	E <sub>onset</sub> (V/RHE)	E <sub>1/2</sub> (V/RHE)	HO <sub>2</sub> <sup>-</sup> (%)	n	Reference
Meso-Fe-N-C	0.95	0.85	-- <sup>a</sup>	3.95	ACS Catal. 2021 (11) 74-81
NiCo alloy N-doped graphene	0.81	0.66	<20	3.71	J Mater Sci 2020 (55) 15454-15466
Co-N-S-tri-doped carbon	0.95	0.72	25	3.5	J. Electrochem. Soc. 2020 (167) 024520
N-doped graphene	0.99	0.84	5	3.92	Int. J. Hydrogen Energy. 2020 (45) 32402-32412

--<sup>a</sup>: not determined

Contrary to the expectations, the N/S co-doped OMCHS show a lower catalytic activity for the ORR than S-doped OMCHS. This suggests that although the N/S co-doped OMCHS have a higher number of defects (I<sub>D\*</sub>/I<sub>G</sub> and I<sub>D'</sub>/I<sub>G</sub> ratios), it does not guarantee a better catalytic activity as mentioned before. However, their catalytic performance is well.

### 5.3. Surface chemical composition of S-doped and N/S-doped OMCHS before ADT

The surface chemical composition of powders of S-OMCHS, N1-S-OMCHS, and N2-S-OMCHS, determined by XPS, is shown in Table 5.4. The electrocatalysts are formed by carbon (C 1s), oxygen (O 1s), sulfur (S 2p), and nitrogen (N 1s) in the case of the co-doped, confirming the incorporation of the heteroatoms during the *in-situ* doping.

The carbon concentration in S-OMCHS is around 95 at. %, while for N1-S-OMCHS and N2-S-OMCHS is about 90 at.%. The oxygen concentration increases in the order S-OMCHS < N2-S-

OMCHS < N1-S-OMCHS. Meanwhile, the sulfur content is rather low, with a similar concentration in S-OMCHS and N1-S-OMCHS (0.2 at. %), which is less at N2-S-OMCHS (0.1 at. %). Moreover, the nitrogen content of N1-S-OMCHS is higher than that of N2-S-OMCHS (1.2 and 0.9 at. %, respectively). Thus, a successful co-doping with heteroatoms has been achieved, even though, with a low concentration, particularly that of S-species. No silicon has been detected, an indication of an effective leaching of the hard core, in good agreement with the micrographs of Fig. 5.3.

Deconvolution of the high-resolution C 1s, S 2p, and N 1s regions of the electrocatalysts before ADT are depicted in Fig. 5.6. Catalyst inks have been characterized (i.e., containing Nafion<sup>®</sup> solution), aiming to assure a similar evaluation of the electrocatalysts after ADT which is shown below (see Section 3.5). Eight peaks at different binding energy (BE) are identified in the C 1s region (Fig. 5.6a-c), corresponding to C=C sp<sup>2</sup> hybridization (284.7 eV), C-C sp<sup>3</sup> hybridization (285.7 eV), C-O (286.6 eV), C=O (287.6 eV), CF<sub>2</sub>-SO<sub>3</sub>H (288.96 eV), CF (290.3 eV), CF<sub>2</sub> (291.9 eV), and CF<sub>3</sub> (293.4 eV). The fluorine species are due to the presence of the Nafion<sup>®</sup> solution [35].

As can be seen, S-OMCHS, N1-S-OMCHS, and N2-S-OMCHS are predominantly composed of C=C bonds (53.8, 50.5, and 48.0 at. %, respectively, Table 5.5), indicating a partially graphitic structure, which agrees with the Raman results. Moreover, the relative concentration of C-O species is similar at S-OMCHS, N1-S-OMCHS, and N2-S-OMCHS (4.4 at. %, 4.7 at. %, and 4.3 at. %, respectively, Table 5.5). On the contrary, the relative concentration of C=O species is higher at S-OMCHS, compared to the co-doped electrocatalysts. On this matter, the relative concentration of C-O species is higher than that of C=O bonds at the electrocatalysts, which is ascribed to their surface functionalization with methanol. It can also be observed that the relative concentration of F-species attributed to Nafion<sup>®</sup> is similar in all electrocatalysts (Table 5.5).

Figs. 5.6d-f) show the deconvolution of the high-resolution spectra in the S 2p region of electrocatalysts, all of them showing two intense peaks at BE = 168.22 and 169.41 eV, which are attributed to the S 2p<sub>1/2</sub> and S 2p<sub>3/2</sub>, states respectively, due to spin-orbit splitting of HSO<sub>3</sub>. The presence of these species is ascribed to a functional group of Nafion<sup>®</sup> [36, 37]. In the case of S-OMCHS, a small peak is observed at 163.88 eV attributed to the presence of thiophene-S

species (C-S bonds). Typically, thiophene bonds are detected in S-doped carbon nanostructures, even though, in this case, its intensity is rather low [38]. Such species are not observed at the spectra of N1-S-OMCHS and N2-S-OMCHS, probably overshadowed by the HSO<sub>3</sub> species of Nafion<sup>®</sup> and probably by some effect of the N-species as well.

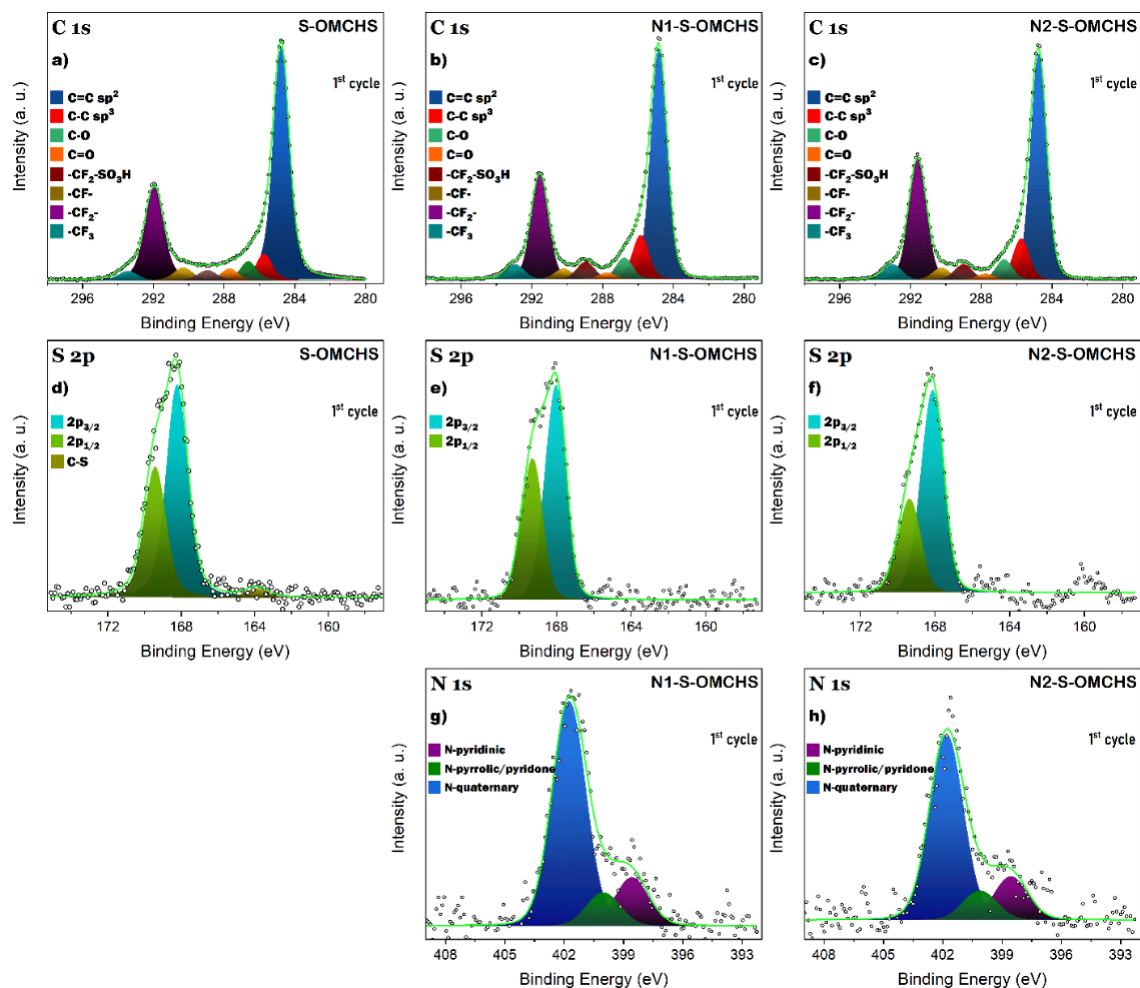


**Fig.5.6.** Deconvoluted high-resolution XPS spectra of S-OMCHS, N1-S-OMCHS, N2-S-OMCHS. (a-c) C 1s region, (d-f) S 2p region, and (g-f) N 1s region. The analysis has been performed on catalyst inks, i.e., containing Nafion<sup>®</sup> solution. Plots form the 1<sup>st</sup> cycle.

Figs. 5.6g-h) shows the deconvoluted N 1s region of N1-S-OMCHS and N2-S-OMCHS. Three peaks have been identified at about the same BE in both electrocatalysts (Table 5.5), which corresponds to N-pyridinic, N-pyrrolic/pyridone, and N-quaternary species, respectively [39]. These results confirm the successful doping of N1-S-OMCHS and N2-S-OMCHS with S and N species.

**Table 5.5.** XPS atomic relative concentration (RC) of the C 1s, S 2p, and N1s regions of electrocatalysts before (1<sup>st</sup> cycle) and after (3000<sup>th</sup> cycle) ADT.

Samples	State	Species	1 <sup>st</sup> cycle		3000 <sup>th</sup> cycle	
			BE (eV)	RC (%)	BE (eV)	RC (at. %)
S-OMCHS	C 1s	C=C	286.76	53.8	284.75	65.3
	C 1s	C-C	285.72	6.1	285.54	1.6
	C 1s	C-O	286.61	4.4	286.41	4.9
	C 1s	C=O	287.67	2.8	287.16	2.6
	C 1s	CF <sub>2</sub> -SO <sub>3</sub> H	288.93	2.7	289.17	5.1
	C 1s	CF	290.29	3.4	290.72	1.5
	C 1s	CF <sub>2</sub>	291.93	24.3	292.14	16.5
	C 1s	CF <sub>3</sub>	293.42	2.5	293.62	2.4
	S 2p	HSO <sub>3</sub>	168.22	60.3	168.53	67.2
			169.41	37.2	169.94	28.0
	S 2p	C-S	163.88	2.6	163.84	4.8
N1-S-OMCHS	C 1s	C=C	284.81	50.5	284.75	51.5
	C 1s	C-C	285.84	9.6	285.71	10.1
	C 1s	C-O	286.77	4.7	286.64	4.7
	C 1s	C=O	287.74	1.4	287.50	1.8
	C 1s	CF <sub>2</sub> -SO <sub>3</sub> H	288.94	4.0	288.69	2.7
	C 1s	CF	290.20	2.4	290.10	2.7
	C 1s	CF <sub>2</sub>	291.54	23.9	291.59	22.5
	C 1s	CF <sub>3</sub>	292.94	3.4	293.13	4.1
	S 2p	HSO <sub>3</sub>	167.86	60.2	167.92	64.1
			169.11	39.8	169.1	35.9
	N 1s	N-pyridinic	398.56	15.8	398.21	16.1
	N 1s	N-pyrrolic/pyridone	400.1	11.0	399.72	11.7
	N 1s	N-quaternary	401.74	73.2	401.22	53.7
	N 1s	Oxidized-N	--	--	402.41	18.6
N2-S-OMCHS	C 1s	C=C	284.74	48.0	284.80	44.4
	C 1s	C-C	285.73	8.7	285.73	9.4
	C 1s	C-O	286.69	4.3	286.66	4.9
	C 1s	C=O	287.75	1.3	287.63	2.2
	C 1s	CF <sub>2</sub> -SO <sub>3</sub> H	288.99	3.6	288.95	2.4
	C 1s	CF	290.23	2.8	290.40	1.7
	C 1s	CF <sub>2</sub>	291.58	27.8	291.99	27.4
	C 1s	CF <sub>3</sub>	292.99	3.6	293.42	7.5
	S 2p	HSO <sub>3</sub>	167.95	68.3	168.51	65.9
			169.2	31.7	167.72	34.1
	N 1s	N-pyridinic	398.5	16.8	398.38	22.0
	N 1s	N-pyrrolic/pyridone	400.1	11.4	399.86	14.6
	N 1s	N-quaternary	401.8	71.8	401.14	45.2
	N 1s	Oxidized-N	--	--	402.4	18.2

As observed, the combination of 2-thiophenemethanol with 2-pyridinecarboxaldehyde and pyrrole promotes the formation of N-quaternary over the two other N-species, with a relative concentration of 73.2 and 71.8 at. % at N1-S-OMCHS and N2-S-OMCHS, respectively (Table 5.5). The preferential formation of N-quaternary during co-doping is interesting and differs from the results observed for single-doped N1-OMCHS and N2-OMCHS (Chapter 4), at which N-pyridone and N-pyrrolic species are mainly formed (i.e., the corresponding N-species because of the use of 2-pyridinecarboxaldehyde or pyrrole as a source of nitrogen). Therefore, there is a strong chemical interaction between the heteroatoms during doping, which affects their relative concentration.

As commented, spectra in Fig. 5.6 have been obtained from catalyst inks, i.e., samples containing Nafion<sup>®</sup>. Aiming to evaluate the S 2p region in the absence of such a solution, powder without Nafion<sup>®</sup> of the electrocatalysts have been analyzed. Fig. 5.7 depicts the deconvolution of the high-resolution spectra of the S 2p region of the electrocatalysts. S-OMCHS fits into two signals at BE = 163 and 164

Fig. 5.7 depicts the deconvolution of the high-resolution spectra in the S 2p region of the electrocatalysts powder. S-OMCHS were fit to two components at ca. BE = 162.8 and 164.1 eV, corresponding to thiophene-S species. N1-S-OMCHS shows three signals at BE = 168.1, 169.5, and 164.2 eV, ascribed to oxidized-S (C-So<sub>x</sub>-C) and thiophene-S (the one at lower BE) species, respectively. Meanwhile, N2-S-OMCHS has two peaks attributed to oxidized-S species at 168.2 and 169.5 eV [28, 40].

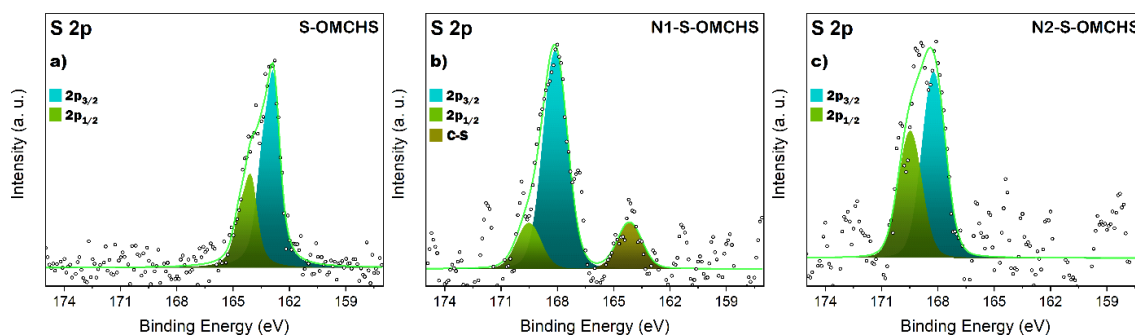


**Fig.5.7.** Deconvoluted high-resolution spectra of S-OMCHS, N1-S-OMCHS, and N2-S-OMCHS in the S 2p region.

Thus, it is confirmed that S-species are formed at the electrocatalysts from their doping with 2-thiophenemethanol. It has been reported that thiophene-S and oxidized-S species enhance the catalytic activity of S-doped carbon electrocatalysts for the ORR [41, 42]. Even more, it is acknowledged that the ORR follows a different path in S-doped metal-free electrocatalysts compared to N-doped because sulfur and carbon have a similar electronegativity. It has been proposed that spin density is a dominant factor in the enhancement of the catalytic activity of S-doped carbon electrocatalysts for the ORR [36].

The work by Perazzolo *et al.* shows that thiophene groups increase the surface hydrophobicity and induce strain in defect sites, also facilitating the charge transfer during the ORR [43]. Wang *et al.* mention that small concentrations of S-species can significantly promote the catalytic activity for the ORR (e.g.,  $E_{\text{onset}}$  more positive than non-doped and  $n = 3.8$ ) [29].

Wang *et al.* report that the high catalytic activity of S-doped carbon electrocatalysts for the ORR can be attributed to the bonding between S and benzene rings, or S sharing conjugate planar systems with delocalized p-electrons from the carbon lattice forming -C-S-C- species [26]. In this context, the high catalytic activity of S-OMCHS at low overpotentials can be attributed in part to the presence of thiophene-S species. Similarly, N1-S-OMCHS also shows high performance for the reaction, which can be ascribed to the thiophene-S and N-species developed during its co-doping, despite its lower  $SSA_{\text{DFT}}$ . N2-S-OMCHS has the lowest catalytic activity for the ORR, probably due to the absence of thiophene-S species in its structure, having C-SO<sub>x</sub>-C-species only, along with those due to N.

#### 5.4. Catalytic activity for the ORR and surface chemical composition of S doped and N/S co-doped OMCHS after ADT

Figs. 5.8a-c) depict the polarization curves of the ORR at the S-OMCHS, N1-S-OMCHS, and N2-S-OMCHS electrocatalysts in the 1<sup>st</sup> and 3000<sup>th</sup> cycles. After ADT,  $E_{\text{onset}}$  of S-OMCHS remains constant, while  $E_{1/2}$  shifts by 10 mV to a more positive value. Meanwhile,  $E_{\text{onset}}$  of N1-S-OMCHS shifts to 20 mV to more positive potentials, with  $E_{1/2}$  maintaining the same value compared to the 1<sup>st</sup> cycle. In contrast,  $E_{\text{onset}}$  and  $E_{1/2}$  are displaced by 10 mV towards more negative potentials after ADT at N2-S-OMCHS. In addition,  $j$  at 0.8 V/RHE increases 13.4 and 20.0 % after ADT at S-OMCHS and N1-S-OMCHS, respectively, decreasing in the case of N2-

S-OMCHS after ADT. Therefore, the S-OMCHS and N1-S-OMCHS show higher electrochemical stability after ADT than N2-S-OMCHS.

In the case of the  $\text{HO}_2^-$  yield (Fig. 5.8d), the values are less than 2.5 % at S-OMCHS and N1-S-OMCHS. Contrary, N2-S-OMCHS have values higher than 4 %. Moreover, the three electrocatalysts have been close to  $4e^-$  (Fig. 5.8e). However, S-OMCHS has the highest value of  $n$  at 0.4 V/RHE (3.97, Table 5.2) followed by N1-S-OMCHS and N2-S-OMCHS (3.96 and 3.91, respectively, Table 5.2). Thus, N1-S-OMCHS shows the highest stability after ADT in terms of  $E_{\text{onset}}$ ,  $E_{1/2}$ ,  $\% \text{HO}_2^-$ , and  $n$ . When comparing the electrochemical performance of N/S co-doped OMCHS after ADT, it is observed that they are more stable than N-doped OMCHS, which denotes a significant effect on performance with the addition of 2-thiophenemethanol as a sulfur source.

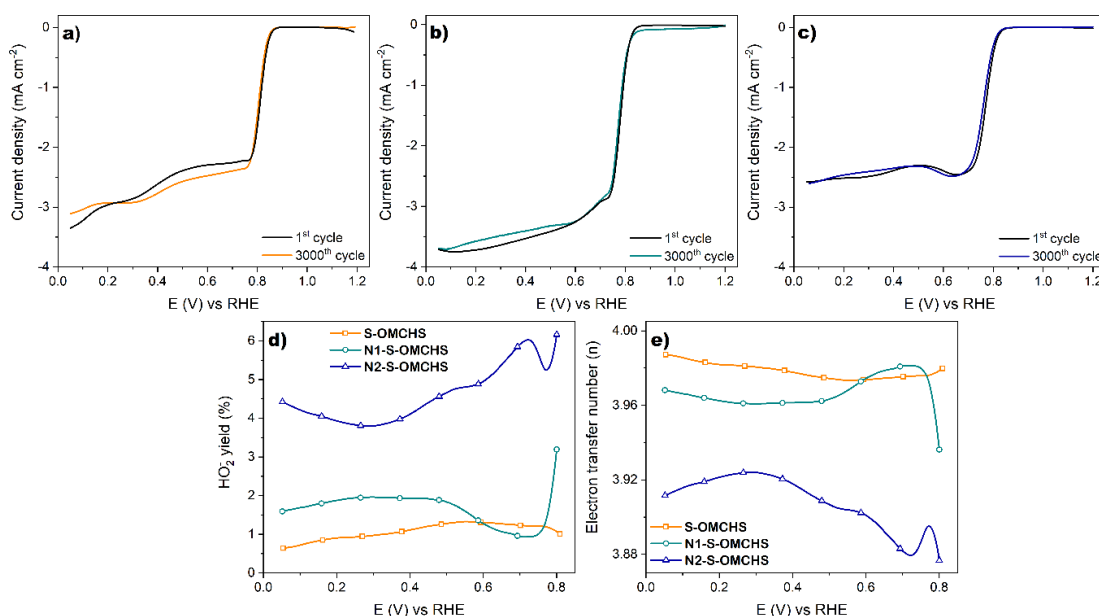


**Fig. 5.8.** Negative scan only of the CVs of the ORR at 2000 rpm (1<sup>st</sup> and 3000<sup>th</sup> cycles) at (a) S-OMCHS, (b) N1-S-OMCHS, and (c) N2-S-OMCHS. Electrolyte:  $\text{O}_2$ -saturated  $0.5 \text{ mol L}^{-1} \text{ KOH}$ , scan rate =  $5 \text{ mV s}^{-1}$  at 2000 rpm. d)  $\% \text{HO}_2^-$  and e)  $n$  plots at the 3000<sup>th</sup> cycle.

Perazzolo *et al.* report that after ADT, the surface concentration of N functional groups decreases because of their higher lability compared to thiophene groups, leading to an increase in the surface of carbon and a decrease in the limiting current of the ORR [44]. Besides, Liang *et al.* suggest that strong bonding between N, S, and C improves the chemical and mechanical properties of the latter, enhancing its electrochemical stability [45]. In this context, the high

stability showed for S-doped and N/S co-doped OMCHS are possible due to a strong interaction bonding between the N, S, and C atoms that prevent the loss of N functional groups. Moreover, polarization curves of the ORR before and after ADT in Figs. 5.8a-c) show that the limiting current (in the range of 0.8 to 0.05 V vs RHE) varies only slightly at S-OMCHS, N1-S-OMCHS, and N2-S-OMCHS, suggesting that the losses of S and N species at the electrocatalysts are low, thus sustaining a similar catalytic activity as that of the 1<sup>st</sup> cycle.

Aiming to explain the performance and electrochemical stability of S-OMCHS, N1-S-OMCHS, and N2-S-OMCHS after ADT, an analysis of their surface chemical composition has been performed by XPS. Figs 5.9a-c) show the high-resolution spectra in the C 1s region of the electrocatalysts after the 3000<sup>th</sup> cycle. Eight signals are observed, which correlate with those before ADT (Figs. 5.6a-c), even though with some variations in their relative concentration (Table 5.5). The C=C bonding increases at S-OMCHS and N1-S-OMCHS (65.3 and 51.5 at. %), meanwhile, N2-S-OMCHS decreases

The relative concentration of the Nafion-related species after ADT decreases a 22 and 5 % for S-OMCHS and N1-S-OMCHS, respectively. N2-S-OMCHS maintains a relative concentration like that before ADT. These values indicate that in the co-doped OMCHS, there is better interaction between the binder and the electrocatalyst, decreasing the detachment of the electrocatalyst during ADT.

The deconvoluted S 2p region of the electrocatalysts at the 3000<sup>th</sup> cycle is shown in Figs. 5.9d-f). The S-OMCHS electrocatalyst shows a signal at 163.98 eV due to thiophene-S species. The peak is more intense after ADT compared to that of the 1<sup>st</sup> cycle (Fig. 5.6d). Therefore, this species not only remains, rather but its relative concentration increases also from 2.6 before to 4.8 at. % after cycling (Table 5.5). Such thiophene-S species are not observed at N1-S-OMCHS and N2-S-OMCHS. Meanwhile, the signals corresponding to the SO<sub>3</sub> species of Nafion® at the 2p<sub>3/2</sub> and 2p<sub>1/2</sub> states are still observed at the electrocatalysts [46].

The high-resolution spectra of the N 1s region of N1-S-OMCHS and N2-S-OMCHS after 3000 cycles (Figs. 5.9g-h) show four peaks at ca. 398.4, 399.9, 401.2 and 402.4 eV, which are related to N-pyridinic, N-pyrrolic/N-pyridone, N-quaternary, and oxidized-N [47]. It should be noticed that oxidized-N species have not been detected during analysis of the 1<sup>st</sup> cycle (Figs. 5.6g-h and



Table 5.5). Rather, this species is formed from the 3000 cycles at which N1-S-OMCHS and N2-S-OMCHS are submitted, with a similar relative concentration in both cases. To a greater or lesser extent, there is an increase in the relative concentration of N-pyridinic and N-pyrrolic/N-pyridone species at N1-S-OMCHS and N1-S-OMCHS after cycling. Moreover, the relative concentration of N-quaternary shows an important decrease at both electrocatalysts after ADT (Table 5.5)

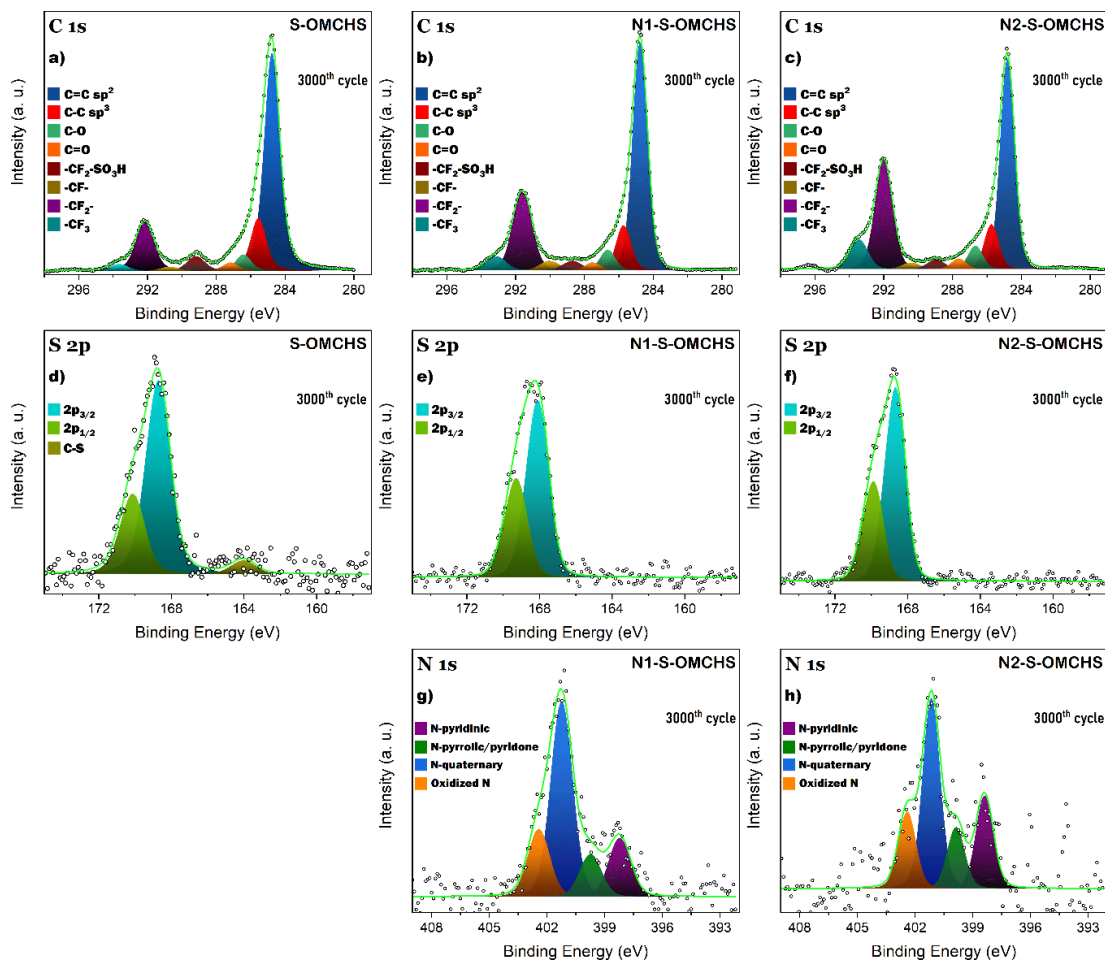


**Fig. 5.9.** Deconvolution of the high-resolution XPS spectra of the N/S-doped OMCHS (catalyst inks). (a-c) C 1s, (d-f) S 2p, and (g-h) N 1s region. 3000<sup>th</sup> cycle.

After performing ADT, Perazzolo *et al.* have found that the most stable nitrogen species is the N-quaternary, N-pyridine and N-pyrrole show higher stability [44]. The results shown in this work disagree from those of Ref. [44], in the sense that the relative concentration of N-quaternary decreases drastically after ADT, while that of N-pyridine and N-pyrrole increases

(more clearly at N2-S-OMCHS). The emergence of the oxidized-N species, along with the increase in N-pyridine and N-pyrrole suggests that N-quaternary has been oxidized after ADT. Therefore, these can be explained to the stability or modifications of the nitrogen species, as well as to an interaction between the N, S, and C atoms that contribute to the electrochemical stability of S-OMCHS, N1-S-OMCHS, and N2-S-OMCHS after ADT

Fig. 5.10 shows the high-resolution O 1s region of the electrocatalysts before and after cycling. The aim is to obtain more detailed information on the behavior of the oxygen species. Before ADT, S-OMCHS (Fig. 5.10a) shows three peaks at 531.9, 533.4, and 535.5 eV, ascribe to SO<sub>3</sub>, C-O, and OCF<sub>2</sub>, respectively. In addition to these species, N1-S-OMCHS and N2-S-OMCHS show another peak attributed to C=O bonds (531.1 eV). The SO<sub>3</sub> and OCF<sub>2</sub> peaks are functional groups of Nafion<sup>®</sup> [48].

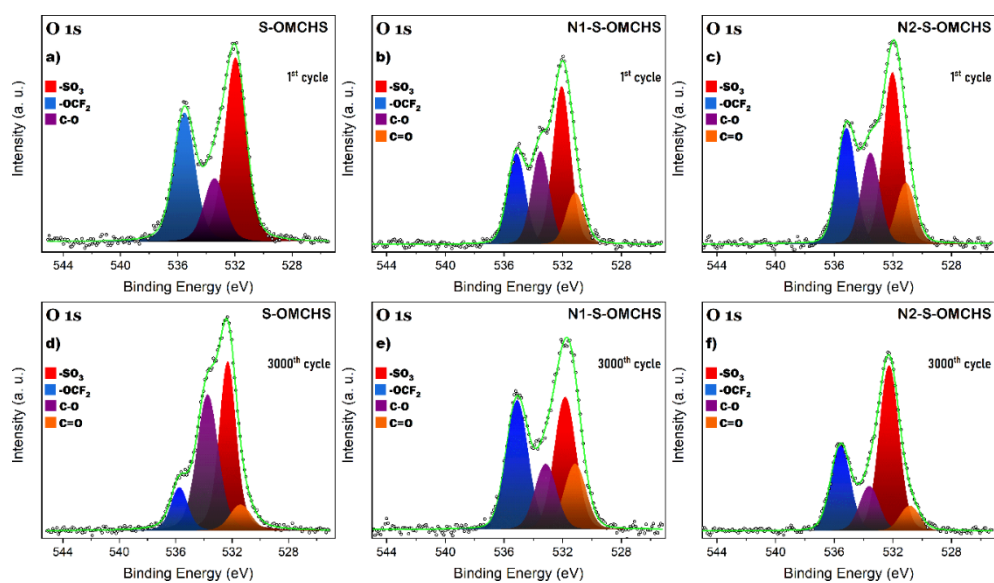


**Fig. 5.10.** High-resolution O 1s spectra of S-OMCHS, N1-S-OMCHS, and N2-S-OMCHS at the 1<sup>st</sup> and 3000<sup>th</sup> cycles.

After ADT, the peak due to C=O bonds emerges at S-OMCHS (Fig. 5.10d), which indicates the important interaction of oxygen species with carbon sites from cycling the electrocatalyst. The presence of C=O species contributed to the most electrocatalytic activity since these functional groups generate more active sites for the ORR than C-O as reported by Chen *et al.* [49]. The DFT studies that having C-O and C=O on the carbon lattice, generates a charge redistribution, positively generating carbon atoms that would function as active sites for the adsorption of

intermediate species of the ORR [46, 50]. This could be a determining factor due to the high oxygen content present in electrocatalysts, especially at S-OMCHS.

Fig.5.11a) shows the mass catalytic activity plots before ADT of the electrocatalysts discussed in this Chapter. S-OMCHS has a Tafel slope of  $40 \text{ mV decade}^{-1}$ , while those of N1-S-OMCHS and N2-S-OMCHS are  $45$  and  $43 \text{ mV decade}^{-1}$ , respectively. These values are also lower than that of Pt/C in Fig. 4.12, demonstrating the high catalytic activity for the ORR of the metal-free electrocatalysts. After ADT (Fig. 5.11b), there is a slight increase in the Tafel slope. Moreover, the mass current density is similar at the 3000<sup>th</sup> cycle compared to those at the 1<sup>st</sup>, confirming the high electrochemical stability of S-OMCHS, N1-S-OMCHS, and N2-S-OMCHS.

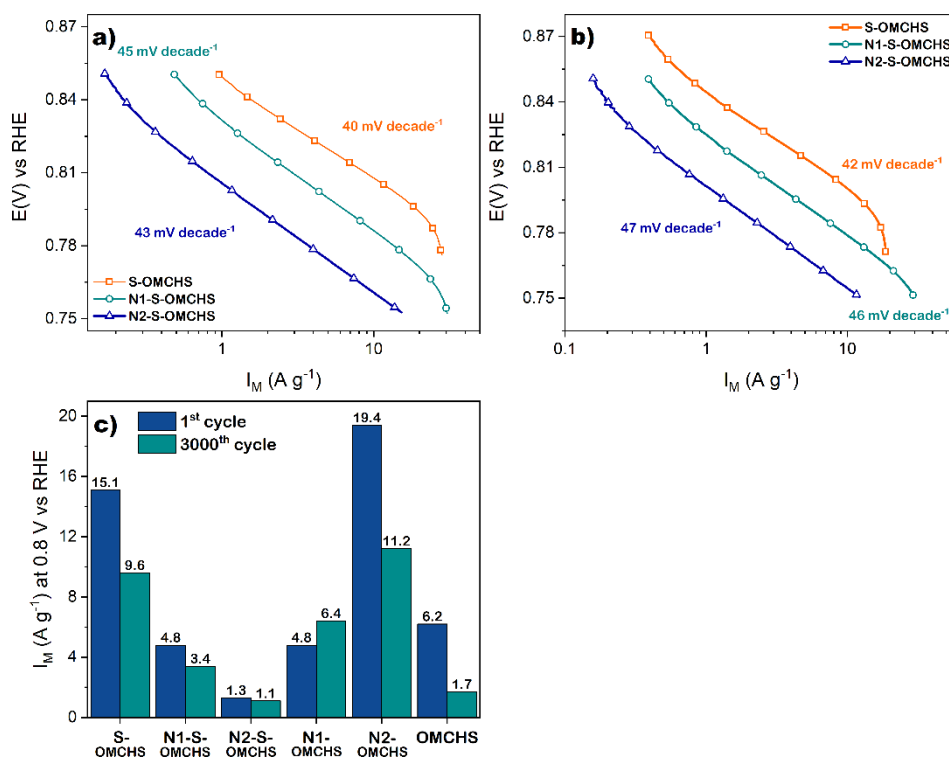


**Fig. 5.11.** Mass catalytic activity of S-OMCHS, N1-S-OMCHS, and N2-S-OMCHS at 2000 rpm at (a) 1<sup>st</sup> cycle and (b) 3000<sup>th</sup> cycle. (c) The mass current density of S-doped, N/S co-doped, N-doped, and non-doped OMCHS at 0.8 V/RHE.

For comparison purposes, those of the electrocatalysts characterized in Chapter 4 are also shown in Fig. 5.11c). It is observed that N2-OMCHS has a higher mass current density, followed by S-OMCHS, OMCHS, N1-OMCHS, N1-S-OMCHS and N2-S-OMCHS (19.4, 15.1, 6.2, 4.8, 4.8, and 1.3 A g<sup>-1</sup> at 0.8 V/RHE, respectively) before ADT. After ADT, the electrocatalysts show a

decrease in the mass current density, which represents a loss of 73, 42, 36, 29, and 15 % for OMCHS, N2-OMCHS, S-OMCHS, N1-S-OMCHS, and N2-S-OMCHS, respectively. On the contrary, N1-OMCHS shows an increase of 133 % ( $6.4 \text{ A g}^{-1}$ ). Therefore, N1-OMCHS shows the highest electrochemical stability. However, N2-S-OMCHS and N1-S-OMCHS electrocatalysts show good electrochemical stability despite the low mass current density compared to the others electrocatalysts (e.g., S-OMCHS and N2-OMCHS).

## 5.5. Conclusions

This chapter allowed us to compare the stability and catalytic activity for the ORR of electrocatalysts based on N/S co-doped OMCHS having the following conclusions:

- The use of 2-thiophenemethanol, 2-pyridinecarboxaldehyde, and pyrrole as sulfur and nitrogen precursors during synthesis has implications for the final textural and structural properties, morphology, and surface chemical composition of S-OMCHS, N1-S-OMCHS, and N2-S-OMCHS.
- The combination of sulfur and nitrogen atoms at carbon lattice decreases the formation of high crystallinity N/S co-doped OMCHS structures. However, they contribute to the formation of highly reactive nitrogen and sulfur species for the ORR.
- The high performance of N1-S-OMCHS electrocatalysts after ADTs is due to the high content of the N-quaternary species. Despite this, N-quaternary undergoes oxidation to form oxidized N species. Contrary, N2-S-OMCHS shows the lowest performance with good stability.
- The N/S co-doped OMCHS is the first effort to evaluate the potential use as cathode electrocatalysts for anion exchange membrane fuel cell applications. The performance of N/S co-doped OMCHS is lower than we expected. However, they stand out for their high stability, which would allow further studies to improve this type of electrocatalysts.

## Reference

- [1] X. Ma, H. Yuan, M. Hu. A simple method for synthesis of ordered mesoporous carbon. *Diam. Relat. Mater.* 98 (2019) 107480.
- [2] M. Zhou, J. Guo, L. Guo, J. Bai. Electrochemical Sensing Platform Based on the Highly Ordered Mesoporous Carbon–Fullerene System. *Anal. Chem.* 80 (2008) 4642–4650.
- [3] A. Y. Lee, K. Yang, N. DucAnh, C. Park, S. Lee, T. Lee, M. Jeong. Raman study of D\* band in graphene oxide and its correlation with reduction. *Appl. Surf. Sci.* 536 (2021) 147990.
- [4] L. G. Caçado, A. Jorio, E. H. Martins Ferreira, F. Stavale, C. A. Achete, R. B. Capaz, M. V. O. Moutinho, A. Lombardo, T. S. Kulmala, A. C. Ferrari. Quantifying defects in graphene via Raman spectroscopy at different excitation energies. *Nano Lett.* 11 (2011) 3190–3196.
- [5] S.A. Chernyak, A.S. Ivanov, K.I. Maslakov, A. V. Egorov, Z. Shen, S.S. Savirov, V. V. Lunin. Oxidation, defunctionalization and catalyst life cycle of carbon nanotubes: a Raman spectroscopy view. *Phys. Chem. Chem. Phys.* 19 (2017) 2276–2285.
- [6] S. Sze. Raman spectroscopic characterization of carbonaceous aerosols. *Atmos. Environ.* 35 (2001) 561–568.
- [7] S. Praver, K. Nugent, D. Jamieson, J. Orwa, L. Bursill, J. Peng. The Raman spectrum of nanocrystalline diamond. *Chem. Phys. Lett.* 332 (2000) 93–97.
- [8] L. Bokobza, J.-L. Bruneel, M. Couzi. Raman spectroscopic investigation of carbon-based materials and their composites. Comparison between carbon nanotubes and carbon black. *Chem. Phys. Lett.* 590 (2013) 153–159.
- [9] M.R. Ammar, J.N. Rouzaud. How to obtain a reliable structural characterization of polished graphitized carbons by Raman microspectroscopy. *J. Raman Spectrosc.* 43 (2012) 207–211.
- [10] S. Claramunt, A. Varea, D. López-Díaz, M.M. Velázquez, A. Cornet, A. Cirera. The Importance of Interbands on the Interpretation of the Raman Spectrum of Graphene Oxide. *J. Phys. Chem. C* 119 (2015) 10123–10129.
- [11] P.A. Goodman, H. Li, Y. Gao, Y.F. Lu, J.D. Stenger-Smith, J. Redepinning. Preparation and characterization of high surface area, high porosity carbon monoliths from pyrolyzed bovine bone and their performance as supercapacitor electrodes. *Carbon* 55 (2013) 291–298.
- [12] O. Beyssac, B. Goffé, J.P. Petitet, E. Froigneux, M. Moreau, J.N. Rouzaud. On the characterization of disordered and heterogeneous carbonaceous materials by Raman spectroscopy. *Spectrochim. Acta - Part A Mol. Biomol. Spectrosc.* 59 (2003) 2267–2276.
- [13] X. He, X. Liu, B. Nie, D. Song. FTIR and Raman spectroscopy characterization of functional groups in various rank coals. *Fuel* 206 (2017) 555–563.
- [14] J. Zhang, J. Zhang, F. He, Y. Chen, J. Zhu, D. Wang, S. Mu, H. Yang. Defect and Doping Co-Engineered Non-Metal Nanocarbon ORR Electrocatalyst. *Nano-Micro Lett.* 13 (2021) 1–30.
- [15] C. Xie, D. Yan, W. Chen, Y. Zou, R. Chen, S. Zang, Y. Wang, X. Yao, S. Wang. Insight into the design of defect electrocatalysts: From electronic structure to adsorption energy. *Mater. Today.* 31 (2019) 47–68.
- [16] A. Ambrosi, M. Pumera. Amorphous carbon impurities play an active role in redox processes of carbon nanotubes. *J. Phys. Chem. C.* 115 (2011) 25281–25284.
- [17] Y. Li, J. Zhong, X.Z. Yang, G.J. Lan, H.D. Tang, H.Z. Liu. Simple synthesis of semi-graphitized ordered mesoporous carbons with tunable pore sizes. *New Carbon Mater.* 26 (2011) 123–129.
- [18] L. Tao, L. Liu, R. Chang, H. He, P. Zhao, J. Liu. Structural and interface design of hierarchical porous carbon derived from soybeans as anode materials for potassium-ion batteries. *J. Power Sources.* 463 (2020) 228172.
- [19] E. Alwin, K. Kočí, R. Wojcieszak, M. Zieliński, M. Edelmannová, M. Pietrowski. Influence of High Temperature Synthesis on the Structure of Graphitic Carbon Nitride and Its Hydrogen Generation Ability. *J. Mater.* 13 (2020) 2756.

- [20] Z.U. Ahmad, Q. Lian, M.E. Zappi, P.R. Buchireddy, D.D. Gang. Adsorptive removal of resorcinol on a novel ordered mesoporous carbon (OMC) employing COK-19 silica scaffold: Kinetics and equilibrium study. *J. Environ. Sci.* 75 (2019) 307–317.
- [21] M. Thommes, K. Kaneko, A. V. Neimark, J.P. Olivier, F. Rodriguez-Reinoso, J. Rouquerol, K.S.W. Sing. Physisorption of gases, with special reference to the evaluation of surface area and pore size distribution (IUPAC Technical Report). *Pure Appl. Chem.* 87 (2015) 1051–1069.
- [22] A. Chen, Y. Yu, Y. Li, Y. Wang, Y. Li, S. Li, K. Xia. Synthesis of macro-mesoporous carbon materials and hollow core/mesoporous shell carbon spheres as supercapacitors. *J. Mater. Sci.* 51 (2016) 1–8.
- [23] T. Cai, W. Xing, Z. Liu, J. Zeng, Q. Xue, S. Qiao, Z. Yan. Superhigh-rate capacitive performance of heteroatoms-doped double shell hollow carbon spheres. *Carbon* 86 (2015) 235–244.
- [24] B. Chao, M. I. Konggidinata, L. Lin, M. Zappi, D. D. Gang. Effect of carbon precursors and pore expanding reagent on ordered mesoporous carbon for resorcinol removal. *J. Water Process Eng.* 17 (2017) 256–263.
- [25] W. Shen, X. Yang, Q. Guo, Y. Liu, Y. Song, Z. Han, Q. Sun, J. Cheng. The effect of carbon precursor on the pore size distribution of mesoporous carbon during templating synthesis process. *Mater. Lett.* 60 (2006) 3517–3521.
- [26] C. Wang, F. Yang, C. Xu, Y. Cao, H. Zhong, Y. Li. Sulfur-doped porous graphene frameworks as an efficient metal-free electrocatalyst for oxygen reduction reaction. *Mater. Lett.* 214 (2018) 209–212.
- [27] M. Klingele, C. Pham, K.R. Vuyyuru, B. Britton, S. Holdcroft, A. Fischer, S. Thiele. Sulfur doped reduced graphene oxide as metal-free catalyst for the oxygen reduction reaction in anion and proton exchange fuel cells. *Electrochem. commun.* 77 (2017) 71–75.
- [28] E. Montiel Macias, A.M. Valenzuela-Muñiz, G. Alonso-Núñez, M.H. Farías Sánchez, R. Gauvin, Y. Verde Gómez. Sulfur doped carbon nanohorns towards oxygen reduction reaction. *Diam. Relat. Mater.* 103 (2020) 107671.
- [29] H. Wang, X. Bo, Y. Zhang, L. Guo. Sulfur-doped ordered mesoporous carbon with high electrocatalytic activity for oxygen reduction. *Electrochim. Acta* 108 (2013) 404–411.
- [30] X. Zhang, Y. Wang, Y. Du, M. Qing, F. Yu, Z.Q. Tian, P.K. Shen. Highly active N,S co-doped hierarchical porous carbon nanospheres from green and template-free method for super capacitors and oxygen reduction reaction. *Electrochim. Acta* 318 (2019) 272–280.
- [31] S. Yang, X. Mao, Z. Cao, Y. Yin, Z. Wang, M. Shi, H. Dong. Onion-derived N, S self-doped carbon materials as highly efficient metal-free electrocatalysts for the oxygen reduction reaction. *Appl. Surf. Sci.* 427 (2018) 626–634.
- [32] J.C. Li, X. Qin, P.X. Hou, M. Cheng, C. Shi, C. Liu, H.M. Cheng, M. Shao. Identification of active sites in nitrogen and sulfur co-doped carbon-based oxygen reduction catalysts. *Carbon* 147 (2019) 303–311.
- [33] X. Xing, R. Liu, M. Anjass, K. Cao, U. Kaiser, G. Zhang, C. Streb. Bimetallic manganese-vanadium functionalized N,S-doped carbon nanotubes as efficient oxygen evolution and oxygen reduction electrocatalysts. *Appl. Catal. B Environ.* 277 (2020) 119195.
- [34] H. Lin, D. Chen, C. Lu, C. Zhang, F. Qiu, S. Han, X. Zhuang. Rational synthesis of N/S-doped porous carbons as high efficient electrocatalysts for oxygen reduction reaction and Zn-Air batteries. *Electrochim. Acta* 266 (2018) 17–26.
- [35] C. Chen, G. Levitin, D.W. Hess, T.F. Fuller. XPS investigation of Nafion® membrane degradation. *J. Power Sources* 169 (2007) 288–295.
- [36] Y. Sun, J. Wu, J. Tian, C. Jin, R. Yang. Sulfur-doped carbon spheres as efficient metal-free electrocatalysts for oxygen reduction reaction. *Electrochim. Acta* 178 (2015) 806–812.
- [37] B. Wang, J. Hu, L. Zhang. Nitrogen and sulfur co-doped hierarchical porous carbon as functional sulfur host for lithium-sulfur batteries. *Mater. Today Commun.* 27 (2021) 102312.
- [38] Y. Wen, H. Zhu, J. Hao, S. Lu, W. Zong, F. Lai, P. Ma, W. Dong, T. Liu, M. Du. Metal-free boro and sulphur co-doped carbon nanofibers with optimized p-band centers for highly efficient nitrogen electroreduction to ammonia. *Appl. Catal. B: Environ.* 292 (2021) 120144

- [39] M. Fan, C. Zhu, J. Yang, D. Sun. Facile self-assembly N-doped graphene quantum dots/graphene for oxygen reduction reaction. *Electrochim. Acta* 216 (2016) 102–109.
- [40] F. Li, L. Sun, Y. Luo, M. Li, Y. Xu, G. Hu, X. Li, L. Wang. Effect of thiophene S on the enhanced ORR electrocatalytic performance of sulfur-doped graphene quantum dot/reduced graphene oxide nanocomposites. *RSC Adv.* 8 (2018) 19635–19641.
- [41] J. E. Park, Y. Jang, Y. Kim, M. Song, S. Yoon, D. Kim, S. Kim. Sulfur-doped graphene as a potential alternative metal-free electrocatalyst and Pt-catalyst supporting material for oxygen reduction reaction. *Phys. Chem. Chem. Phys.* 16 (2014) 103–109.
- [42] S. Yang, L. Zhi, K. Tang, X. Feng, J. Maier, K. Müllen. Efficient synthesis of heteroatom (N or S)-doped graphene based on ultrathin graphene oxide-porous silica sheets for oxygen reduction reactions. *Adv. Funct. Mater.* 22 (2012) 3634–3640.
- [43] V. Perazzolo, C. Durante, R. Pilot, A. Paduano, J. Zheng, G.A. Rizzi, A. Martucci, G. Granozzi, A. Gennaro. Nitrogen and sulfur doped mesoporous carbon as metal-free electrocatalysts for the in situ production of hydrogen peroxide. *Carbon* 95 (2015) 949–963.
- [44] V. Perazzolo, E. Grądzka, C. Durante, R. Pilot, N. Vicentini, G.A. Rizzi, G. Granozzi, A. Gennaro. Chemical and Electrochemical Stability of Nitrogen and Sulphur Doped Mesoporous Carbons. *Electrochim. Acta* 197 (2016) 251–262.
- [45] J. Liang, Y. Jiao, M. Jaroniec, S.Z. Qiao. Sulfur and nitrogen dual-doped mesoporous graphene electrocatalyst for oxygen reduction with synergistically enhanced performance. *Angew. Chem. Int. Ed.* 51 (2012) 11496–11500.
- [46] I.S. Flyagina, K.J. Hughes, M. Pourkashanian, D.B. Ingham. A Theoretical Study of Molecular Oxygen Chemisorption on N, B, or O Doped Carbon Edge Sites. *Fuel Cells* 14 (2014) 709–719.
- [47] C. Maouche, Y. Zhou, B. Li, C. Cheng, Y. Wu, J. Li, S. Gao, J. Yang. Thermal treated three-dimensional N-doped graphene as efficient metal free-catalyst for oxygen reduction reaction. *J. Electroanal. Chem.* 853 (2019) 113536.
- [48] A.K. Friedman, W. Shi, Y. Losovyj, A.R. Siedle, L.A. Baker. Mapping Microscale Chemical Heterogeneity in Nafion Membranes with X-ray Photoelectron Spectroscopy. *J. Electrochem. Soc.* 165 (2018) H733–H741.
- [49] S. Chen, T. Luo, K. Chen, Y. Lin, J. Fu, K. Liu, C. Cai, Q. Wang, H. Li, X. Li, J. Hu, H. Li, M. Zhu, M. Liu. Chemical Identification of Catalytically Active Sites on Oxygen-doped Carbon Nanosheet to Decipher the High Activity for Electro-synthesis Hydrogen Peroxide. *Angew. Chem. Int. Ed.* 60 (2021) 16607–16614.
- [50] Z. Liu, Z. Zhao, Y. Wang, S. Dou, D. Yan, D. Liu, Z. Xia, S. Wang. In Situ Exfoliated, Edge-Rich, Oxygen-Functionalized Graphene from Carbon Fibers for Oxygen Electrocatalysis. *Adv. Mater.* 29, 1606207.



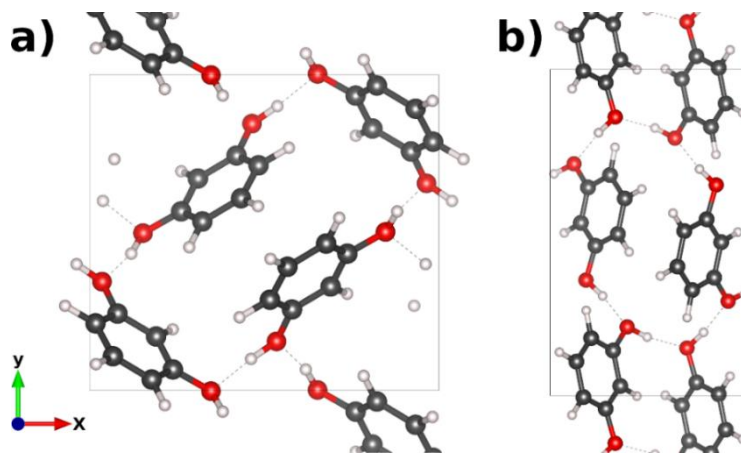
## CHAPTER VI.

### Three-dimensional modeling the Resorcinol-Formaldehyde (R-F) polymer: a DFT and XRD study.

---

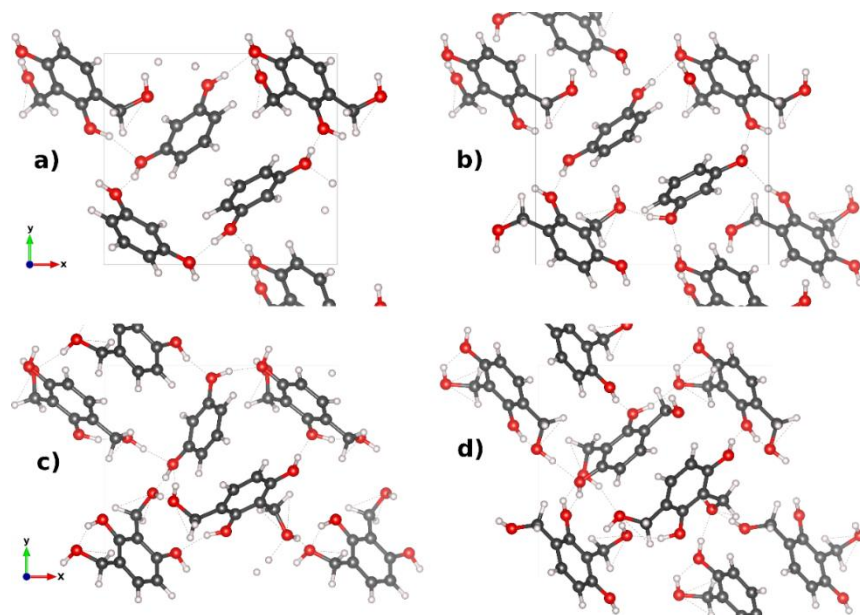
#### 6.1. Determination of lattice parameters, enthalpy of formation ( $\Delta H_f$ ) and bulk modulus.

Fig. 6.1 shows the relaxed crystal structures of a)  $\alpha$  and b)  $\beta$  resorcinol used in the polymerization model. An important difference between the two phases is the molecular configuration assumed for the structures. In the  $\alpha$  phase, both hydroxyl groups are pointing downwards, while in the  $\beta$  phase one hydroxyl points upwards and the other downwards. It is acknowledged that  $\alpha$ -resorcinol is more stable, than  $\beta$ -resorcinol since the latter is obtained by heating the former at temperatures above 80° C [1]. Both phases will be studied for modeling the R-F polymer.



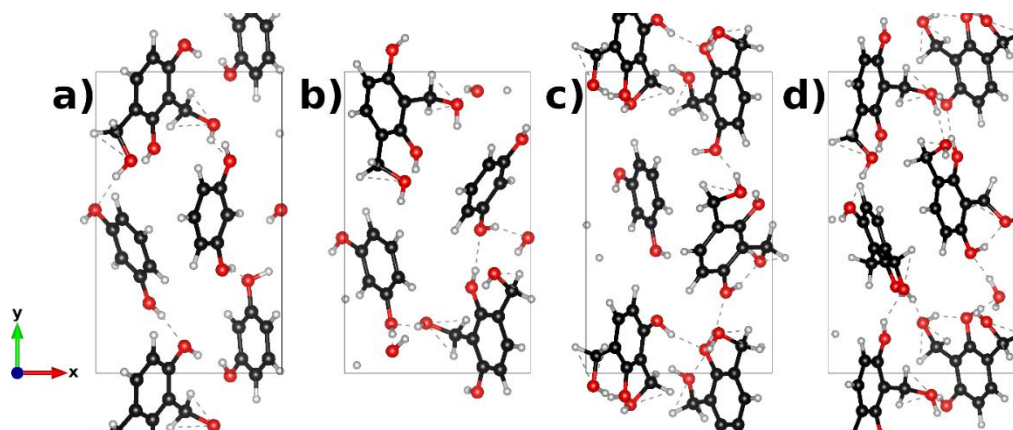
**Fig. 6.1.** (a)  $\alpha$ -resorcinol and (b)  $\beta$ -resorcinol crystals structures. The view is such that molecules of any of the structures project equal areas on the plane of the page.

Figure 6.2 shows the structure of  $\alpha$ -resorcinol saturated with a) two (2HMR), b) four (4HMR), c) six (6HMR), and d) eight (8HMR) hydroxymethyl molecules. In the case of 2HMR, the resorcinol molecule at the upper left corner undergoes a rotation due to the addition of hydroxymethyl groups, while the rest maintain their initial positions. This effect becomes more relevant in 4HMR and 6HMR (Figs. 6.2 b and c), where resorcinol molecules with and without hydroxymethyl groups rotate in at least two of their directions. The rotation of resorcinol molecules promotes the formation of methylene and methylene ether bridges, which will be discussed later in this section.



**Fig. 6.2.** Spatial configuration of (a) 2HMR, (b) 4HMR, (c) 6HMR, and (d) 8HMR in 3D-coordinates. The view is such that molecules of any of the structures project equal areas on the plane of the page.

Figure 6.3 depicts the structure of  $\beta$ -resorcinol saturated with a) two (2HMR-B), b) four (4HMR-B), c) six (6HMR-B), and d) eight (8HMR-B) hydroxymethyl molecules. Resorcinol molecules are subject to rotation and displacement when concentration with hydroxymethyl groups increases, as in  $\alpha$ -resorcinol. However, the resorcinol molecule in the center-left of the 8HMR-B model rotates to form a bond with that in the z-direction. This behavior causes the formation of bridges between the ethanol-type resorcinol molecules ( $-\text{CH}_2\text{-CHOH}-$ ), as well as the emerging of water molecules. Such type of bridges has not been found in the literature, which suggests that the result shown in Fig. 6.3d) is highly unlikely.



**Fig. 6.3.** Spatial configuration of (a) 2HMR-B, (b) 4HMR-B, (c) 6HMR-B, and (d) 8HMR-B in 3D coordinates. The view is such that molecules of any of the structures project equal areas on the plane of the page.

Plots of total energy as a function of the atomic volume and the fitting of the Birch-Murnaghan equations of state (BM-EOS) of a) 2HMR, b) 4HMR, c) 6HMR, and d) 8HMR are shown in Fig 6.4. The BM-EOS is obtained from the fitting of theoretical energy-volume data with an empirical functional form of the EOS and indicates the degree of stiffness or the energy necessary to produce a volumetric deformation [2]. Taking the minimum energy as starting point, two regions of energetic stability (compression and expansion zone) can be distinguished.

The volume of  $\alpha$ -resorcinol is  $554.05 \text{ \AA}^3$  and increases to 599.09, 686.14, 786.79, and  $794.79 \text{ \AA}^3$  (i.e., 8%, 24%, 42%, and 43% increment) in 2HMR, 4HMR, 6HMR, and 8HMR, respectively (Table 6.1). The normalized volume at which 2HMR, 4HMR, 6HMR, and 8HMR stabilize is 9.46, 9.55, 9.83, and  $9.03 \text{ \AA}^3 \text{ atoms}^{-1}$ , respectively. An increase in cell volume occurs as 2, 4, and 6 hydroxymethyl molecules are added, decreasing at 8HMR. Presumably, the unit cell of 8HMR is close to stability, requiring no further expansion, a feature that can be seen more clearly when observing the cell volume of 6HMR.

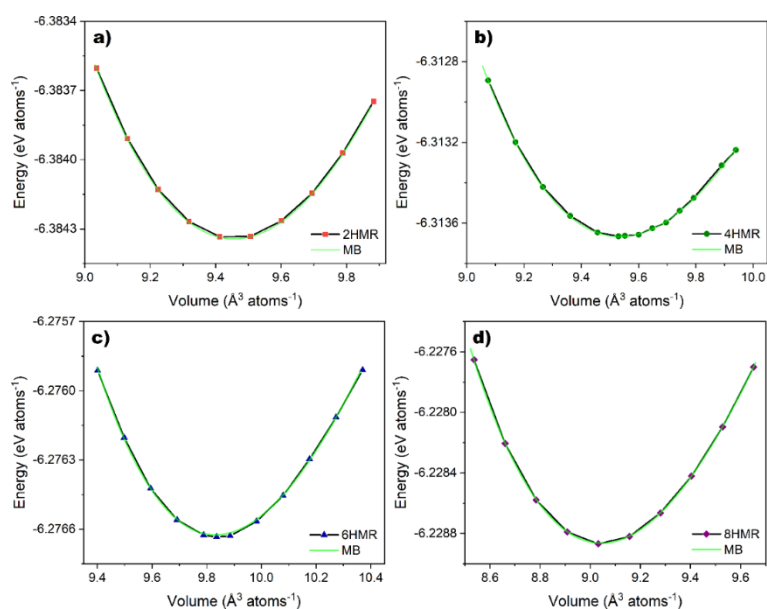


**Fig. 6.4.** Total energy as a function of the volume of the (a) 2HMR, (b) 4HMR, (c) 6HMR, and (d) 8HMR. Green line is BM EOS fits.

Meanwhile, the volume of  $\beta$ -resorcinol is increasing by 18%, 29%, 46%, and 57% in 2HMR-B, 4HMR-B, 6HMR-B, and 8HMR-B, respectively (Table 6.1). Their normalized volume is 9.76, 9.51, 9.71,  $9.49 \text{ \AA}^3 \text{ atoms}^{-1}$ , respectively (Figure 6.5). As can be seen, the normalized volume expands and compresses as the number of hydroxymethyl molecules increases. For 2HMR-B

and 4HMR-B, this effect can be explained by an expansion of cell parameters due to the addition of new resorcinol molecules as hydroxymethyl groups are added. In the case of 6HMR-B and 8HMR-B, the lower normalized volume compared to 2HMR-B and 4HMR-B, may be due to the formation of ethanol-type bridges, which provokes a reduction in the distance between molecules.

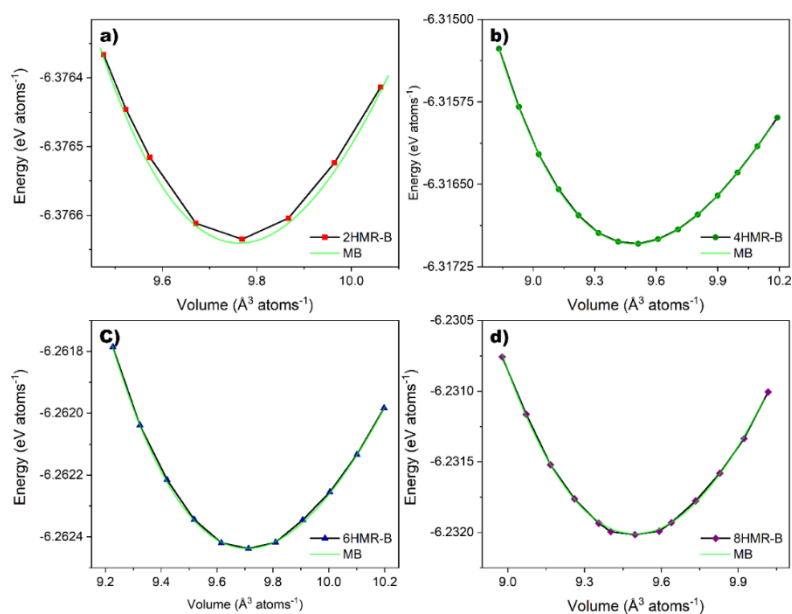


**Fig. 6.5.** Total energy as a function of the volume of the (a) 2HMR-B, (b) 4HMR-B, (c) 6HMR-B, and (d) 8HMR-B. Green line is MB EOS fits.

**Table 6.1.** Lattice parameters, volume, and  $\Delta H_f$  of  $\alpha$ -resorcinol and  $\beta$ -resorcinol containing hydroxymethyl molecules.

Model	Unit cell parameters (Å)			Normalized Volume (Å <sup>3</sup> atom <sup>-1</sup> )	$\Delta H_f$ (kJ mol <sup>-1</sup> )
	X	y	z		
2HMR	10.76	9.73	5.72	599.09	-26.15
4HMR	11.25	10.19	5.98	686.14	-195.41
6HMR	11.78	10.66	6.26	786.79	-511.58
8HMR	11.82	10.70	6.29	794.79	-679.49
2HMR-B	8.24	13.31	5.73	628.31	11.01
4HMR-B	8.48	13.70	5.89	684.86	-225.62
6HMR-B	8.85	14.29	6.15	776.98	-408.78
8HMR-B	9.06	14.64	6.30	835.76	-712.96

The enthalpy of formation ( $\Delta H_f$ ) of 2HMR, 4HMR, 6HMR, and 8HMR are shown in Table 6.1. As can be seen, the values increase as more hydroxymethyl molecules are added, showing that

8HMR is the model that requires the lowest energy to form. Meanwhile, the same trend is observed for the models based on  $\beta$ -resorcinol, i.e., the  $\Delta H_f$  values decrease with more hydroxymethyl molecules (Table 6.1). Thus, the lowest  $\Delta H_f$  is that of 8HMR-B. It is worth mentioning that 2HMR-B is the least feasible system of those shown in the Table. Next, methylene and methylene ether bridges are formed by eliminating the hydroxyl functional groups in the hydroxymethyl molecules. The distance between active sites for methylene and methylene ether bridges must be ca. 3 Å and 4.5 Å, respectively.

Figs. 6.6 a-b) show the  $\alpha$ -resorcinol structure with two and four methylene bridges, labeled as 2MR and 4MR, respectively. Fig. 6.6 c) shows the same molecule with four methylene bridges plus one methylene ether bridge (6MR), while Fig. 6.6 d) depicts four methylene bridges plus two methylene ether bridges (8MR). The 2MR, 4MR, 6MR, and 8MR models correspond to the 2HMR, 4HMR, 6HMR, and 8HMR models, respectively. The rotations and displacements that resorcinol undergoes when adding hydroxymethyl molecules allow, at this point, the formation of methylene bridges with an orientation towards the active sites.

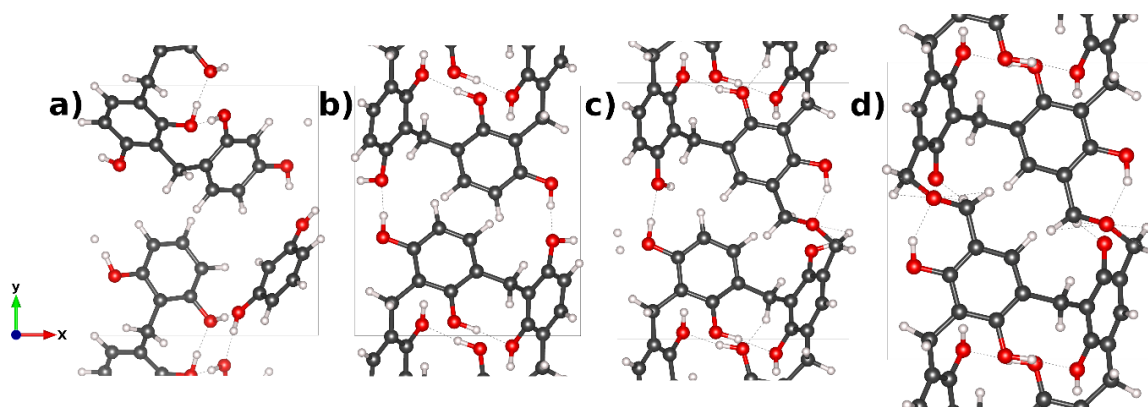


**Fig. 6.6.** Spatial configuration of (a) 2MR, (b) 4MR, (c) 6MR, and (d) 8MR in 3D coordinates. The view is such that molecules of any structure project equal areas on the plane of the page.

Figs. 6.7 a) and b) depict the  $\beta$ -resorcinol structure with two and four methylene bridges (labeled as 2MR-B and 4MR-B, respectively). Fig. 6.7 c) shows five methylene bridges plus one methylene ether bridge (7MR-B). Unlike  $\alpha$ -resorcinol derivatives,  $\beta$ -resorcinol derivatives show mostly methylene-type bridges. 7MR-B shows fewer bridges than 8MR because the distance between the active sites of each resorcinol is shorter, which makes the formation of methylene ether bridges more difficult at the former. Furthermore, the maximum number of bridges that

can be formed in either of the two models ( $\alpha$  or  $\beta$ ) is six, since twelve is the maximum number of active sites that are not occupied.

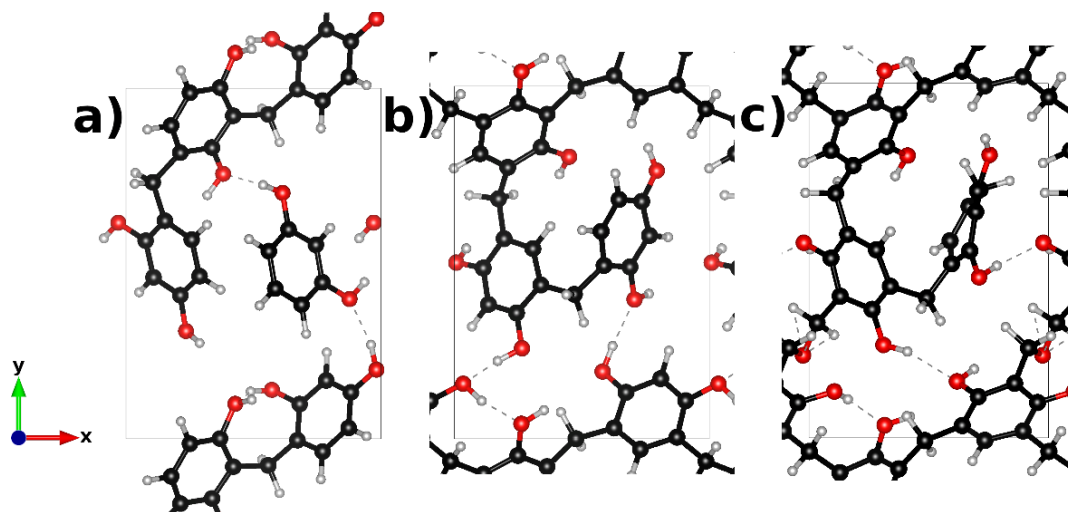


**Fig. 6.7.** The spatial configuration of (a) 2MR-B, (b) 4MR-B, and (c) 7MR-B in 3D coordinates. The view is such that molecules of any structure project equal areas on the plane of the page.

Plots of total energy as a function of the atomic volume of a) 2MR, b) 4MR, c) 6MR, and d) 8MR are shown in Fig 6.8. Taking the minimum energy as a normalized volume, the values are 10.71, 9.42, 9.68, 9.23  $\text{\AA}^3 \text{ atoms}^{-1}$  for 2MR, 4MR, 6MR, and 8MR, respectively, slightly higher than those reported for the HMR family of molecules in Table 6.1. The values decrease in the order 2MR > 6MR > 4MR > 8MR, while those above have the order 6HMR > 4HMR > 2HMR > 8HMR.

The unit cell parameters and volume of 2MR, 4MR, 6MR, and 8MR are shown in Table 6.2. As can be seen, the volume of 4MR, 6MR, and 8MR is lower compared to that of 4HMR, 6HMR, and 8HMR. Meanwhile, that of 2MR is higher than that of 2HMR. The 2MR, 4MR, 6MR, and 8MR models require a compression of their cell to allow the formation of methylene or methylene bridges, thus, resorcinol molecules must take different positions from those of the HMR models, which explains the increase or decrease in volume of 2MR, 4MR, 6MR, and 8MR compared to those in Table 6.1.

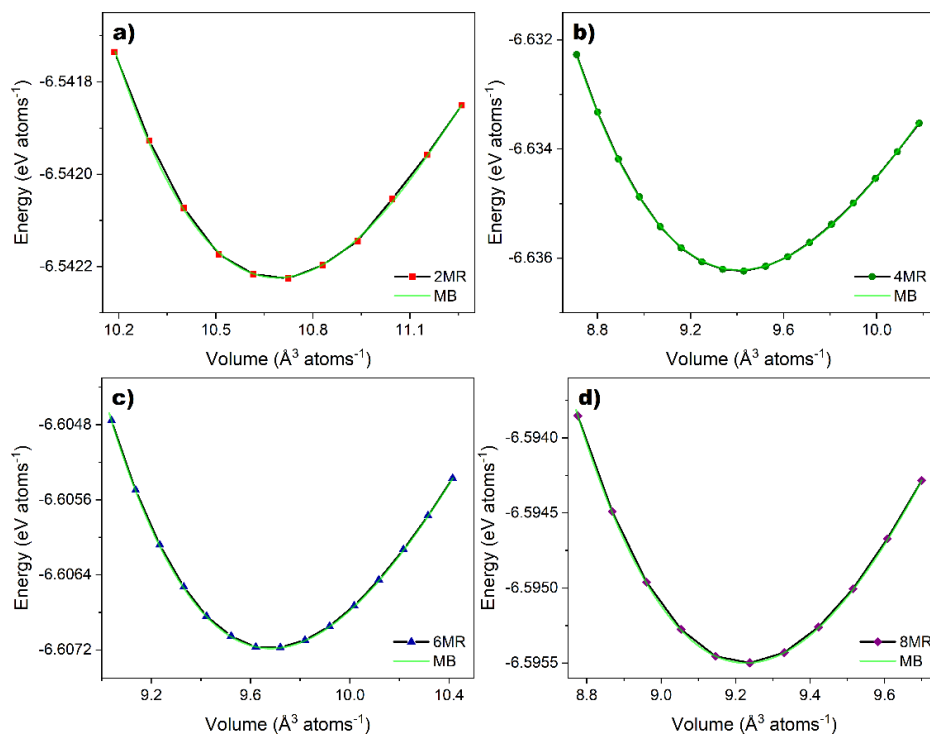


**Fig. 6.8.** Total energy as a function of the volume of the (a) 2MR, (b) 4MR, (c) 6MR, and (d) 8MR. Green line is MB EOS fits.

The lattice parameters and volume of 2MR-B, 4MR-B, and 7MR-B are shown in Table 6.2. It is noticeable that these models are also subject to compression compared to 2HMR-B, 4HMR-B, 6HMR-B, and 8HMR-B (Table 6.1). Plots of total energy as a function of atomic volume of a) 2MR-B, b) 4MR-B, and c) 8MR-B are shown in Fig 6.9. Taking the minimum energy as a reference, the normalized volume is 9.86, 8.75, 8.55, i.e., 2MR-B > 4MR-B > 7MR-B. It should be recalled that the normalized volume decreases in the order 2HMR-B > 6HMR-B > 4HMR-B > 8HMR-B in Table 6.1.

A particularly interesting effect is observed from these results. Even though  $\alpha$ -resorcinol and  $\beta$ -resorcinol have different configurations, both 4MR and 4MR-B have the lowest volumes of all models in Tables 6.1 and 6.2, most likely because the resorcinol:formaldehyde molecular ratio is 1:1 in both cases. Such configuration allows a better arrangement of the molecules by reducing their lattice parameters. However, when normalizing the volume, this trend is not maintained.

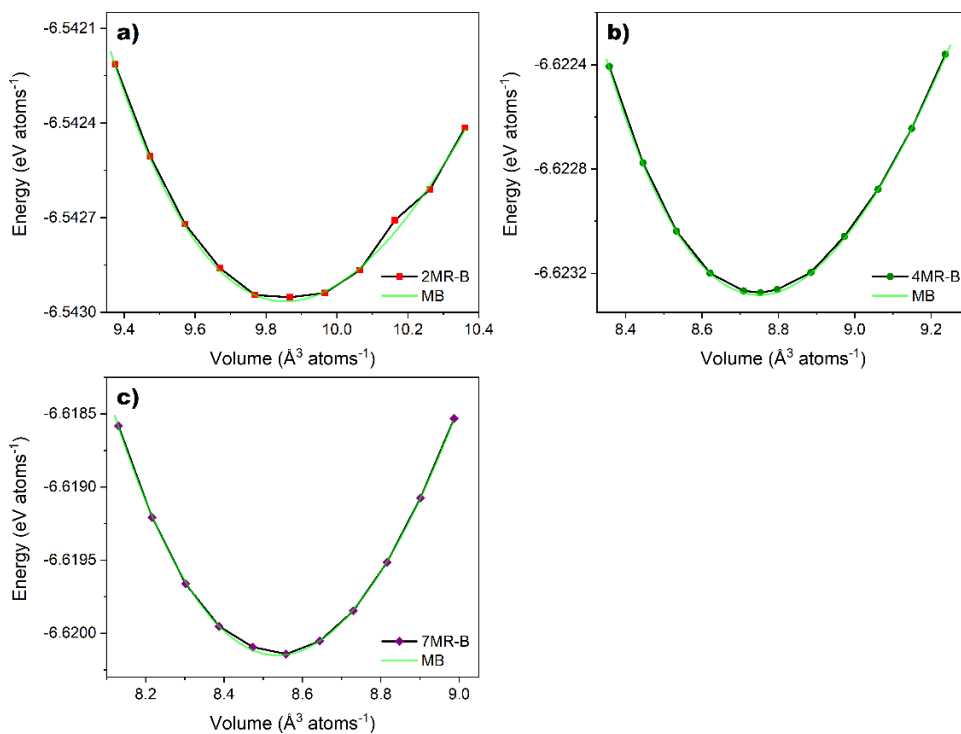


**Fig. 6.9.** Total energy as a function of the volume of the (a) 2MR-B, (b) 4MR-B, and (c) 8MR-B. Green line is MB EOS fits.

The formation enthalpies of the  $\alpha$ -MR and  $\beta$ -MR molecules are shown in Table 6.2. As can be seen, the values decrease as the bridges are formed, indicating that the more exothermic reactions are those of the  $\alpha$ -models. On the contrary, the reactions to form 2MR and 2MR-B are highly endothermic because a compression must occur first before the formation of the bridges, thus, are difficult to proceed.

**Table 6.2.** Lattice parameters and volume of  $\alpha$ -MR and  $\beta$ -MR.

Model	Unit cell parameters (Å)			Volume (Å <sup>3</sup> )	$\Delta H_f$ (kJ mol <sup>-1</sup> )
	X	y	z		
2MR	10.89	9.86	5.79	621.98	36.99
4MR	10.55	9.55	5.61	565.75	-243.90
6MR	10.95	9.91	5.82	631.81	-364.55
8MR	11.03	9.99	5.87	646.66	-574.60
2MR-B	9.41	12.91	4.71	572.19	26.18
4MR-B	9.23	12.71	4.48	525.18	-175.63
7MR-B	8.54	12.62	5.24	564.88	-328.49



Atom-atom distances and angles of the bridges in the models have been determined. The average atom-atom bond lengths of methylene bridges are 1.51 Å (C-C) and 1.11 Å (C-H), with an angle of 119°. Meanwhile, those of methylene ether bridges are 1.51 Å (C-C), 1.46 Å (C-O), and 1.1 Å (C-H), with an angle of 118°. The bond lengths calculated here are similar to those reported by El-Gammal *et al.* [3].

It is acknowledged that resorcinol has three active sites on its ring, so three methylene or methylene ether bridges should form through condensation at the 2-2', 2-4', and 4-4' positions, as schematized in Fig. 6.10. However, the study of an R-F polymer using <sup>13</sup>C NMR elsewhere shows that the 2-4' and 4-4' positions are predominant over the 2-2' linkages [4]. Therefore, from the beginning, the position of the molecules in  $\alpha$ -resorcinol and  $\beta$ -resorcinol preferentially tend to form methylene bridges on the 2-4' and 4-4' positions, over the 2-2' bonds.

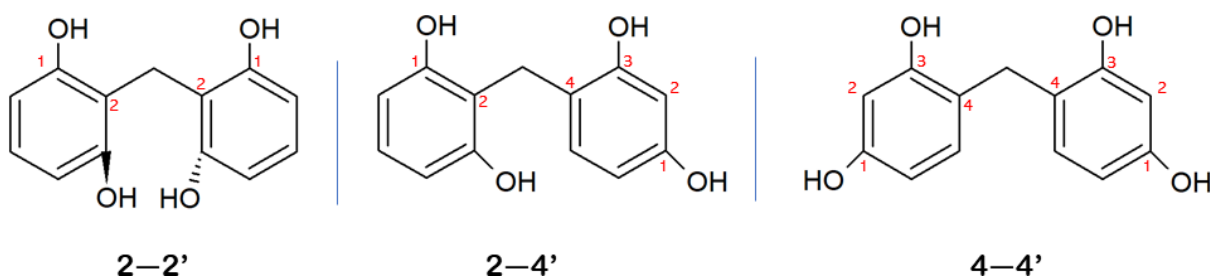


**Figure 6.10.** Scheme of the three methylene bridges that are formed in the different active sites.

## 6.2. Comparative analysis of experimental and theoretical XRD patterns of R-F polymers.

For the comparison, RF polymers having 1:0.5, 1:1, 1:1.5, and 1:2 resorcinol:formaldehyde ratios have been synthesized, aiming to correlate them with the 2MR, 4MR, 6MR, 8MR, 2MR-B, and 4MR-B theoretical models, respectively. Fig. 6.11 shows the experimental XRD pattern of RF(1:0.5) and its comparison with the theoretical one of a) 2MR and b) 2MR-B. The pattern of resorcinol (PDF 38-1969 card) is also depicted. RF(1:0.5) shows a broad shoulder between ca. 10 and 45° (2 $\theta$ ), suggesting a partially amorphous structure, along with several reflections ascribed to resorcinol, as seen in the card. The pattern of 2MR (Fig. 6.11 a) shows a series of peaks that coincide with that of RF(1:0.5), attributed to two phenomena: i) most resorcinol atoms remain in their positions, i.e., are not displaced by hydroxymethyl molecules, and ii) methylene bridges are not modified in the theoretical molecule.

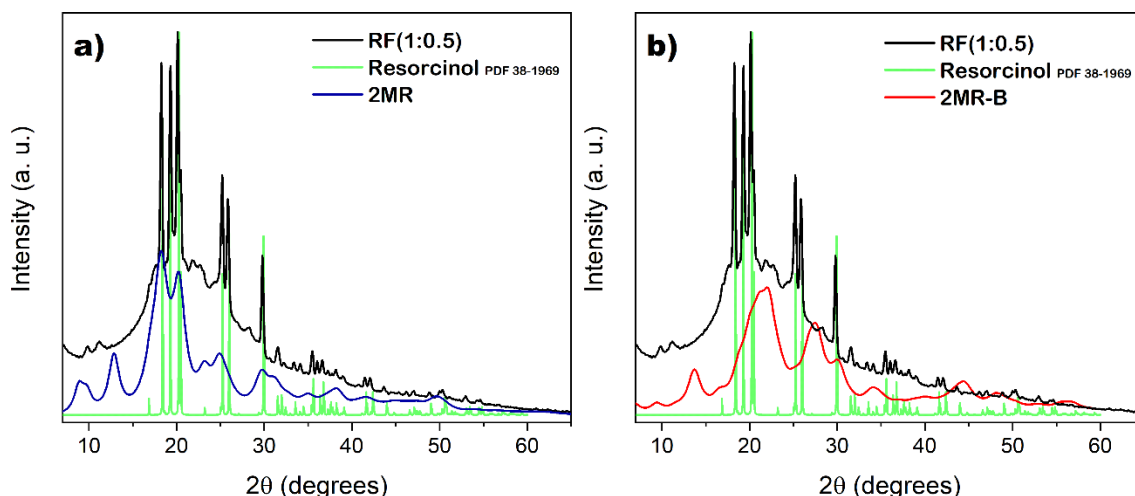


**Fig. 6.11.** Experimental and theoretical XRD pattern of RF(1:0.5), (a) 2MR, and (b) 2MR-B.

Meanwhile, the theoretical pattern of 2MR-B in Figure 6.11 b) shows the several peaks not identified by the resorcinol card. Nevertheless, some of those reflections coincide with peaks of RF(1:0.5). Thus, it can be concluded that both  $\alpha$  and  $\beta$  phases of resorcinol have developed in the structure of RF(1:0.5).

The diffraction pattern of RF(1:1) in Fig. 6.12 shows that the polymer is rather amorphous. It has two broad peaks, one intense at  $20.8^\circ$  ( $2\theta$ ), and the second barely detected at  $37.8^\circ$  ( $2\theta$ ). The pattern of 4MR (Fig. 6.12 a) shows an intense peak with a maximum at  $18.2^\circ$  ( $2\theta$ ), i.e., shifted towards lower angles compared to the peak maximum of RF(1:1). 4MR has the smallest volume of the  $\alpha$ -resorcinol family of models (Table 6.2), therefore, the shift of the peak compared to the experimental pattern is attributed to a lattice contraction. Above  $35^\circ$  ( $2\theta$ ), several reflections of 4MR correlate with the low-intensity peak of RF(1:1) at  $37.8^\circ$ . Meanwhile, the pattern of 4MR-B (Fig. 6.12 b) has an intense peak at  $20.3^\circ$  ( $2\theta$ ), close to the peak maximum observed at RF(1:1). However, the peaks above  $35^\circ$  ( $2\theta$ ) do not fit with the experimental pattern, contrary to the features of 4MR.

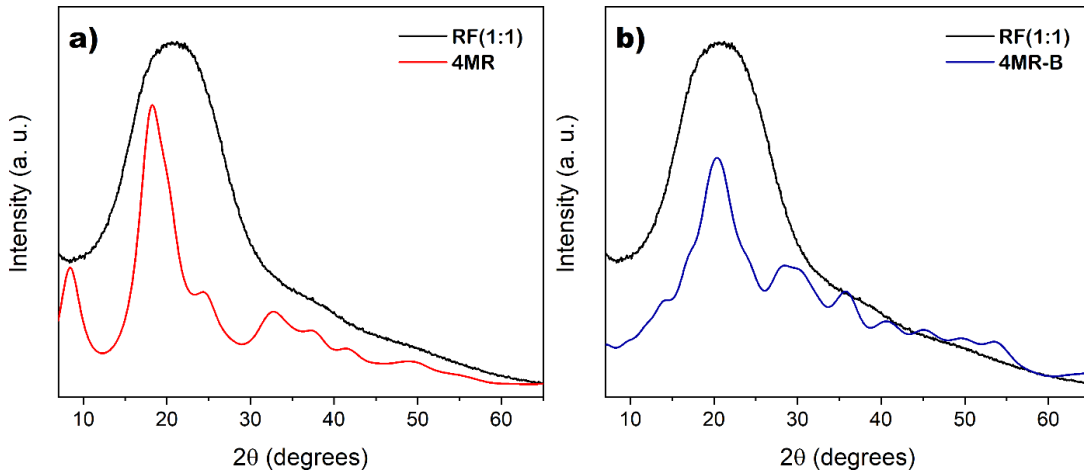


**Fig. 6.12.** Experimental and theoretical XRD pattern of RF(1:1), (a) 4MR, and (b) 4MR-B.

Fig. 6.13 shows the experimental XRD pattern of RF(1:1.5), along with the theoretical one of 6MR. The main peak of RF(1:1.5) has a maximum at  $17.3^\circ$  ( $2\theta$ ), an important shift towards lower angles compared to RF(1:1) in Figure 6.12. The peak is also broader at RF(1:1.5), suggesting that it may be composed of several diffractions. Moreover, it displays a very small and narrow peak at  $31.3^\circ$  ( $2\theta$ ). The theoretical pattern of 6MR shows reflections that match the peaks at  $17.3^\circ$  and  $31.3^\circ$  ( $2\theta$ ).

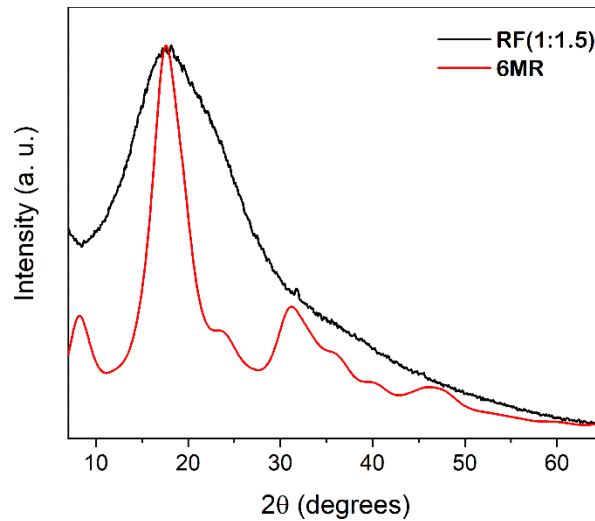


**Fig. 6.13.** Experimental and theoretical XRD pattern of RF(1:1), and 6MR.

Fig. 6.14 shows the experimental pattern of RF(1:2), with the theoretical patterns of a) 8MR and b) 7MR-B. RF(1:2) shows a mean peak at  $17.7^\circ$  ( $2\theta$ ) and because of its broadness it seems to

be composed by several reflections. It also has a small and narrow peak at  $32.2^\circ$  ( $2\theta$ ). Overall, the pattern of RF(1:2) resembles that of RF(1:1.5) in Fig. 6.13.

The most intense peak of 8MR has a maximum ( $17.7^\circ$ ) that fits that of RF(1:2), while a second reflection is at a slightly lower  $2\theta$  value than that at  $32.2^\circ$  in the experimental pattern. On the other hand, even though the peak maximum of the main reflection of 7MR-B is slightly shifted towards a higher  $2\theta$  value compared to the experimental pattern, it shows three reflections in the  $10\text{-}30^\circ$  ( $2\theta$ ) interval, which seem to correlate with the broadness of RF(1:2) in such range. 7MR-B also has a small peak at about the same  $2\theta$  value as that at  $32.2^\circ$  in RF(1:2) can be attributed to traces of resorcinol that did not react with formaldehyde. Above  $2\theta = 35^\circ$ , several reflections emerge at 7MR-B, a feature that completely differs from the experimental pattern.

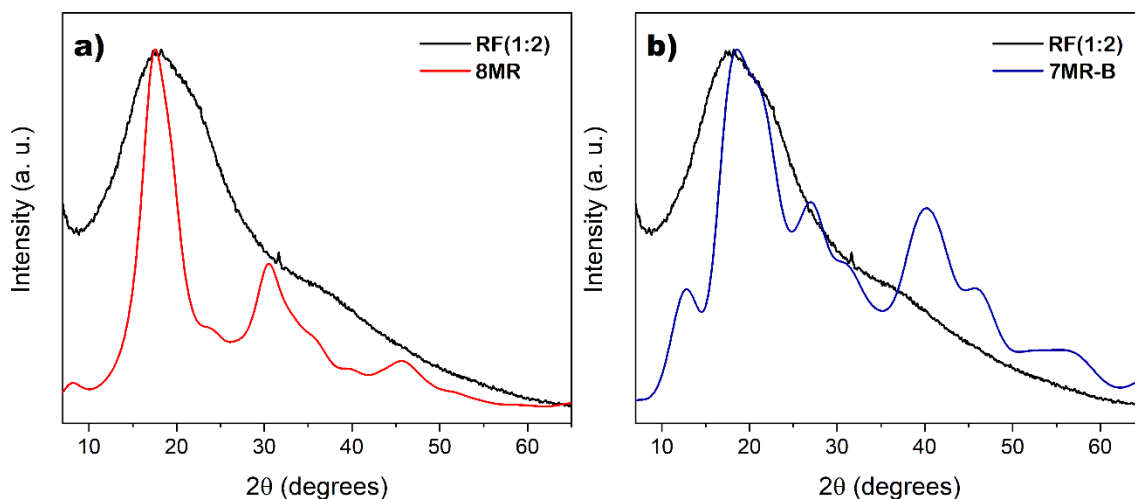


**Fig. 6.14.** Experimental and theoretical XRD pattern of RF(1:1),(a) 8MR, and (b) 6MR.

The results show that the patterns of the  $\alpha$ -resorcinol models have no drastic modifications at the different R:F ratios, while those based on  $\beta$ -resorcinol show significant changes between them when increasing the amount of formaldehyde.

### 6.3. Conclusions

Three-dimensional models of the R-F polymers were proposed, leading to the following conclusions:

- The hydroxymethyl intermediate reaction is a necessary step in the mechanism for the subsequent formation of methylene bridges, which in turn promote the formation of polymer chains.
- The most energetically feasible models for the formation of R-F polymers are 8MR and 7MR-B.
- The similarities between the XRD pattern of RF(1:2) and those of 8MR and 7MR-B provide the certainty that the theoretical models resemble the experimental one. Nevertheless, it is acknowledged that more experimental studies are still needed to optimize the models.

### References

- [1] J. Chatchawalsaisin, J. Kendrick, S.C. Tule, J. Anwar. An optimized force field for crystalline phases of resorcinol. *CrystEngComm* 10 (2008) 437–445.
- [2] E. Kim, C. Chen. Calculation of bulk modulus for highly anisotropic materials. *Phys. Lett. A* 326 (2004) 442–448.
- [3] B. El-Gammal, G.M. Ibrahim, I.M. El-Naggar. Preparation of some resorcinol formaldehyde resins for the separation of <sup>134</sup>CS from acidic waste streams. *Desalin. Water Treat.* 52 (2014) 4721–4733.
- [4] A.W. Christiansen. Resorcinol-formaldehyde reactions in dilute solution observed by carbon-13 NMR spectroscopy. *J. Appl. Polym. Sci.* 75 (2000) 1760–1768.